December 2018

Fabrication and Mechanical Properties of Micro-Architectured 3D Scaffolds

Pooya Niksiar
Clemson University, pooyaniksiar@gmail.com

FABRICATION AND MECHANICAL PROPERTIES OF MICRO-ARCHITECTURED 3D SCAFFOLDS

A Dissertation
Presented to
the Graduate School of
Clemson University

In Partial Fulfilment
of the Requirements for the Degree
Doctor of Philosophy
Mechanical Engineering

---

by
Pooya Niksiar
December 2018

Accepted by:
Dr. Gang Li, Committee Chair
Dr. Michael Porter, Co-Chair
Dr. Huijuan Zhao
Dr. Hongseok Choi

ABSTRACT

Freeze casting is a physical process for the fabrication of porous anisotropic materials. In this method, an aqueous slurry of ceramic particles is frozen directionally, creating lamellar columns of ice that push particles between the growing crystals. Then, the frozen material is lyophilized to remove the ice and sintered to densify the ceramic. Scaffolds made by freeze casting often have significant strength in the solidification direction, while they lack sufficient strength in the transverse direction. To enhance strength in the transverse direction, magnetite particles are added to a slurry of paramagnetic particles, and an external magnetic field is applied during solidification. Interactions between the magnetite and paramagnetic particles compete with thermal and viscous forces, resulting in different colloidal behaviors. Under relatively weak magnetic fields, the particles are attracted to one another, forming aligned chains that are trapped by the ice front and result in bridges spanning the lamellar walls. When interactions between magnetite and paramagnetic particles are strong, the alignment of magnetite also results in alignment of the paramagnetic particles. Under stronger magnetic fields, however, a gradient magnetic force attracts particles toward the field's poles, creating biphasic regions of iron-rich and iron-poor microstructures.

To further investigate the relationship between microstructure and mechanical properties observed, 3D printed scaffolds mimicking patterns observed in magnetic freeze casting were designed and fabricated for comparison. The 3D printed scaffolds were tested in compression in three orthogonal directions. To compare their performance, permutated radar charts were used to simultaneously

analyze the strength, toughness, resilience, elastic modulus and strain to failure across each orthogonal direction.

DEDICATION

To my parent, sibling (Shohreh, Sharareh and Reza), Mahsa and Amir, who have always supported and motivated me in learning more and achieving higher!

ACKNOWLEDGMENTS

I would like to thank my adviser Dr. Michael Porter as without his help I could not do that much and would not be able to finish this dissertation. His support and patience in mentoring and advising me step by step is really appreciated. I am very grateful and blessed to have such adviser. I also would like to thank Dr. Gang Li as he has been amazing in supporting and helping me to go through the final stages of my dissertation. Definitely if it was not Dr. Li's help, this dissertation never would have finished!

I also would like to thank my committee members Dr. Huijuan Zhao and Dr. Hongseok Choi for their help and serving in my committee and also proving constructive feedbacks.

I would like to thank Department of Mechanical Engineering of Clemson University for letting me use equipment to finish my research and also financial support during my PhD. In this regard, I would like to thank Dr. Richard Figliola, Dr. Todd Schweisinger, Dr. Atul Kelkar, Dr. Joshua Summers, Ms. Trish Nigro and Ms. Kathryn Poole.

I am also thank my labmates Ella Moore, Nakul R Kumar, Subrata Deb Nath, Garret Hall, Dakota Holt and Mathew Miller which was a privilege to work with them.

TABLE OF CONTENTS

Page

Table of Contents (Continued)

Page

LIST OF TABLES

Page

LIST OF FIGURES

Page

LIST OF FIGURES (CONTINUED)

LIST OF FIGURES (CONTINUED)

LIST OF FIGURES (CONTINUED)

LIST OF FIGURES (CONTINUED)

LIST OF FIGURES (CONTINUED)

LIST OF FIGURES (CONTINUED)

CHAPTER 1

POROUS MATERIALS

The mechanical properties of materials not only depend on the properties of the constituents they are made of but also depend on the composition and microstructural architecture. For instance, changing the crystalline structure of an alloy from Body-Centered Cubic (BCC) to Face Centered Cubic (FCC), will impart mechanical property changes, or making high entropy alloys by combining more than five different elements in a homogenous way will enhance the strength, hardness, wear resistance, and corrosion/oxidation resistance versus conventional alloys[1,2]. On the other hand, many applications require porosity in themselves, such as bone; not only does it provide body support, but it also provides a network for blood flow and red/white blood cell reproduction[3]. Porosity brings various advantages to the materials. It makes them lightweight and ideal for

insulation/filtration[4–6]; also porous materials have found applications in heat exchangers, chemical analyses, acoustic scattering, sensors, energy absorption systems, vibration control and energy storage, just to mention a few[7–11].

However, most porous material have an inherent drawback—they lack sufficient mechanical properties due to porosity. For porous materials, in addition to the two mentioned parameters (constituents and composition), microstructural architecture is another contributing factor in their mechanical properties. Porous materials can be natural like trabecular or cancellous bone, honeycomb, cork and wood, or man-made such as cushioning foams, sandwich panels, artificial biological implants, or heat resistant ceramic tiles of space shuttles[12]. Honeycomb structures are porous materials inspired from the natural honeycomb which are made in different cell shapes and designs. The different cell shape of honeycomb is shown in **Figure 1.1**. Cell shapes can be square (see **Figure 1.1a**), equilateral triangle (see **Figure 1.1b**), hexagonal (see **Figure 1.1c**), square supercell constructed from triangles (see **Figure 1.1d**), Kagome cell (see **Figure 1.1e**), diamond cell (see **Figure 1.1g**), and rectangular cell (see **Figure 1.1f**)

Different shapes of honeycomb can have different functions or applications involving multifunctional performance. For instance, triangular honeycombs perform better for application where high stiffness and strength in the in-plane direction is required, while metallic hexagonal or rectangular honeycombs are suitable for forced convection heat transfer[13]. In honeycomb structures, out-of-plane loading refers to loads along the longitudinal cell axis while in-plane loadings

refers to loads transverse to the cell axis. In general, cellular solids have superior multi-functionality properties compared to their solid counterparts[12].

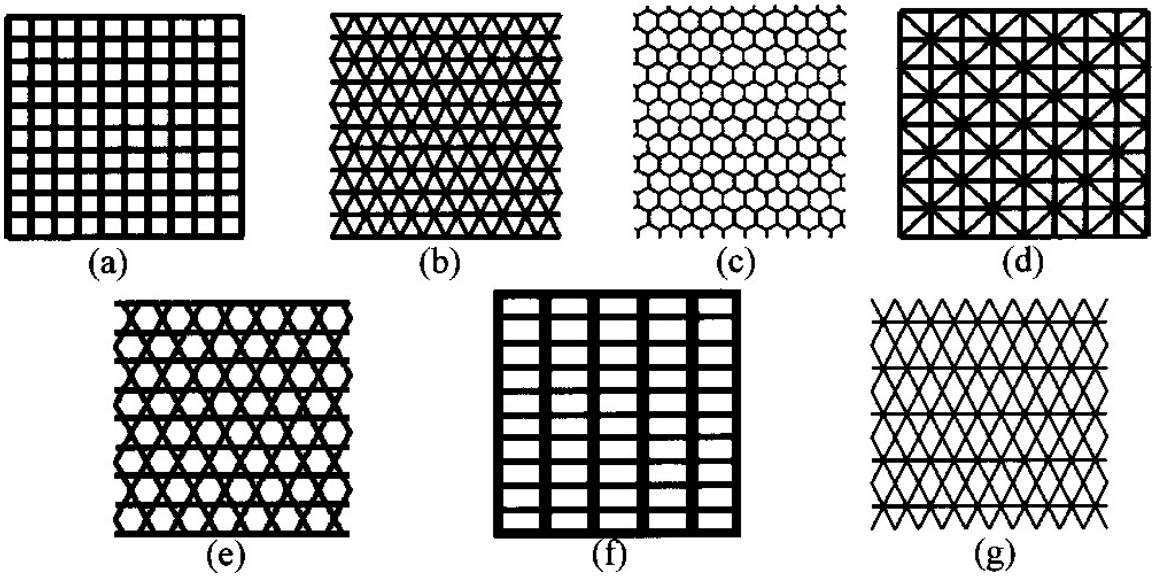

Figure 1.1 Honeycombs with different unit cell shapes of **(a)** square, **(b)** equilateral triangles, **(c)** hexagonal, **(d)** square supercells constructed from triangles, **(e)** Kagome, **(f)** rectangular and **(g)** diamond. Image taken from[14].

Rather than only changing the cell shape of honeycombs, replacing walls of honeycomb with equal-mass honeycomb lattice[15], or replacing three edge joint of honeycombs with hollow hexagonal prism[16] or hollow circles[17] can increase the Young's modulus of the new structure.

Porous materials are also ubiquitous in nature. Millions of years of evolution in nature has resulted in the interesting design patterns within the natural materials that are compatible with their surrounding environment. The patterns observed in natural porous materials are tubular and cellular structures (see **Figure 1.2a**). Tubular materials have pores that give them superior resistance to impact and piercing and are found in hooves, teeth and fish scales[18].

The function of tubules is to transfer the nutrients within the material, avoiding crack propagation, and providing ductile attachment. These result in increased energy absorption and fracture toughness by stopping or deflecting crack growth (see **Figure 1.2f**) or by collapsing the tubules when compressed[18]. They also can act as scattering centers that decrease the amplitude of longitudinal stress pulses of impact. This can be demonstrated in horn and hooves as they receive very high velocity momentum. The impact generates high amplitude waves which are scattered by tubules so its amplitude decreases significantly, which reduces damage to the tissues beneath the horn and hooves.

Cellular structures encompass open/closed cell foams or porous material with high strength to weight ratios with significant buckling and bending resistance and high toughness. These structures are usually observed in flying organisms or birds, and examples of cellular structures in nature are porcupine quills (see **Figure 1.3b**), toucan beaks (see **Figure 1.3c**), turtle shell (see **Figure 1.3d**), antlers (see **Figure 1.3e**), bird bones (see **Figure 1.3f**), horseshoe crab shells (see **Figure 1.3g**) and mammalian trabecular bone (see **Figure 1.3h**). There are two types of cellular structures, open cell structures where pores are connected to each other and make interconnected networks of porosity, and closed cell structures where individual pores are isolated and there is no connection between pores[18]. Open/closed cell structures have a similar stress-strain response—Initially , there is a linear behavior followed by a zig-zag pattern due to buckling and then a sharp increase in stress due to compaction[4].

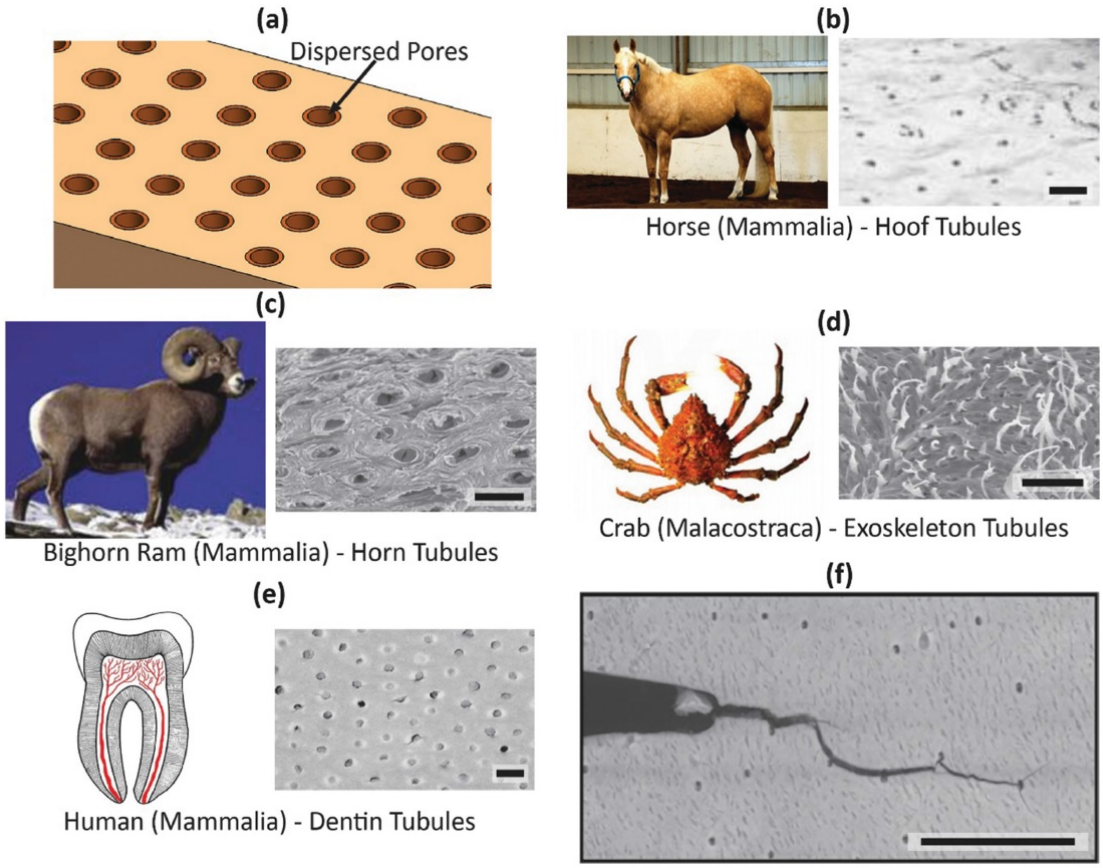

Figure 1.2 Tubular materials are made from **(a)** long pores within the bulk material; **(b)** horse hooves with a tubular pattern; **(c)** horn tubules of a Bighorn ram; **(d)** exoskeleton of carb; **(e)** tooth with dentin tubules; **(f)** Deflection of crack by tubules. Image taken from[18].

Even by coming up with an appropriate design for a specific application, the next challenge in engineering is fabrication of a designed material. Typical processing methods to fabricate porous synthetic materials include template replication[19–21], direct foaming[22–24], 3D-printing[25–27], sol-gel methods[28–30] or electrospinning[31]. All of these processing routes have varying limitations: narrow range of pore characteristics[32], difficult removal of pore-forming agent and binder[33–35], costly, intricate and high pressure components[36,37], additive toxicity, long drying procedure and troublesome polymerization reactions[38,39]; presence of

impurities[40,41], shrinkage and drying stresses[42,43]. Freeze casting is a simple technique to fabricate porous anisotropic ceramics[44–46], polymers[47–49] or metals[50–52] with high compressive strength[53]. This method has found applications in cryobiology[54], the food industry[55,56], energy storage[57,58], remediation of contaminated media[59,60], chemical analyses[9], photocatalysis[61–63], liquid chromatography[64], sensors[65–67] and pharmaceuticals[68–70]. To enhance the mechanical properties of freeze cast scaffolds in multiple directions, external magnetic fields are applied during the freeze casting process which is known as, Magnetic Freeze Casting.

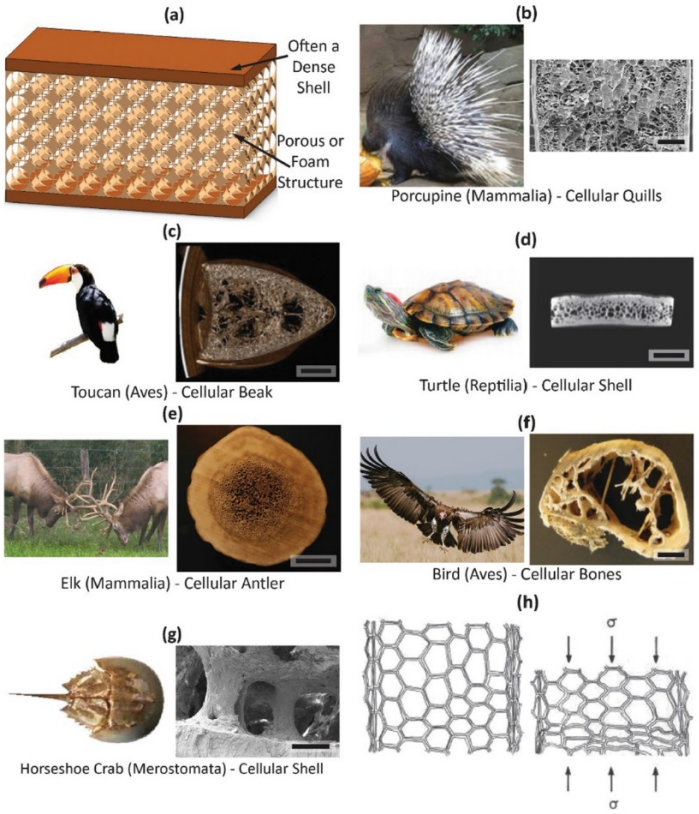

Figure 1.3 **(a)** Cellular structures in natural materials consisting of a dense outer region and porous inner region. Open and closed pores within the bulk materials of **(b)** porcupine quills; **(c)** toucan beaks; **(d)** turtle shell; **(e)** antlers; **(f)** bird bones. Image taken from[18].

In this dissertation, first, the physics of freeze casting is explained, then the use of external magnetic fields in freeze casting is investigated. To explain the physics of freeze casting, a review on thermodynamics of multi-phase systems is given in Chapter 2. In Chapter 3, the physics of freeze casting is explained and in Chapter 4, experimental studies investigating different parameters are reviewed. In Chapter 5, the magnetic freeze casting method is introduced and the underlying physics of this process is discussed in detail. Also, the effect of processing conditions on the final structure of freeze cast scaffolds is investigated. Since several parameters are playing role in the final structure of freeze cast scaffolds, in Chapter 6, by taking advantage of 3D printing, scaffolds mimicking freeze cast patterns were designed in SolidWorks and compressed in three orthogonal directions, where one parameter was changed at a time and the others were kept constant. This helped to investigate the effect of microstructure on the mechanical properties. Finally, in Chapter 7, the use of permutated radar charts to visualize multiple properties is applied to the 3D-printed scaffolds.

CHAPTER 2

REVIEW OF THERMODYNAMICS

2.1 Internal Energy

The internal energy of a system is energy contained within the system. This energy is in the form of kinetic energy of translation, vibration and rotations of molecules plus chemical energy of the system (chemical energy is manifested as energy of bonds holding molecules together)[71].

2.2 Enthalpy

According to the first law of thermodynamics, the rate of total energy change (internal energy *U*, plus, kinetic energy, $K = \frac{1}{2}mV^2$) of a control system is equal to the sum of work of external forces and heat given to the system.

$$\Delta E = \Delta(U + K) = Q + W \tag{2.1}$$

Q is the heat input to the system by conduction through boundaries (neglecting heat generation), *W* is the work done on the system by external forces, and ΔE is system's total energy change. The control system is the amount of mass considered as a system. *E*, *U* an *K* are total energies; it is more convenient to write them in terms of per unit mass and show them by lower case letters, e, u and k. By manipulating the equation (2.1) and utilizing Reynold's transport theorem[72] equation (2.1) can be written for a fixed control volume (CV; an imaginary fixed space in the flow) located in fluid flow through which flow is passing (see **Figure 1.1**). Conservation of energy for this CV is:

$$\Delta E = \underbrace{\frac{d}{dt}\int_v \rho e dv}_{\text{Total time rate of change of energy of the mass confined by CV}} = \underbrace{\int_v \frac{\partial \rho e}{\partial t} dv}_{\text{Local time rate of change of energy by time in CV}} + \underbrace{\int_v \rho e \overrightarrow{V}.\vec{n}\, dA}_{\text{Net energy flowing in/out of CV from the boundaries}} \tag{2.2}$$

In equation (2.2) Reynolds transport theorem is applied to pass the time derivative inside the integral. Substituting $e = u + k$:

$$\Delta E = \frac{d}{dt}\int_v \rho e dv = \int_v \frac{\partial \rho (u+\frac{1}{2}V^2)}{\partial t} dv + \int_v \rho (u + \frac{1}{2}V^2)\overrightarrow{V}.\vec{n}\, dA \tag{2.3}$$

dv is an infinitesimal volume within CV, $\vec{q}$ is the heat flux vector (rate of heat transfer per unit area), $\vec{n}$ is a normal unit vector on the surface pointing outward (**Figure 2.1**), *dA* is a differential surface area, ρ is the density , $\vec{V}$ is the velocity, and $V = |\vec{V}|$. Note that the integral on left side is of the volume and the integral on

right side is of the surface area enclosing CV. In equation (2.3), the time derivative on the left side is the rate of change of energy for a mass, which is confined to CV at time t. Also, at time t+dt part of this mass has left the CV because this part of the mass is moving with the flow. The first term on the right side is the local time rate of change of energy within CV, which means we have considered one fixed point within CV (without moving with flow) and are evaluating the change of energy by time at that fixed point. The second term on the right side is the amount of energy carried to/out of CV by the flow.

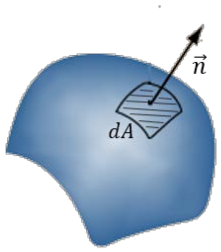

Figure 2.1 *dA* is a differential surface area and $\vec{n}$ is a vector pointing out of the control volume

Power input to the system consists of the rate of work done by external surface forces per unit area and body forces per unit volume. Examples for body forces are gravitational acceleration, electrical and magnetic forces. Then, the power input by external stresses is:

$$W = \int_A \vec{T}.\vec{V}dA + \int_v (\rho\vec{f}.\vec{V})dv \qquad (2.4)$$

where $\vec{T}$ is surface stress, and $\vec{f}$ is body force per unit mass. In fluids problems, pressure is separated from viscous stresses because viscous stresses appear in

a fluid when there is strain in the fluid while pressure exists, even if the fluid is at rest. It follows:

$$\vec{T} = \vec{t} - P\vec{n}$$

where $\vec{t}$ is the viscous stress and P is the thermodynamic pressure; $P\vec{n}$ shows the pressure is always normal to surface. The work done by pressure is demonstrated in **Figure 2.2.** On face 1, pressure is pushing the fluid into the CV and doing work on the fluid. The same thing happens at face 2 and other faces, so the net work done on CV at x direction is: $-\int_A P\vec{n}.\vec{V}dA$

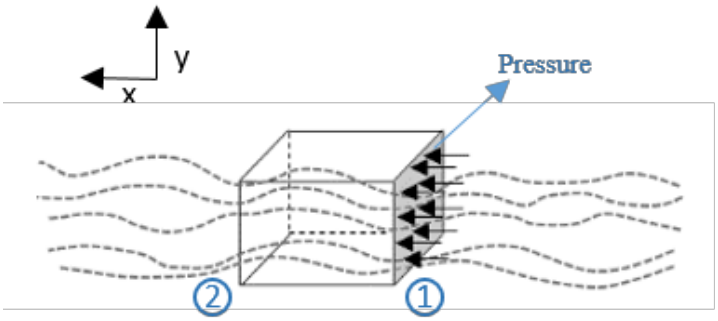

Figure 2.2 Work done on a control volume by pressure

The only body force we are considering is gravitational acceleration per unit mass denoted by $\vec{f}$.

$$W = \int_A \overrightarrow{(t} - P\vec{n}).\vec{V}dA + \int_v (\rho\vec{f}.\vec{V})dv =$$

$$-\int_A P\vec{V}.\vec{n}\,dA + \int_A \vec{t}.\vec{V}\,dA + \int_v \rho\vec{f}.\vec{V}\,dv \tag{2.5}$$

The net heat transfer to CV by conduction and neglecting heat generation is:

$$Q = -\int_A \vec{q}.\vec{n}\,dA \tag{2.6}$$

Now substituting equations (2.3)-(2.8) into (2.1), it follows:

$$\overbrace{\int_v \frac{\partial \rho\left(u+\frac{1}{2}V^2\right)}{\partial t}dv + \int_A \rho\left(u+\frac{1}{2}V^2\right)\vec{V}.\vec{n}\,dA}^{\text{Total rate of change of energy within the CV}} =$$

$$\underbrace{-\int_A P\vec{V}.\vec{n}\,dA}_{\text{Work done by pressure}} + \underbrace{\int_A \vec{t}.\vec{V}\,dA}_{\text{Work done by viscous forces}} + \underbrace{\int_v \rho\vec{f}.\vec{V}\,dv}_{\text{Work done by gravity force}} - \underbrace{\int_A \vec{q}\,.\vec{n}\,dA}_{\text{Heat transfer by conduction}} \tag{2.7}$$

By taking the first term on right side to the left side and merging it with second integral on left side:

$$\int_v \frac{\partial \rho\left(u+\frac{1}{2}V^2\right)}{\partial t}dv + \int_A \rho\left(u+\frac{P}{\rho}+\frac{1}{2}V^2\right)\vec{V}.\vec{n}\,dA =$$

$$\int_A \vec{t}.\vec{V}\,dA + \int_v \rho\vec{f}.\vec{V}\,dv - \int_A \vec{q}\,.\vec{n}\,dA \tag{2.8}$$

As in control volume analysis for fluid flows, the work done by pressure is always present; for a more compact notation a new thermodynamic property is introduced as:

$$h = u + \frac{P}{\rho}$$

where h is called enthalpy. Enthalpy is used when an energy balance is considered in fluid flow. In case we are analyzing control mass (an enclosed amount of mass with no mass transfer at the boundaries), internal energy u appears in the conservation of energy equation, because there is no inflow/outflow of mass at boundaries and pressure is not doing work at the boundaries, so the $\frac{P}{\rho}\vec{n}.\vec{V}$ term would not appear in our equations. Although motivation for defining a new property as enthalpy comes from pressure work on CV, the enthalpy notation can be used in any system analysis (since in the enthalpy definition we have properties like u, P, ρ, so it is property of substance as well).

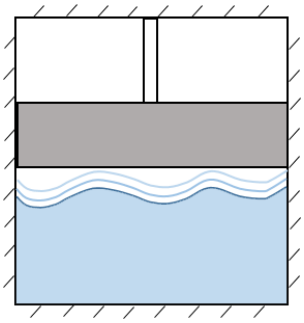

Figure 2.3 Water confined between a cylinder and piston is considered a control system because no mass flows through the boundaries.

The equation (2.8) would be:

$$\int_v \frac{\partial \rho \left(u + \frac{1}{2}V^2\right)}{\partial t} dv + \int_A \rho \left(h + \frac{1}{2}V^2\right) \vec{V}.\vec{n}\, dA =$$

$$\int_A \vec{t}.\vec{V}\, dA + \int_v \rho \vec{f}.\vec{V}\, dv - \int_A \vec{q}\,.\vec{n}\, dA \qquad (2.9)$$

In case of incompressible flow equation (2.9) can be simplified. Since gravitational acceleration is a conservative body force, we can write it as the gradient of a scalar function, such as $M = gz$, where z is a coordinate in the direction of gravitational acceleration [73].

$$\vec{f} = -\nabla M \tag{2.10}$$

Utilizing equation (2.10) in the following identity:

$$\int_v \rho \vec{f}.\vec{V}\, dv = \int_v -\rho \nabla M.\vec{V}\, dv = \int_v \left\{\nabla.\left(-\rho M \vec{V}\right) + \rho M \nabla.\vec{V}\right\} dv \tag{2.11}$$

For incompressible flow $\nabla.\vec{V} = 0$ [74] results in:

$$\int_v -\rho \nabla M.\vec{V}\, dv = \int_v \nabla.\left(-\rho M \vec{V}\right) dv$$

Applying the divergence theorem in the equation above, the volume integral would be converted to a surface integral as:

$$\int_v \nabla.\left(-\rho M \vec{V}\right) dv = -\int_A \rho M \vec{V}.\vec{n}\, dA \tag{2.12}$$

Finally substituting equation (2.12) into (2.9):

$$\int_v \frac{\partial \rho \left(u + \frac{1}{2}V^2\right)}{\partial t} dv + \int_A \rho \left(h + \frac{1}{2}V^2 + M\right) \vec{V}.\vec{n}\, dA =$$

$$\int_A \vec{t}.\vec{V}\, dA - \int_A \vec{q}\,.\vec{n}\, dA \tag{2.13}$$

where $M = gz$ is called the gravitational potential.

2. 3 Entropy

To explain Gibbs free energy, let's consider system *A* in **Figure 2.4** where a flywheel is surrounded by air in a adiabatic container. Initially the flywheel is spinning fast. By the passing of time, collision between air molecules and the flywheel will slow down, causing the air molecules to move faster (friction of bearings are neglected). The motion of gas molecules is random because we have no information regarding the magnitude and direction of each molecule's velocity at time t, while the flywheel's kinetic energy is organized because we know the velocity magnitude and direction of each mass element on the wheel at time t, $\vec{V} = \vec{\omega} \times \vec{r}$, where $\vec{r}$ is a vector pointing from the axis of spin toward the mass element). Collisions between the flywheel and air molecules will transfer organized energy from the flywheel to random motions in the air molecules. Finally, both the flywheel and air will come to rest with a slight increase in temperature (State B).

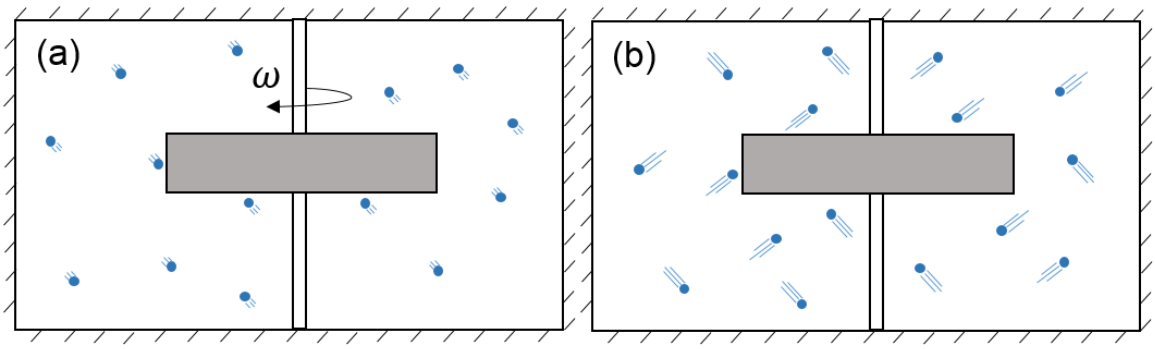

Figure 2.4 **(a)** Spinning flywheel surrounded by gas in a rigid isolated container (b**)** Flywheel is at rest and its temperature with air is increased an infinitesimal amount. Image adapted from from[75].

This increase in temperature of the wheel and gas is trivial. For example, if kinetic energy of a steel flywheel (0.5 m diameter and thickness of 10cm) spinning at 1000 rpm is converted to its internal energy, it will increase the temperature of wheel $\sim 0.35\,℃$, even if this energy is transferred to the air, container and environment, the temperature difference will be smaller.

In the initial state A, most of the energy is in a highly organized form. All of the molecules of the wheel are rotating around the axis together, and this organization makes it possible to extract that energy as useful work. We can simply attach a generator to the flywheel, provide electricity, and use this energy to raise weight, run trains, etc. But once the system has reached state B, where all the energy is microscopically disorganized, it is more difficult to extract the energy as useful work from a system whose temperature is just slightly higher than its surroundings. This produces a higher state of molecular chaos. This loss and gain always go hand in hand; whenever molecular chaos is produced, the ability to do work is reduced [75]. Hence, form state A to B the ability of the system to do useful work has decreased, while entropy of system has increased. Now the question is what is the maximum useful work that could be extracted from the system. This is done after quantifying microscopic disorder by the thermodynamics property called entropy.

Entropy measures the level of disorder in the matter, and for all processes entropy is produced or is kept constant (reversible processes) meaning it can not be decreased or destroyed (second law of thermodynamics). Associated with the production of entropy is a reduction in the amount of useful work that can be

extracted from a system. This indicates that processes would progress in the direction that entropy of system increases. Entropy also can be considered as uncertainty in a microscopic state of the matter.

If there is no uncertainty about the microscopic state, however, we should be able to capture all of the molecular energy. For example, if we know precisely the position and velocity of each molecule in a gas at each instant, we would know exactly where to hook in little molecule catchers to catch their kinetic energy, but by increasing randomness in the system causes our ability to convert all molecular energy to useful work to be reduced.

By defining entropy quantitatively, and doing energy analysis, along with the second law of thermodynamics, the maximum work that can be extracted from a given state is[76]:

$$W_{rev} = \int_v \frac{\partial \rho\left(u - T_0 s + \frac{1}{2}V^2\right)}{\partial t} dv + \int_A \rho \left(h - T_0\, s + \frac{1}{2}V^2 + M\right) \vec{V}.\vec{n}\, dA \quad (2.14)$$

where s is the entropy and T_0 is the temperature of the environment. T_0 appears in the equation because it is assumed the maximum work can be obtained when the system is reversible, and brought to the environment temperature and pressure without the need of extra work. Again similar to the analysis for enthalpy, we can introduce new thermodynamic properties defined as:

$$g = h - Ts \quad (2.15)$$

$$a = u - Ts \quad (2.16)$$

g is Gibbs free energy and a is the Helmholtz function, which emerges from the energy analysis for control systems. Note that *g* and *a* in (2.15) & (2.16) are per unit mass, and the total form is G and A. Now reversible work is:

$$W_{rev} = \int_v \frac{\partial \rho\left(a+\frac{1}{2}V^2\right)}{\partial t} dv + \int_A \rho\left(g + \frac{1}{2}V^2 + M\right)\vec{V}.\vec{n}\, dA \qquad (2.17)$$

In conclusion, if there are two systems with the same internal energy, but the first one has higher Gibbs free energy, it means we can extract more work than the first system, and that system may go from state A to B spontaneously but the reverse is not possible. Also, it follows that energy in the first system is in a more organized state than the energy in the second system. Thus, Gibbs free energy is a more important property than the internal energy.

2.4 Equilibrium

In the next chapter, to obtain the freezing point depression of two phases (i.e. a ceramic particle in water), we need to use equilibrium conditions.

In the previous section, we found that according to the second law of thermodynamics, processes tend to proceed spontaneously in the direction that increases the entropy of a system. Also, it was shown that an increase in entropy would result in less useful work that can be extracted from the system, or equivalently the system's Gibbs free energy would decrease. For isolated systems, equilibrium state is one of maximum entropy. For non-isolated system, maximum entropy is reached when the system and environment are in equilibrium with one another. In this case, the Gibbs function of the non-isolated system is a minimum and gives the equilibrium state for a system exposed to an isothermal isobaric

environment. Therefore to find equilibrium, we need to find the minimum of Gibbs function.

From a different perspective, if a system is at equilibrium, there must be no possibility that the system can do work when it is isolated from its surroundings. The first requirement is that the system must have a uniform temperature, otherwise we could operate a heat engine between points of different temperature and do work. There must also be no unbalanced mechanical forces within the systems, or a turbine could operate between the two points to do work.

Now we can obtain the equilibrium criterion in this specific example. Imagine a natural gas well (see **Figure 2.5**) that is deep, and assume that the temperature of the gas is constant through the well. Let us assume that equilibrium conditions prevail in the well. If they do, we would expect an engine such as that shown in **Figure 2.5**, which operates on the basis of pressure and composition changes with elevation, to be incapable of doing work. If we consider a steady state process ($\frac{\partial}{\partial t}$=0) for a control volume around this engine, we could apply equation (2.17):

$$\dot{W}_{rev} = m_i \left(g_i + \frac{1}{2}{V_i}^2 + gz_i\right) - m_e(g_e + \frac{1}{2}{V_e}^2 + gz_e) \tag{2.20}$$

However, because $\dot{W}_{rev} = 0$, $m_i = m_e$ and $\frac{1}{2}{V_i}^2 = \frac{1}{2}{V_e}^2$, then we can write:

$$g_i + gZ_i = g_e + gZ_e \tag{2.21}$$

And the requirement for equilibrium in the well between two levels that are a distance *dZ* apart would be:

$$dg_T + gdZ_T = 0 \tag{2.22}$$

In contrast to the deep gas well, most of the system that we consider are of such size that ΔZ is negligibly small, and therefore we consider the pressure in the system to be uniform. This leads to the general statement of equilibrium:

$$dG_{T,P} = 0 \tag{2.23}$$

Which states at equilibrium that the Gibbs function is a minimum[76].

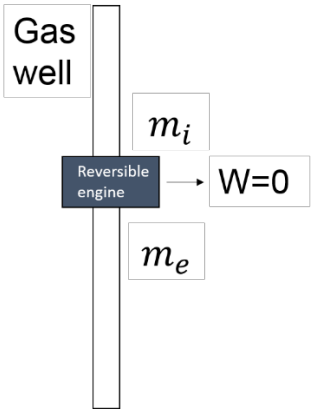

Figure 2.5 Illustration showing the relation between reversible work and the criteria for equilibrium. Image adapted from[76].

Now let's consider an isolated system consisting of a two-phase mixture, such as a gaseous water-vapor-nitrogen mixture in contact with liquid water containing nitrogen in solution. We seek the conditions of equilibrium between the two phases (**Figure 2.6**). We imagine an isolated system; the equilibrium state will be the one of maximum system entropy, selected from all possible states having the same total internal energy, volume and mass of each component. We denote the entropy of combined system by S_C and have:

$$S_C = S_A(U_A + V_A + \Pi_{1A}, \dots, \Pi_{nA}) + S_B(U_A + V + \Pi_{1B}, \dots, \Pi_{nB})$$

Where U_A is internal energy of phase A, $V_A$is volume of phase A and Π_{1A} is mass fraction of component 1 at phase A.

The isolation constraints require:

$$U_A + U_B = constant$$

$$V_A + V_B = constant$$

$$\Pi_{iA} + \Pi_{iB} = constant$$

Thus we are free to vary only $U_A, V_A, \Pi_{iA}, \ldots\ldots, \Pi_{iB}$

In seeking the maximum of S_C. The condition

$$\left(\frac{\partial S_C}{\partial U_A}\right)_{V_A,\, \Pi 1_A, \ldots, \Pi nA} = 0$$

Leads directly to

$$\frac{1}{T_A} = \frac{1}{T_B} \rightarrow T_A = T_B$$

The condition

$$\left(\frac{\partial S_C}{\partial V_A}\right)_{U_A,\, \Pi 1_A, \ldots, \Pi nA} = 0$$

Leads directly to

$$\frac{P_A}{T_A} = \frac{P_B}{T_B}\ (since\ T_A = T_{B)} \rightarrow P_A = P_B$$

The condition

$$\left(\frac{\partial S_C}{\partial \Pi_{iA}}\right)_{U_A, V_A, \Pi 1_A, \ldots, \Pi nA} = 0$$

Leads directly to

$$(\frac{\hat{\mu}_i}{T_A})_A = (\frac{\hat{\mu}_i}{T_B})_B \ \ (since\ T_A = T_{B)} \rightarrow \hat{\mu}_{iA} = \hat{\mu}_{iB}$$

Be definition

$\hat{\mu}_{1A} = \left(\frac{\partial G}{\partial \Pi_{1A}}\right)_{U_A, V_A, \Pi 2_A, \ldots, \Pi nA}$ is change in total Gibbs energy by changing constituent 1 in phase A, while internal energy and volume and other amount of constituents are held constant. $\hat{\mu}_{1A}$ is called chemical potential and in fact is Gibbs free energy per unit mass of component 1 [75].

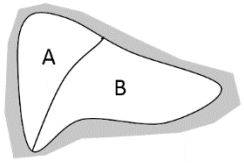

Figure 2.6 A and B represents two phases of a substance.

Consider again the system of **Figure 2.6**. Suppose that the two phases are in thermal and mechanical equilibrium, and that the electrochemical potentials of all but constituent i are equal in both phases. The entropy change of combined system associated with any interaction will then be simply

$$dS_C = dS_A + dS_B = (\frac{\hat{\mu}_{iB}}{T} - \frac{\hat{\mu}_{iA}}{T}) d\Pi_{iA}$$

Where $d\Pi_{iA}$ represents an infinitesimal number of moles of constituent i transferred from B to A. Since the combined system is isolated, the second law requires that $dS_C \geq 0$

If $\hat{\mu}_{iB} > \hat{\mu}_{iA}$ then $d\Pi_{iA} > 0$

If$\hat{\mu}_{iB} < \hat{\mu}_{iA}$ then $d\Pi_{iA} < 0$

We conclude that the electrochemical potential acts as a driving force for mass transfer. Any species will try to move from the phase having the higher electrochemical potential for that species to the phase having lower electrochemical potential.

CHAPTER 3

FREEZE CASTING

Freeze casting is a physical process to fabricate lightweight, high-strength porous materials from particulate matter that mimic the microstructures of natural materials, like nacre or bone[77]. This method can be utilized to fabricate polymers[47–49,78–80], ceramics[44–46,81,82] , metals[50,52,83,84] , gels[85], and composite systems[86–90], in which the particulate phase has a relatively low solubility in the freezing vehicle, ensuring expulsion from the ice crystals during solidification[91]. Freeze casting is of interest in many fields, such as cryobiology[92], the food industry[55,56], chemical analyses[9], and energy storage[7,93,94]. The exceptional mechanical properties of freeze cast scaffolds are mainly attributed to the complex architecture of their microstructures[95]. In this method, ceramic particles are mixed with a freezing liquid (e.g. water[77], camphene[96–99], naphthalene-camphor[100], tertiary butanol[101]) (see **Figure 3.1a**) that is directionally solidified[53,96,102]. During directional freezing, ice columns grow into the form of lamellae, pushing away particles from their

path[103,104]. Rejected particles will be trapped between ice lamellae and form ceramic columns (see **Figure 3.1b**)[105–107]. Then, the frozen solid is sublimated to remove the ice (see **Figure 3.1c**), and sintered to partially densify and strengthen the porous materials (see **Figure 3.1d**)[95].

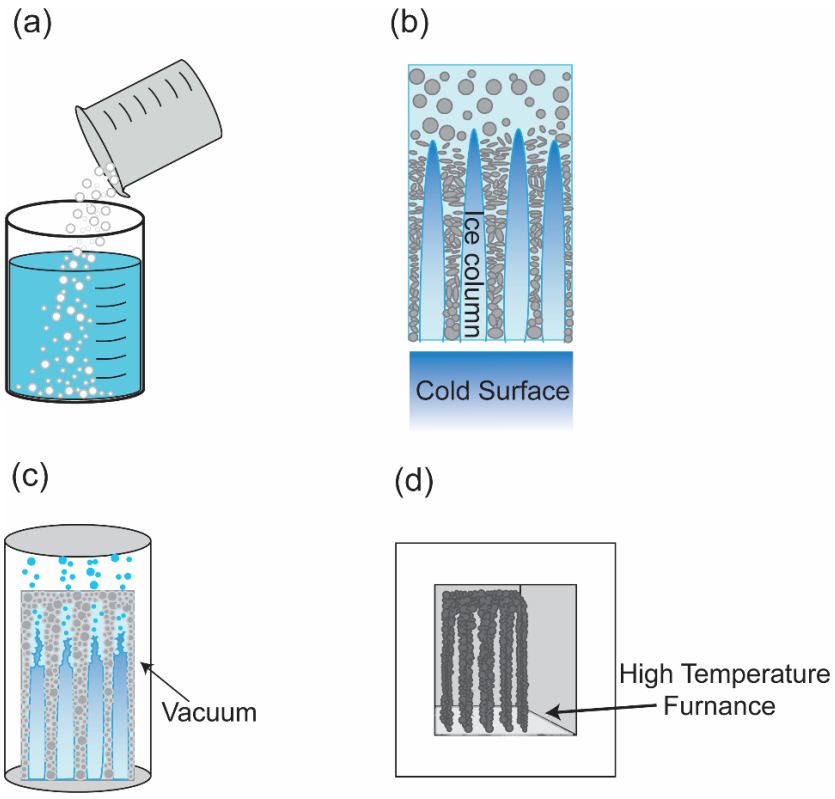

Figure 3.1 Schematic of the freeze casting. **(a)** Ceramic particles are mixed in water; **(b)** the slurry is placed on a cold surface and ice columns grow directionally; **(c)** the frozen scaffold is placed in a vacuum chamber to sublimate the ice, resulting in a porous scaffold; **(d)** the green body is sintered in a high temperature furnace to strengthen the scaffold.

In the initial slurry, a binder, dispersant, and other additives are also added. The binder acts as a “glue” to prevent the collapse of the green body (scaffolds after sublimation and before sintering process), whereas the dispersant prevents the aggregations of ceramic particles to ensure homogeneity in the slurry[77] and

various additives (e.g., polyethylene glycol (PEG)) prevent agglomeration of binder molecules and/or modify the solution's properties[108]. A freeze cast scaffold and its cross-section is shown in **Figure 3.2**. Formation of ice columns at the interface is due to the constitutional supercooling. To explain underlying physics of freeze casting, constitutional undercooling is explained in next section.

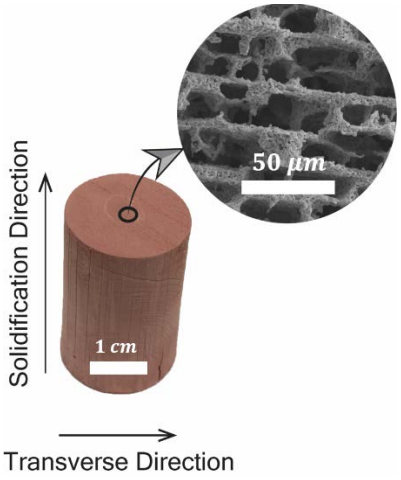

Figure 3.2 Sample scaffold fabricated by freeze casting. Freeze cast scaffolds has high strength in the longitudinal (solidification) direction while they have lower strength in the transverse direction. A close up view of scaffold cross section is shown as well.

3.1 Constitutional supercooling

When a slurry is subjected to s cold surface, at low cooling rates the freezing front velocity is slow and particles and solute molecules are repelled from the ice front and agglomerate at the interface. This is called planar solidification (see **Figure 2.3a**)[109,110]. At faster freezing velocities, due to morphological instabilities at the interface, lamellar layers of ice will be formed and start progressing into the slurry (see **Figure 2.3b**)[111]. This is reminiscent of directional solidification of binary alloys[112,113].

Agglomeration of particles at the interface will depress the freezing point of the solution at the interface, similar to salting ice in winter to melt it. Both have the same cause; adding particles/solute will decrease the chemical potential of the solvent and depress the freezing point of the solution[114]. Freezing point depression due to existence of particles/solute is called Constitutional Supercooling[1]. Supercooling can occur due to additives (e.g. binders, dispersants, or other solutes), which is called solute constitutional supercooling (SCS) or due to particles, which is called particulate constitutional supercooling (PCS). Solute supercooling is stronger than particle supercooling[115–117].

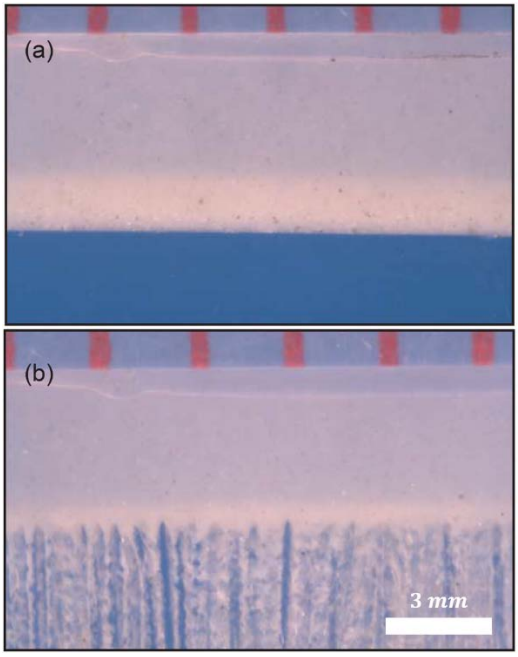

Figure 3.3 Solidification of colloidal slurry at low and high velocity. **a)** When solidification velocity is slow all the particles and solute are ejected from the ice crystals and the regime is planar solidification **b)** at the faster solidification velocities instabilities at interface are grown and make lamellar wall morphology Image taken from[111].

[1] It is called constitutional supercooling, since supercooling occurs because of the adding constituents to the solution.

By solving conservation of mass, momentum and energy for directional solidification, the temperature and concentration profiles can be obtained at the interface[111]. The profile for particle concentration is plotted in **Figure 3.4** for different ice front velocities. The freezing point of a slurry can be found at the interface (see Section 2.3)[111]. In **Figure 3.4**, the freezing point at the interface (dashed line) along with the temperature of the slurry are plotted by the assumption that the temperature profile is linear. At slow freezing front velocities, the slurry temperature at the interface is above the freezing point (**Figure 3.4a**); while at faster solidification velocities, the slurry temperature is below the freezing temperature. This metastable condition is caused by perturbations at the interface where parts of the ice protrude into the suspension. In the absence of supercooling, this perturbation will be melted back into the solution, but in supercooling, the perturbations will grow into the suspension in the form of lamellar walls (instabilities are often modeled as sinusoidal waves)[118–121]. In the case of binary alloys, these instabilities are known as Mullins-Serkerka instabilities[122].

At colloidal suspensions, Mullins-Serkerka instabilities are present at low concentrations; at higher concentrations, instability modes will change to split instability and global instability[119]. In the next section, premelting between a particle and ice is reviewed to explain freezing point depression at the interface.

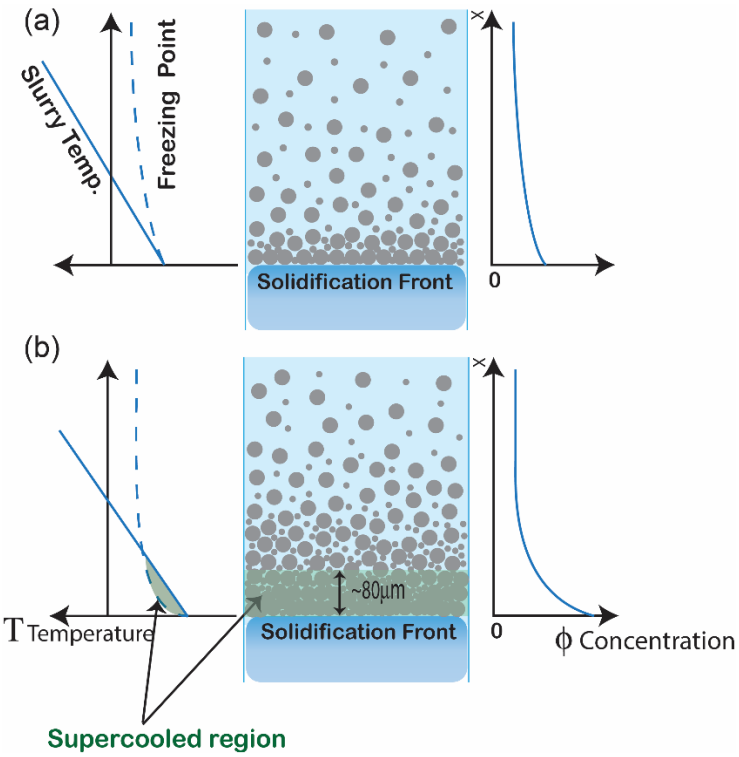

Figure 3.4 Supercooling at the solidification front. **a)** At slow solidification velocities, there is a slight increase in the particle concentration at the interface and it decades to slurry concentration smoothly. **b)** At higher solidification velocities, particles pile up at the interface and concentration decays to slurry concentration steeply. This steep concentration decrease cause slurry temperature be below the freezing point of the slurry that leads to superccoling at the interface (green area).

3.2 Premelting

Below the melting temperature (0^{o} C for water), when ice comes into contact with a solid substrate, van der Waals interactions[123,124] between molecules of ice and the substrate at the interface causes a layer of ice to melt and a thin layer of water, known as the premelted layer (2~10 nm at -1 C^{o} [125,126]), intervenes between the ice and substrate[127–135]. The slipperiness of ice and snow is ascribed to this premelted layer and its thickness is function of temperature. By decreasing the temperature, the thickness of this layer is reduced and approaches zero[136,137]. The

reason of premelting is that at the ice-substrate interface, a mismatch of atomic spacing causes strain in the solid near the interface, resulting in a buildup of energy stored in the solid phase. Introducing a liquid layer between the ice and solid relaxes these strains and decreases the free energy of the system[138]. To quantitatively explain premelting, let's first consider the case where ice is in direct contact with a solid substrate. In this case, the free energy of the interface is γ_{is}, whichis the ice-substrate interface free energy coefficient[2]. If a layer of liquid intervenes between the ice and substrate, then the free energy of the interface is $(\gamma_{ls} + \gamma_{il})$ where γ_{ls} and γ_{il} are the liquid-substrate and liquid-ice free energy coefficients, respectively. For many materials:

$$\gamma_{ls} + \gamma_{il} < \gamma_{is} \tag{3.1}$$

or

$$\Delta\gamma = \gamma_{ls} + \gamma_{il} - \gamma_{is} < 0 \tag{3.2}$$

such that the free energy of a wetted interface is less than the dry interface[136]. On the other hand, we know that below the melting point (0^{o} C for water) the free energy of a liquid is higher than ice. Therefore, the conversion of a layer of ice to liquid below the melting point increases the bulk free energy of the system. In fact, there is competition between the interface term (promoting premelting) and the conversion term (prohibiting premelting). In the case that the premelted layer is thin, the interfacial term dominates and the total free energy of system is

[2] γ is interface free energy per unit area, however the quantity measured experimentally is surface tension instead of interface free energy. Under specific condition, these can be the same as work done against surface tension to create new surface is equal to surface free energy per unit area [138].

decreased, when premelting occurs. This competition determines the thickness of the premelted layer at different temperatures[136].

An interesting phenomenon in premelted layer is the pressure difference between ice and premelted layer. Ice and water are at equilibrium with each other at 0^{o} C and a pressure of 1 atm. But, for temperatures below the melting point, if liquid water and ice are at equilibrium (in the form of a premelted layer), they must have different pressures. Wettlaufer and Worster obtained this pressure difference[139] by minimizing the free energy of a system with respect to *d* (the thickness of the premelted layer), while fixing the temperature and chemical potential of the ice and liquid. This resulted in the following relation:

$$P_M - P_s = -\rho_l q_m t_r \tag{3.3}$$

where P_M is pressure in the premelted layer, P_s is pressure in the ice, q_m is the latent heat of fusion, ρ_l is the density of the liquid, T_m is the melting temperature, *T* is the actual temperature, and $t_r = \frac{(T_m - T)}{T_m}$. This pressure difference is called the thermomolecular pressure. For example, let's consider a piece of ice with a temperature gradient across it (see **Figure 3.5a**). In colder regions the premelted layer is thinner and in warmer regions the pressure is lower, according to equation (3.3) (pressure in the ice is almost constant). This causes migration of the liquid from warmer regions to cooler regions, a process known as cryosuction[140–142]. When the liquid reaches to the colder regions and freezes (to keep an equilibrium thickness of the premelted layer), the interface deforms (see **Figure 3.5b**). This

pressure difference is the driving force for many physical phenomena like frost heaving[142–144].

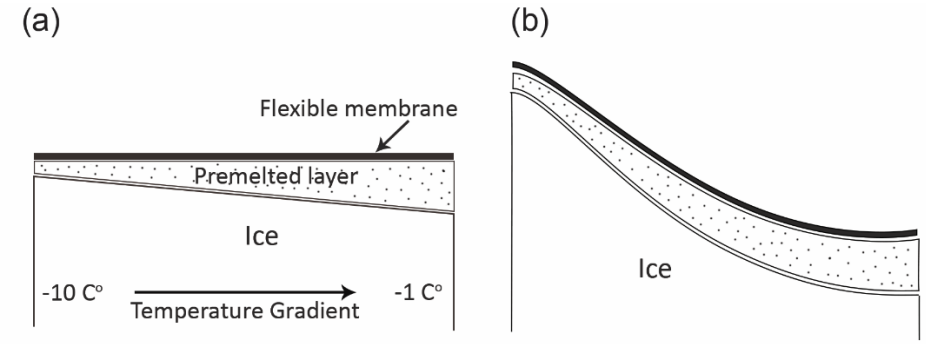

Figure 3.5 The surface of the ice is covered by the flexible membrane and temperature gradient is applied across the ice surface. **a)** In colder regions, the thickness of the premelted layer is smaller than warmer regions. Also, pressure in colder regions is lower than the warmer regions which cause flow from warmer, high pressure to colder low pressure regions. When water reaches to the cold regions, freezes (to keep the equilibrium thickness of premelted layer) and the interface shape will be deformed. Image adapted from[124].

3.3 Freezing point depression at the interface

As previously mentioned, if the solidification velocity is fast enough in a colloidal solution, accumulation of particles/solutes at the interface causes supercooling. Supercooling is due to interfacial curvature and premelting effects. A curved interface depresses the freezing point temperature, which is known as the Gibbs-Thompson effect[145–147] (see **Figure 3.6**). According to the Young-Laplace equation, there is a pressure difference between ice and water at curved interfaces, which results in a lower local freezing point than the bulk. Freezing point depression caused by interfacial curvature is given by:

$$\Delta T = \frac{\sigma_{il} T_m}{\rho_s q_m} \kappa \tag{3.4}$$

where κ is the mean curvature and σ is the surface tension between ice and water [146,148,149]. Therefore, the temperature at the ice front is below the bulk freezing point due to curvature of the interface and interfacial premelting effects. The temperature at the ice-particle interface is given by [150]:

$$T_i = T_m - \frac{\sigma_{il} T_m}{\rho_s q_m} \kappa - T_m \left(\frac{\lambda}{d}\right)^v \tag{3.5}$$

where v depends on the type of intermolecular forces; for non-retarded van der Waals $v = 3$ and for retarded and long-range electrical interactions is $v = 4$ and $v = 5$, respectively [150]. Experimental works of You et. al.[115] shows the intermolecular force effects are stronger than curvature effects on the freezing point depression, which is due to the existence of particles [151–155] or solute [156–158] at various concentrations.

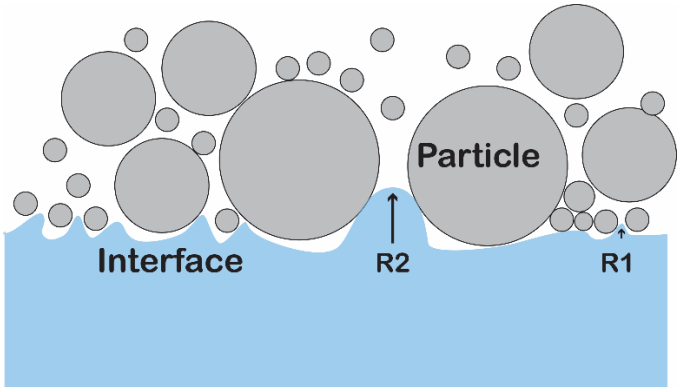

Figure 3.6 Ice for entrapping the particles should be able to penetrate into the pores between particles. Due to premelting effects between ice and particle, ice-particle interface will deform into the curved interface when ice tries to penetrate into the pores between particles.

3.3.1 Freezing point depression due to external fields

The freezing point can also be affected by external electric or magnetic fields[159]. In the liquid form, water molecules must form ice-like structures of specific size to

initiate freezing[160]. In pure undisturbed water, in the absence of any nucleation agents, water can exist as liquid as low as -48C°[161]. Freezing is often initiated by foreign substrates, which is called heterogeneous nucleation where water molecules aggregate on the substrate surface and form ice-like structures (called ice nuclei) [162]. Foreign particles in water can also act as ice nucleators. In the absence of any nucleation sites, homogeneous nucleation occurs but at much lower temperatures[163]. Strong electrical fields (10^6 V/m) can act as ice nucleators to promote freezing, which is called "Electrofreezing"[164]. Electric fields cause spatial anisotropy in ice that creates more ordered ice-like structures, promoting freezing[163,165,166]. However, unlike electric fields, magnetic fields depress the freezing point[167]. Although the mechanism of freezing point depression due to an external magnetic field is not fully understood, it is believed that magnetic fields are orienting, vibrating and spinning the molecules to prevent their aggregation, which causes supercooling[168]. It is worth mentioning that, under an external magnetic field, water acts as diamagnetic material because, under a magnetic field, the orbital motions of water electrons are altered in a way that oppose the field like diamagnetic materials[168].

3.3 Dominant forces

As discussed before, rejection of particles/solutes from the ice front and their agglomeration at the interface cause supercooling. In this section, the dominant forces that cause rejection/engulfment of particles by the ice front are considered. A force balance on a particle in a solution reveals the conditions under which particles are engulfed or rejected by the solidification front. The solidification of

colloidal suspensions was investigated for many years from point of the view of interactions of single particles with a solidification front[105,169]. These studies have explained the governing forces exerted on particles at the interface[170,171]. When the freezing front approaches a single ceramic particle, two forces are exerted on it, a repulsive force and a resistive force, also known as the lubrication force.

3.3.1 Repulsive Force

Historically two different approaches have been taken to explain the repulsive force between a particle and the ice front. Uhlmann et al.[169], Bolling and Cisse[172] and Gilpin[126,173] proposed that the presence of a particle close to the ice interface will lower the chemical potential of the liquid intervening between the particle and ice front, causing flow of the liquid from outside this region to push particles away from the interface. On the other hand, Chernov et al.[174] recognized that forces due to intermolecular interactions[3] cause the repulsion of particles from the ice front. Their analysis was later generalized by Rempel and Worster[105]. To explain the second approach, let's consider a freezing front approaching a particle. When particle is far away from the freezing front, it does not interact with the front. However, when the interface approaches a particle and the ice-particle distance reaches 0.1~0.01 microns, intermolecular interactions become dominant and Van der Waals forces between molecules in all three layers result in a net repulsive force which pushes away particles from the interface (see **Figure 3.7**). The simplest way to obtain the repulsive force is to sum the van der Waals interactions of a molecule with the

[3] These are the forces between two molecules which can be Van der Waals, electrostatic or structural forces.

surface molecules of particle and ice interface plus liquid molecules of premelted layer at the interface[174]. For non-retarded van der Waals interactions, the repulsive force per unit area is given by [105,171]:

$$P_T = \frac{A}{6\pi d^3} \equiv \frac{\rho_s q_m \lambda^3}{d^3} \tag{3.6}$$

where *A* is the Hamaker constant of the interaction between the ice and particle with a premelting layer intervening, ρ_s and q_m are the density and melting latent heat of ice, *d* is the thickness of the premelted layer, and λ is a length proportional to the interaction strength[105].

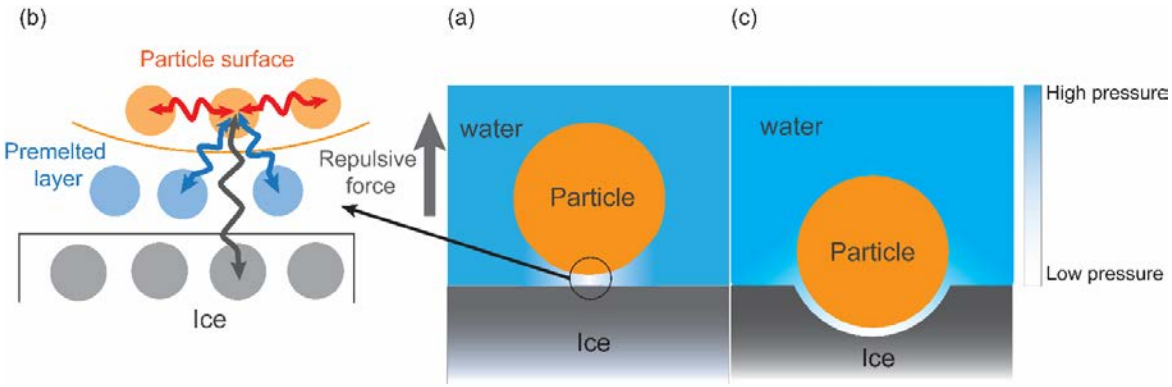

Figure 3.7 Interaction of the ice front with a particle. **a)** When particle approaches the ice front, van der Waals interaction between molecules of particle, ice and premelted layer become important. **b)** The sum of these van der Waals interactions result in a repulsive force on the particle **c)** Premelting effect between particle and ice front will deform the interface shape.

This repulsive force is called the thermomolecular pressure[175,176] or disjoining pressure in the context of wetting[177–182]. The main contribution of the repulsive force comes from the surface of the particle where it has a minimum distance from the ice front (see **Figure 3.7a**). Because this distance is small, the

repulsive force is negligible. As a result, the ice front surrounds the particle and the planar interface deforms due to premelting (see **Figure 3.7c**). This increases the contact area between the particle and the ice, thus strengthening the repulsive force. Integrating P_T over the deformed interface yields a total repulsive force[150]. Lower pressure in the premelted layer between the ice and particle causes water from the surrounding area to flow into the particle-ice front gap, keeping an equilibrium distance such that the particle is rejected from the ice front.

3.3.2 Resistive forces

Particles rejected from the ice front interface experience a resistive force which pushes them back to the interface and resists their rejection. This resistive force, which is also called the lubrication force, can be obtained by integrating the pressure around the particle [105183]:

$$F_\mu = 12\pi R^4 \mu U \int_0^{\theta_c} sin\theta cos\theta \int_{\theta_c}^{\theta} \frac{\sin \emptyset}{d^3} d\emptyset \mathrm{d}\theta \tag{3.7}$$

where R is the particle radius, μ is the viscosity, U is the particle velocity, d is the thickness of the film between the particle and ice front, and θ_c is the upper limit where thickness of liquid is bigger than thickness of premelted layer beneath the particle. At higher solidification front velocities, the resistive force dominants and the distance between the particle and ice front decreases, such that the particle is engulfed. By balancing the repulsive and resistive forces, a critical ice front velocity is obtained. When the solidification velocity is lower than the critical velocity, particles are rejected from the ice front, while at velocities higher than the critical velocity, particles are entrapped by the front. This critical velocity is given by[169]:

$$V_c = \frac{\Delta\gamma\, d}{3\,\mu\, r}\left(\frac{a_0}{d}\right)^n \quad (3.8)$$

where *r* is the diameter of the particle, μ is the viscosity, *d* is the thickness of the liquid film between particle and ice front, a_0 is the average intermolecular distance in the film, and the exponent *n* ranges from 4-5.

3.5 Processing conditions

The final microstructure of scaffolds made by freeze casting depends on the processing conditions. These processing conditions are related to the freezing and initial slurry properties.

3.5.1 Freezing properties

Freezing properties are primarily controlled by freezing velocity and direction. The freezing velocity changes the morphology of both the lamellar walls and mineral bridges. Increasing the freezing velocity results in a smaller structural wavelength, i.e., pore width plus wall thickness[184]. An empirical relationship between structure wavelength and freezing velocity is given by[185–187]:

$$\lambda = Av^{-1} \quad (3.9)$$

where λ is the structure wavelength, *v* is the freezing velocity, and *A* is a constant which depends on the solid content and particle size. By decreased the wavelength, both the pore width and wall thickness decrease[188,189]. In general, finer pore structures (i.e., thinner walls and smaller wall spacing) result in higher strength[190–194]. At higher freezing velocities, the final scaffolds are typically denser[195,196]. The freezing velocity also changes the morphology of the lamellar

walls. Increasing the velocity generally converts the lamellar morphology to a dendrite structure (see **Figure 3.8**)[184,197].

The freezing direction can be manipulated by different approaches to control scaffold morphology. For instance, a dual temperature gradient was applied by inserting a PDMS wedge between cold finger and slurry that creates vertical and horizontal temperature gradients[198]. This applies the temperature gradient both vertically and horizontally that results in uniform alignment of lamellar walls in the transverse and longitudinal directions. Another method is radial cooling to align lamellar walls in the radial direction[199,200]. In this method, the top and bottom parts of the mold are isolated the and mold is cooled from the sides[201–203] or a conductive rod is placed at the center of the mold[204,205]. Finally, to obtain constant lamellar wall spacing through the length of the scaffold, double sided cooling can be applied[186,192].

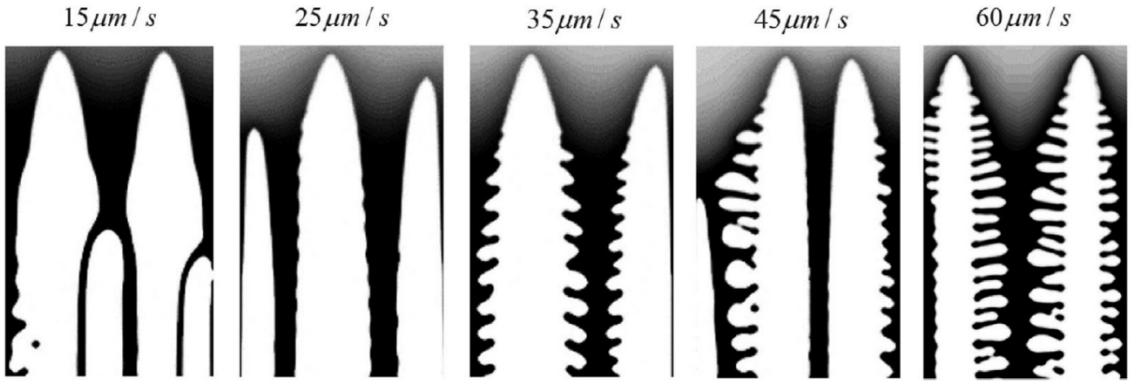

Figure 3.8 Lamellar to dendrite morphology transition due to higher freezing front velocity. Image taken from[197].

3.5.2 Colloidal properties

Colloidal properties such as particle size, initial concentration of particles, mixture composition, and additives are all factors which contribute to the final morphology of freeze cast scaffolds.

3.5.2.1 Initial concentration

The initial concentration of particles is inversely related to the porosity of the scaffolds. A higher initial concentration results in more dense structures (smaller pore width and thicker walls) and higher strength. There is linear relationship between initial concentration and porosity[206–208]. As was discussed in Section 3.1, Mullins-Serkerka instabilities occurs at low initial concentrations. However, increasing the initial concentration changes the mode of instabilities, which form spear-like patterns in the slurry. This pattern is referred to as a local split instability[119]. It is believed that this mode is different from Mullins-Serkerka instabilities[119]. Increasing the initial concentration further leads to stripe bands of particles engulfed by the ice front, which is known as a global split instability, similar to the ice banding pattern in frost heaving.

3.5.2.2 Additives

Chemical additives function as binders, dispersants, or slurry modifiers. Besides their primary functions of preventing green body collapse and particle aggregation, various additives cause morphological transitions and supercooling at the interface[115,209]. Adding polyvinyl alcohol (PVA)[210] or gelatin[211] as binder, for example, increases the formation of secondary dendrites which changes the

scaffold morphology from lamellar to dendritic[212,213]. Increasing the binder content further (to a critical threshold), increases the intensity of secondary dendrite dendrites changing the morphology to cellular[214]. You *et. al*.[115,215] observed that binders also cause supercooling at the interface. They suggested that a morphological transition occurs because of binder-induced supercooling at the interface[115], while others attribute it to the increased viscosity of the suspension[153]. Delattre et al.[117] investigated the effect of polyethylene glycol (PEG) and a dispersant on the interface morphology. They observed that adding a small amount of PEG changes the isotropic morphology to lamellar, similar to the binder effect. In their experiment, the dispersant effect was negligible compared to the binder and PEG. Increasing the PEG content further resulted in a finer microstructure (thinner walls with smaller pores) and a morphological transition from lamellar to dendritic[216–218]. Interestingly, adding NaCl leads to lamellar structures by promoting supercooling at the interface[119]. Finally, sucrose was observed to trigger a dendritic to cellular transition[221,222] and the addition of glycerol increased the density of mineral bridges connecting adjacent walls[43,151,223,224].

Other chemical additives that change the freezing properties of freeze cast slurries have also been investigated. Adding alcohols to a suspension by 5vol% increases the pore aspect ratio but beyond that (>5vol%) decreases the pore aspect ratio[219]. Pore aspect ratio is defined as the length of the major axis of a pore to its minor axis (measured from the scaffold cross-section). Increases in the pore aspect ratio due to the addition of alcohol is attributed to the formation of clathrate hydrates during freezing[220].

CHAPTER 4

EXPERIMENTAL WORKS IN FREEZE CASTING

Directional solidification of colloidal suspension is similar to directional solidification of binary alloys in many ways, but with water (or other fluids) playing the role of a fugitive second phase. Hence, in many works the solidification of colloidal suspensions is inspired by those on binary alloys[225–228]. The solidification of, colloidal solutions or binary alloys, can be classified into two categories, whose behaviors are totally different from each other: dilute suspensions and concentrated suspensions. In dilute suspensions, particle-particle interactions are neglected, while in concentrated suspensions this cannot be neglected and plays a crucial role in the morphology of the frozen phase.

In the case of dilute suspensions, for many years the problem has been investigated based on interaction of a single particle with an ice front[105,229–232]. As a suspension is diluted, the interactions between particles are neglected. Based

on these studies[105,229–232], there is a critical velocity of the ice front, which for velocities above that particles are entrapped while at velocities below that particles are rejected. For a particle to be rejected by ice front it is necessary that a thin layer of water intervenes between the particle and ice front to supply molecules to the growing crystals. By increasing the solidification velocity, the thickness of this film is reduced which hinders transport of water to the gap, such that the particle is engulfed by the ice front[186]. The critical velocity can be obtained by considering a force balance at the ice front[107,232]:

$$v_c = \frac{\Delta\sigma d}{3\eta R}\left(\frac{a_0}{d}\right)^z \tag{4.1}$$

where d is the premelted layer thickness, a_0 is the average intermolecular distance, η is the viscosity, R is the particle radius, and z is the exponent, which ranges from 1-5[169]. A low solidification velocity is shown in **Figure 4.1** where particles are repelled from the interface. For concentrated suspensions, at very low solidification velocities, particles are rejected from the interface similar to the dilute case. By increasing the ice front speed, a concentrated layer forms in front of the planar interface which lowers the thermodynamic solidification temperature ahead of the interface and leads to Mullins-Sekerka instabilities that turns the planar interface to lamellar (see **Figure 4.1**). By further increasing the ice front velocity, particles are entrapped by the ice front and an isotropic microstructure is formed (see **Figure 4.2**).

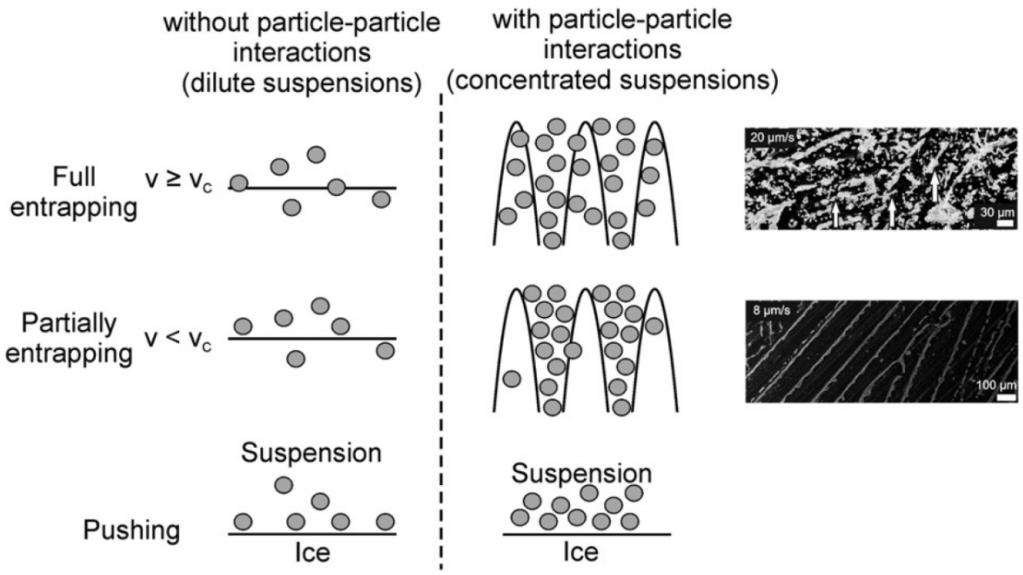

Figure 4.1 Interaction of the ice front interface with particles at low to high solidification velocities. Image taken from[185].

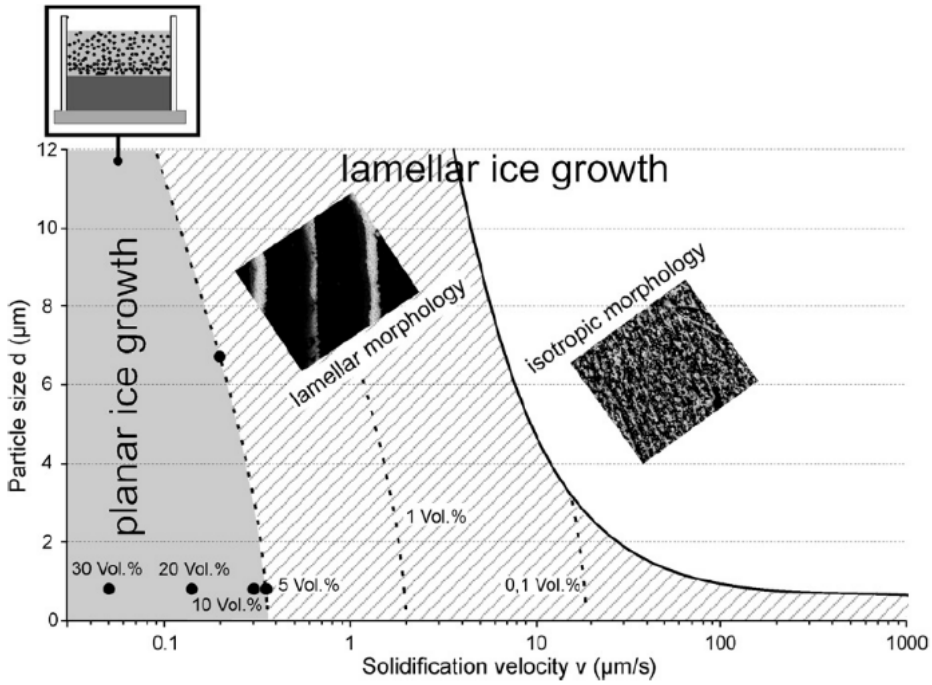

Figure 4.2 Microstructure morphology dependent on particle size and solidification velocity. Image taken from[185].

Observations of the microstructure when a suspension is exposed to a very cold surface suggests that the initial solidification velocity (the initial 10 μm) is very high and all particles are entrapped by the ice front, such that an isotropic morphology is formed (see **Figure 4.3**). The solidified suspension acts like an insulator between the cold surface and ice front, and decreases the ice front velocity. A reduced solidification velocity results in the formation of a cellular morphology. Further increasing the solidification velocity results in a change from cellular to a lamellar/dendritic morphology.

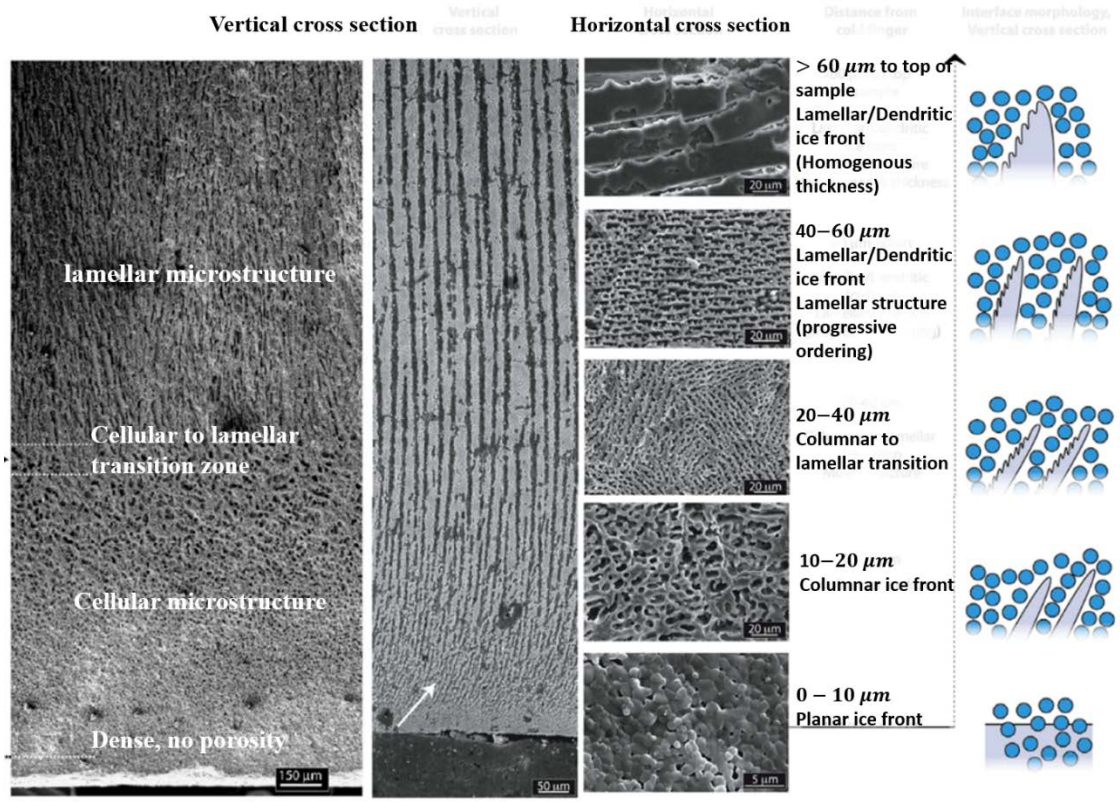

Figure 4.3 SEM image of longitudinal view showing the evolution of the ice front at different heights. Image adapted from[184].

At very high solidification velocities, it is observed that ice crystals are inclined due to growth directions: parallel to the solidification direction and preferred crystal growth direction (in sense of interfacial energies)[234,235] (see **Figure 4.4**). The analysis in the previous section based on the idea of Mullins & Sekerka instabilities is the reason for this transition from planar to dendritic solidification in binary alloys. In Mullins & Sekerka instabilities, migration of particles at the suspension/ice interface is modeled by diffusion.

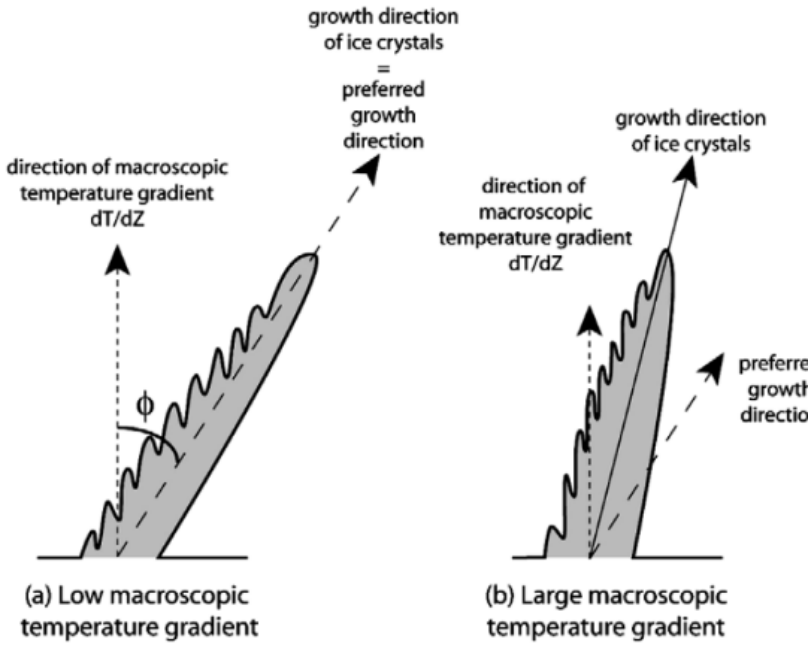

Figure 4.4 Solidification direction and preferred direction for growth of ice crystals at low and high temperature gradients. Image adapted from[186].

4.1 Segregated ice lenses versus lamellar morphology

As discussed in Section 3, binders and dispersants are added to a slurry to prevent collapse of the green body and avoiding flocculation of ceramic particles, respectively. It is found that binders and other additives not only acts as a glue to

stabilize the green body, but also change pattern formation during solidification[108]. If the binder is removed from the initial slurry, segregated ice lenses would form rather than dendritic patterns (see **Figure 4.5**). This is also shown in **Figure 4.6a** in which segregated ice lenses are formed in region three with 0.1 wt% binder. Region one is a fast freezing dense layer and region four is an accumulated dense layer of particles in front of the ice-suspension interface. In **Figure 4.6b**, adding 1.5 wt% binder resulted in the formation of a lamellar zone (**Figure 4.6b** region two). The length of this region increases by increasing the binder concentration up to 2 wt%. During these experiments, the velocity of interface was nearly constant, inferring that changes in freezing regimes were due to the effect of additives and not the freezing velocity[108].

4.2 Solute versus particle constitutional supercooling

To explain the reasons for different freezing regimes (segregated vs. lamellar) we need to clarify between different interfacial supercooling phenomena that occur in the solidification of suspensions: Solute Constitutional Supercooling (SCS) versus Particle Constitutional Supercooling (PCS). SCS is caused by additives[107,108,236] while PCS is caused by particles. To investigate the effect of PCS and SCS on freezing of colloidal suspensions and supernatant, an apparatus with two adjacent cells, one containing a suspension and the other supernatant are shown in **Figure 4.7**. The first system contained polystyrene (PS) microspheres with average particle size of 1.73 µm and initial volume fraction of 33% dispersed in deionized water[209].

Figure 4.5 Ice lenses formed by the directional solidification of kaolinite clay. Image taken from[111].

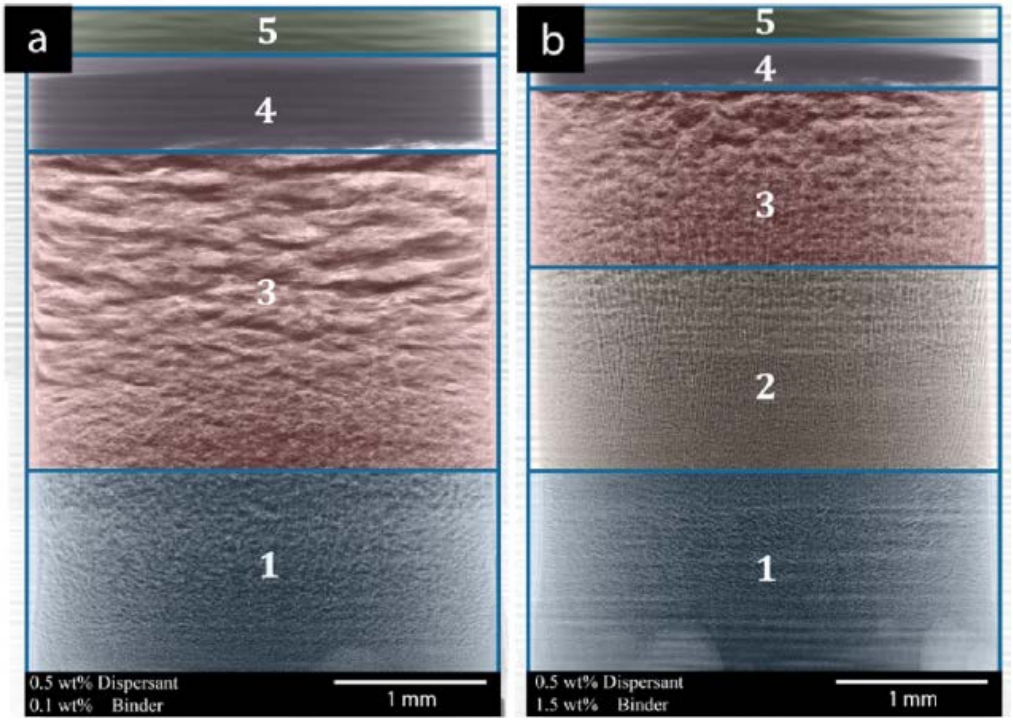

Figure 4.6 Effect of binder on solidification regimes. Different freezing zones for **(a)** 0.5 wt % of dispersant and 0.1 wt % of binder and **(b)** 0.5 wt % of dispersant and 1.5 wt % of binder. In **(b)** a lamellar pattern emerged after the fast-growth regime and the length of this region was increased by increasing the binder content. (1) fast growing region, (2) lamellar pattern, (3) segregated regime, (4) the particle-build-up zone, (5) the liquid phase. Image taken from[108].

In **Figure 4.8a** SCS supercooling was measured between the deionized water and supernatant by comparing the interface position. The upper end of the cell (in **Figure 4.7** down part is cold side and up part is warm side) is the heating zone, while the lower end of the cell is the cooling zone, which creates a linear thermal gradient G = 7.23 K/cm. In **Figure 4.8a**, the position of the solid/liquid interface in the cell of deionized water is much higher than that of the supernatant, which indicates that the freezing point of the deionized water is much higher than that of the supernatant. On the other hand, comparison of the interfacial position between the colloidal suspension and its supernatant is shown in **Figure 4.8b**, which shows particle supercooling. The interfacial position of the supernatant is almost identical to that of the suspension, which means that the freezing point of the supernatant is almost the same. Therefore, PCS is almost undetectable and should be smaller than 0.01 K if it exists in this colloidal suspensions system. Consequently, in **Figure 4.8a**, the interfacial undercooling of colloidal suspensions mainly comes from SCS. To further confirm this conclusion, the interfacial undercooling of suspensions with particles of different diameters and different volume fractions were measured. All the results are similar to that in **Figure 4.8a**.

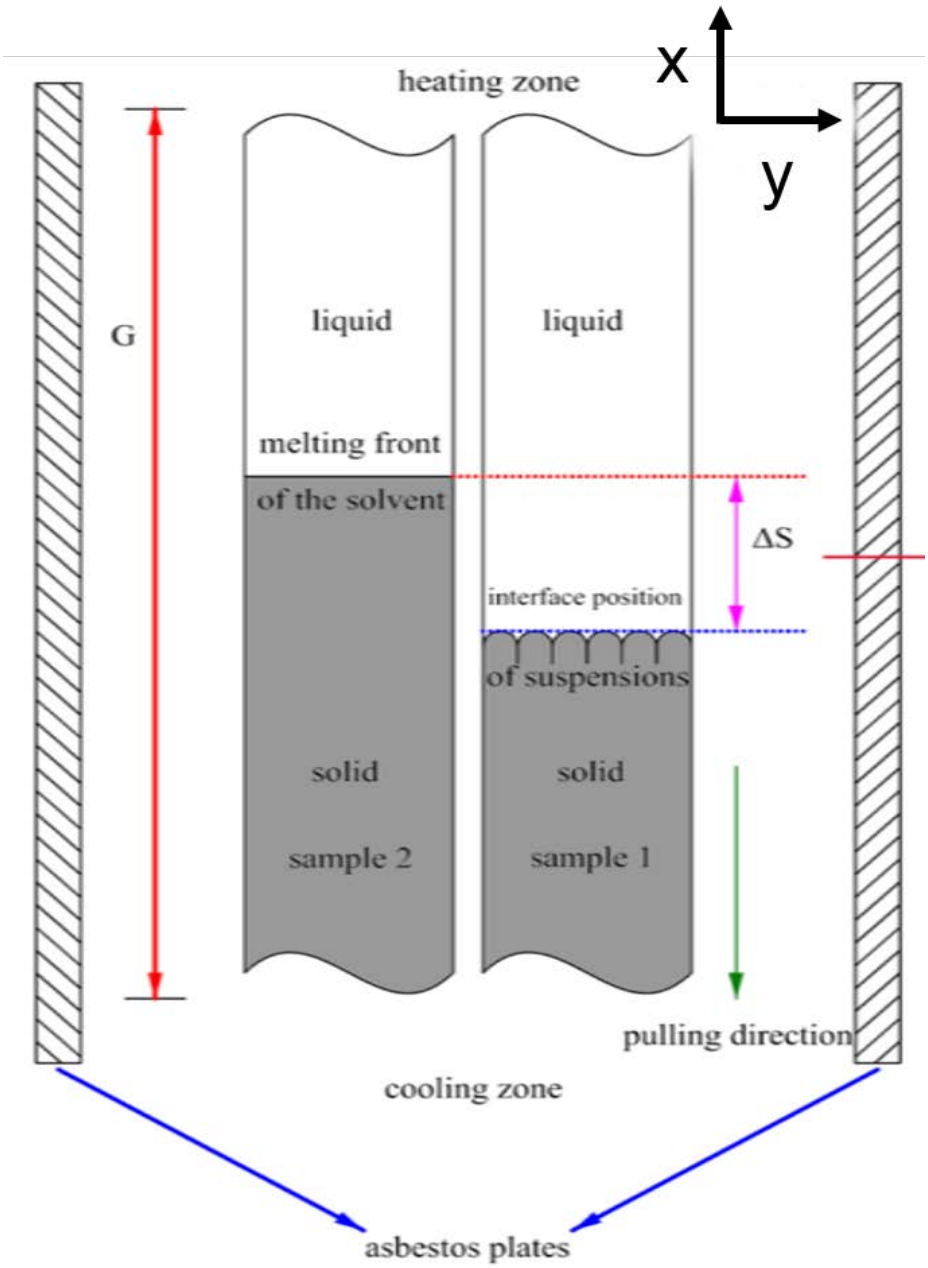

Figure 4.7 Experimental setup for measurements of undercooling. Supernatant and colloidal suspension are placed next to each other and are pulled. Two heat exchanger are creating temperature gradient. Image taken from[209].

One more interesting observation was undercooling of α-alumina suspensions. Supernatant and suspension of α-alumina at different concentrations and thermal gradients were measured[209]. In static measurements, the

undercooling in all concentrations and thermal gradients are very small and negligible while at dynamic measurements undercooling in the supernatant was noticeable and in the suspension was also negligible, emphasizing the effect of SCS rather than PCS in dynamic undercooling. The dynamic SCS varies with different pulling velocities; increasing pulling velocity results in smaller undercooling[209]. Based on the above systematic measurements, PCS is minor in both static and dynamic cases; in contrast, the effect of SCS is dominant.

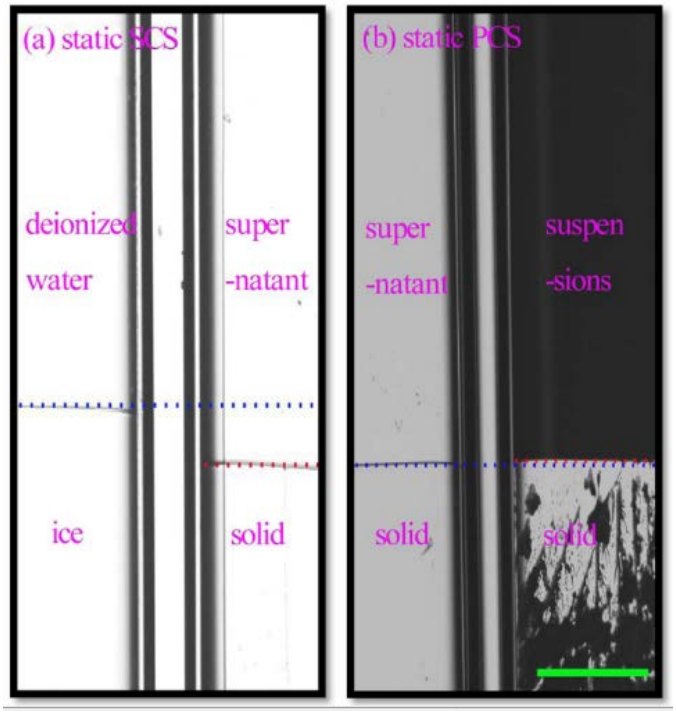

Figure 4.8 Undercooling measurements from **(a)** supernatant (solute effect) and **(b)** colloidal suspension (particle effect). Image taken from[209].

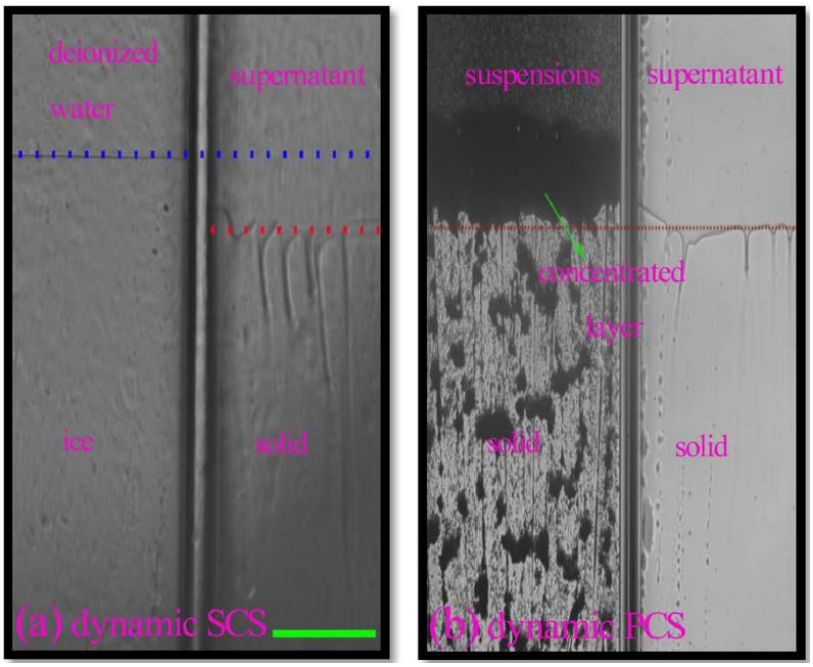

Figure 4. 9 Hele-Shaw cells of alumina suspensions to measure undercooling at a freezing velocity of V = 8.217 μm/s for **(a)** supernatant and **(b)** colloidal suspension[209]. Image taken from[209].

4.3 Interfacial instability modes

PCS and SCS result in different interfacial instability modes. The instability of the supernatant obeys classical MS instability dynamics which has been well predicted by time-dependent instability analysis[144,237]. However, the instability processes of colloidal suspensions are of great difference from the supernatant system and depend on their particle volume fractions. The directional freezing of colloidal suspensions with small particle volume fraction undergoes the similar process as that of the supernatant, as shown in **Figure 4.10a**. The interface instability also starts from fluctuation and then develops into a cellular structure[238]. However, as the volume fraction increases, the instability mode changes. As shown in **Figure 4.10b**, the cellular instability disappears. Instead, the

accumulated particle layer is split and trapped in the ice at the onset of planar instability in colloidal suspensions, this type of instability is called local split instability. Moreover, this kind of instability happens much earlier than the cellular instability mode.

As the volume fraction further increases, the accumulated particle layer is split into stripe bands as shown in **Figure 4.10c**. The instability mode is similar to the local split instability mode shown in **Figure 4.10b**, but here the split block is a stripe band jointed with an ice lens. The spears penetrate the accumulated particle layer and then grow laterally to form the ice lens, called “global split instability” or ice lenses. This kind of instability mode is almost irrelevant from the MS instability of the supernatant. The accumulated particle boundary layer will split even if the planar interface of the supernatant is stable with a pulling velocity smaller than the critical one[238].

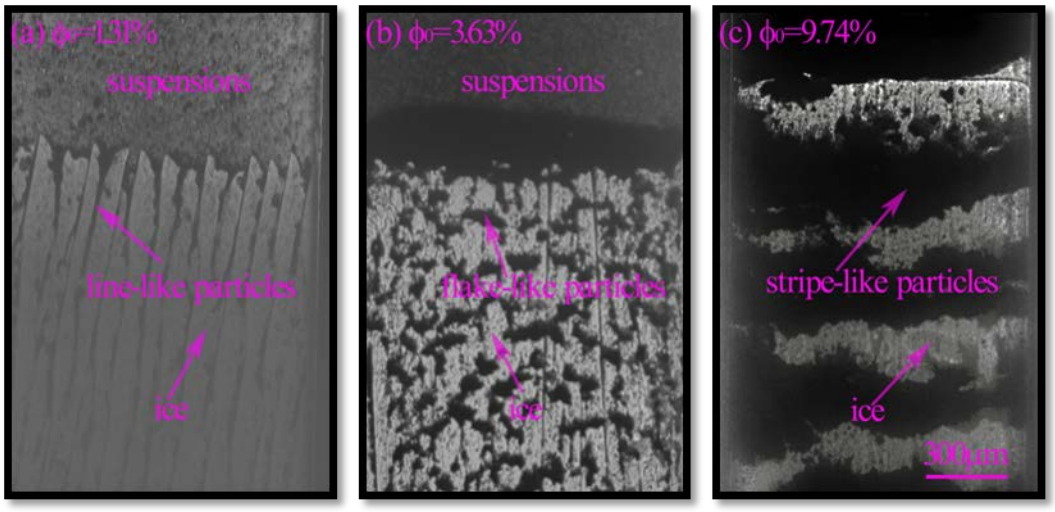

Figure 4.10 Freezing morphology for different initial concentrations at a thermal gradient of G=7.23K/cm and freezing speed V=16m/s[238]. **(a)** Cellular instability, **(b)** local split instability and **(c)** global split instability. Image taken from[209].

4.3.1 The origin of interface instability

As shown in the MS instability analysis, the interface instability is related to the solute boundary layer ahead of the planar interface. However, there are two types of boundary layers in the freezing of colloidal suspensions, i.e., solute boundary layer and particle boundary layer. For a one dimensional boundary diffusion problem, the profiles of solute concentration and particle volume fraction along the system are schematically shown in **Figure 4.14a&b** respectively. The time-dependent solute concentration and particle volume fraction in front of the solid/liquid interface is shown by connecting the interface concentration at the liquid side, as shown by the black thick lines in **Figure 4.14a&b**. The particle concentration in front of the interface will rapidly increase to the maximum volume fraction of particles φ_{max} within a very short time, as shown in **Figure 4.14b**. Furthermore, the length scale of the equivalent particle diffused layer can be ignored, compared with that of the solute diffused layer, indicating that the diffusion of particles is negligible.

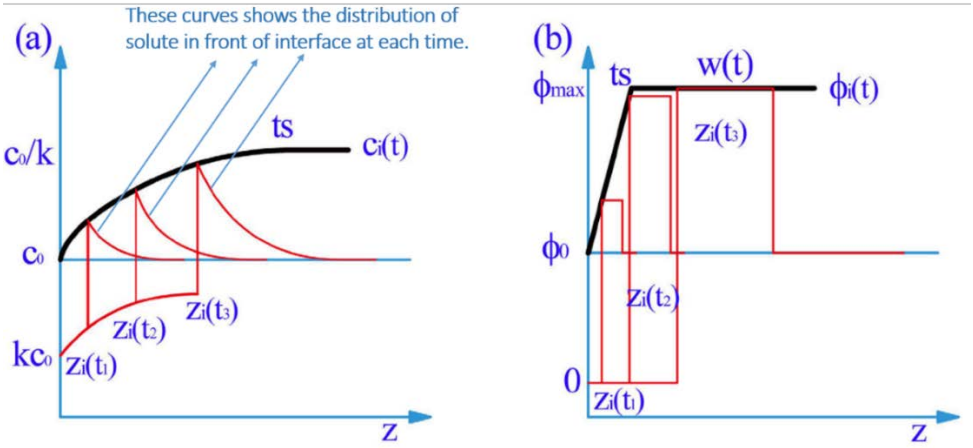

Figure 4. 11 Sketches of the time-dependent (**a**) solute concentration and (**b**) particle volume fraction at the interface[238]. Thin red lines are profiles of solute/particle boundaries for a given time. t_s is the time to reach steady state, c_0 is the initial concentration, c_i is the concentration at the interface, z_i is the interface position, and k is a partition factor. Image taken from[209].

Considering the accumulated boundary layers of solute and particle, the three interface instability modes observed in **Figure 4.10** can be well understood. First, the cellular instability is determined by the MS instability from the accumulated solute boundary layer. After the interface instability, particles are submerged into the intercellular space and the particle layer exists within a limited width. Interfacial instability of the supernatant and colloidal suspension occurs almost at the same time because the effect of the particles is negligible. Second, when particle accumulation is dominant, the whole interface is entrapped by the ice front in global split instability and patterns similar to ice lenses are formed. Third, local split instability mode occurs when solute and particle boundary layer have the same level of influence[238].

In the pattern formation of directional solidification, it is accepted that the MS instability causes the cellular morphology. Also, MS instabilities happen at a

velocity larger than the critical criterion in directional solidification[239]. At a velocity below the critical velocity, the planar interface is stable in the supernatant system, while the local split instability occurs in the colloidal suspension. At a freezing velocity larger than the critical velocity, the interface propagates with a cellular morphology in the supernatant system, and the local split particle clusters become smaller and smaller in the colloidal suspension.

The experimental results indicate that increasing solute effects gradually change the local split morphologies and may induce cellular structures as the freezing velocity further increases. As solute effects can greatly enhance the planar instability, increasing the content of additives will change the interface morphologies. In order to understand competition between solute effects and particle effects, NaCl was added into the system. The addition of NaCl almost does not change the viscosity of the system. Moreover, NaCl is an inorganic small molecular compound, neither a binder nor dispersant. The experimental results are shown in **Figure 4.15**. It shows that the global split instability mode in **Figure 4.15a** is totally changed into the cellular instability mode by only a small amount of NaCl (1%wt of particle amount). Accordingly, it is suggested that the transition from ice banding to cellular structure comes from the increasing of solute effects on the interface instability[238].

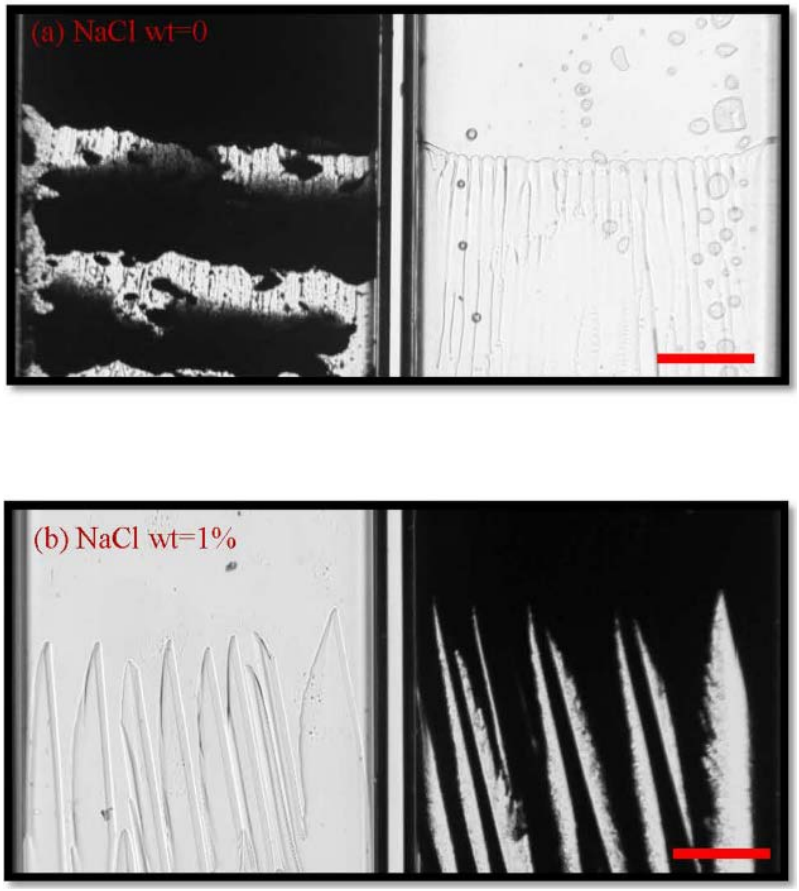

Figure 4.12 Freezing regime of **(a)** supernatant and **(b)** supernatant with 1 %wt. sodium chloride (NaCl). Image taken from[238].

4.4 Microstructural architecture and mechanical properties

Apart from attempts in trying to analyze the process analytically[111,118], numerically[240], and experimentally[102,104,106,241], freeze cast scaffolds exhibit unique microstructural features. Usually these microstructural features are organized, layered structures or contain the presence of fibrous elements that affect the mechanical properties of the material[242]. This indicates that mechanical properties could be tailored by controlling the microstructure of scaffolds. Some microstructural characteristics include pore size, lamellar wall thickness and spacing, bridge length (see **Figure 4.4**), interlamellar porosity, and overall porosity.

As expected, overall porosity has the biggest effect on strength, as the porosity increases strength decreases[243]. By decreasing the lamellar wall spacing strength is increased more than twofold[190]. Smaller pore size increases the strength by reducing the volume of struts and therefore the probability of catastrophic defects[193]. Smaller pore area and smaller aspect ratio also provided increased strength[194,219]. By increased number of domains and bridge densities and decreased thickness of the walls (and increased density of walls) by less than half, the strength increases by almost an order of magnitude[191]. Interlamellar porosity affects the strength of scaffolds too[243]. In magnetic freeze casting, longer mineral bridges (see **Figure 4.2a**) resulted in higher strength of scaffolds in the corresponding direction[244]. As noticed, alteration of the microstructural architecture or features result in changed mechanical properties. Hence, it is important to have control over microstructure by manipulating the processing conditions in order to tailor the mechanical properties as desired.

4.5 Processing conditions

Knowing the influence of microstructure on mechanical properties, it is important to determine what processing parameters affect microstructure. These parameters are solidification front velocity, particle size, solid loading, additives, etc[102]. Lamellar wall spacing (structure wavelength), an important microstructure, is a physical manifestation of the wavelength of instabilities. The factors that influence lamellar wall spacing and approaches that predict this spacing are discussed here in terms of processing conditions.

4.5.1 Solidification velocity

4.5.1.1 Achieving constant velocity during solidification

When a slurry is exposed to a cold surface with constant temperature, an ice front velocity decreases with time as a result of increased thermal resistance from the ice. This leads to an increasing lamellar spacing through the height[192]. To investigate the effect of velocity on lamellae spacing constant velocity during the solidification need to be obtained. So before proceeding with effect of velocity on lamellae spacing it is necessary to demonstrate how constant velocity can be achieved. To address this issue two remedies exist: first, an exponential cooling function must be used at cold surface; second, a double-side cooling experimental setup must be used with corresponding cooling functions at the cold surfaces.

In 1889, J. Stefan studied the formation of ice in oceans. He considered the cooling of water from atmosphere and solved the heat equation to model the problem[245]. This was the first known mathematical modeling of directional solidification without considering convection. Because phase change occurs at the ice-water interface, this problem has a moving boundary layer. Due to this study, problems involving moving boundaries are often called Stefan problems. By solving the Stefan problem with appropriate boundary conditions, the following cooling function must be applied at the cold surface to have constant velocity during solidification[246]:

$$f(t) = T_0(t) + \frac{h_f}{c_s}\left[1 - \exp\left(\frac{{v_f}^2}{k_s}t\right)\right] \tag{4.2}$$

where h_f is the latent heat of fusion, $k = \frac{\lambda_s}{\rho_s C_s}$ is the thermal diffusivity, ρ_s is the density, C_s is the specific heat, and λ_s is the conductivity of the solid phase. V_f represents the ice front velocity and T_0 is the freezing temperature of the liquid. The other end of the mold is exposed to the environment.

The other approach using a double-side (DS) cooling setup is shown in **Figure 4.5**. In DS setup, a slurry is cooled from both the top and bottom surfaces. In this case, the Stefan problem is solved by a quasi-stable approximation and the following relation is obtained[192]:

$$T_0(t) = T_0 - h_f \rho \left(\frac{{v_f}^2 t}{\lambda} + \frac{v_f \delta_w}{\lambda_w} + \frac{v_f}{\alpha}\right) \tag{4.3}$$

where δ_w and λ_w are the thickness and thermal conductivity of the plate, α is the heat transfer coefficient, λ is the thermal conductivity and ρ is the density of the liquid. Thermal conductivities in equation 4.3 for the solid phase were calculated with the Krischer model[192].

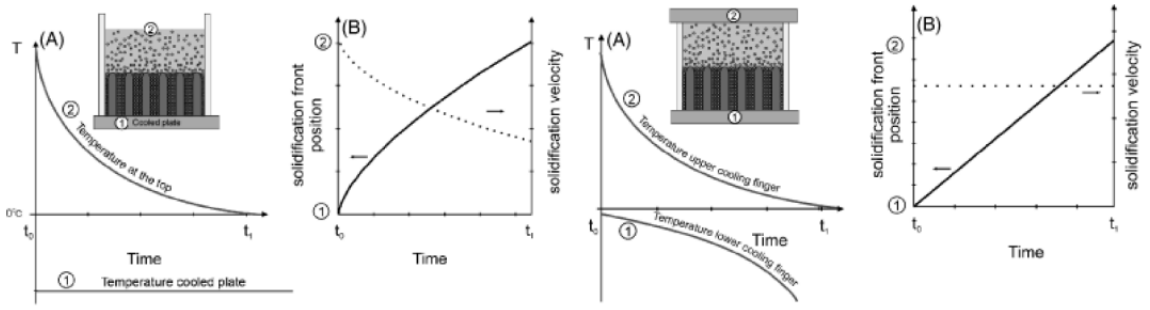

Figure 4.13 Schematic of the (a) single-side cooling setup and (b) right, double-side cooling setup. Image adapted from[192].

Note that in the first approach (single side cooling) the temperature profile at the cold surface has an exponential form and in DS cooling it has a linear dependence with time. This is the advantage of DS cooling, as longer scaffolds can be fabricated. In single-side cooling there is a limitation of maximum height of the scaffolds.

4.5.1.2 Effect of velocity on lamellar spacing

Now, with constant velocity during solidification, we can investigate the effect of velocity on lamellar spacing. Increasing freezing velocity will result in thinner walls with smaller spacing between them[186,192]. The relationship between freezing velocity and lamellar spacing can be shown by $\lambda \sim v^{-n}$[186] where n depends on the particle size[107]. Waschkies et al.[185] proposed a similar relation for lamellar spacing as

$$\lambda = Av^{-1} \tag{4.4}$$

where the prefactor *A* depends on the solid content and particle size. The significance of these two studies[185186] is that they have done measurements on green samples while the others have carried out measurements on sintered bodies whose microstructure is affected by sintering artefacts and binder additives[247].

4.5.2 Additive concentration

Increasing the concentration of particles increases the effect of particle-particle interactions and affects parameters of the system, such as the diffusion coefficient and freezing point. Also, additives provide control over the final microstructure or change the degree of constitutional supercooling[108,191,209]. For example, adding acetic acid or ethanol changed the pore size of the final structure, which results in

a linear relationship between the concentration of acetic acid and final pore dimensions. By adding more acetic acid, pore dimensions and lamellar spacing become larger[49,158]. It is observed that by increasing the solid contents, *A* is increased in equation 4.4 and the lamellar spacing is shifted to larger values[185]. Although there are studies investigating the influence of concentration qualitatively, there is no known quantitative study that explains the relationship between lamellar spacing and concentration of additives.

4.5.3 Particle size

For the first instances of solidification at the cold surface, particles provide nucleation sites for the initiation of ice crystals. Smaller particles have larger surface area and provide greater surfaces for nucleation. Hence, large particles trigger higher supercooling. Greater supercooling results in higher initial freezing velocity and causes larger structural gradients in final scaffold[225]. Also, particle size influences the spacing of lamellae. With increasing particle size, the prefactor *A* in equation 4.4 is also increased and shifts lamellar spacing to larger values[185].

4.6 Microstructure prediction

Freeze casting is not only used for fabrication of ceramics but can also be applied to polymers[47] and metals[50]. In fact, this method can be applied to any two phase system as long as the second phase has low solubility in water (or any other freezing vehicle) which ensures its segregation during solidification[91]. Different ceramic materials have been made by this method such as, silicon nitride[248], NiO-YSZ[201], polymeric materials[107] and TiO_2, ZrO_2, alumina, and hydroxyapatite[249]. As the physics of the process are the same, it is expected that the final structure is

predictable regardless of material. In this way, there have been attempts to predict lamellar spacing based on parameters of the system. Zhang et al.[107] used the equation for the wavelength of instability found from linear stability analysis for binary alloys and calculated the spacing as 15μm for colloidal suspension of silica nanoparticles. Measurements of lamellar walls were 10 μm which was close to the predicted value. Trivedi & Kurz[250] postulated that three underlying phenomena play a role in solidification, based on diffusion, thermal, and capillary characteristic lengths in binary alloys. Inspired by their method, Flauder et al[190] used these characteristic lengths to predict the lamellar spacing for colloidal suspensions. First, although both processes are similar, there are major differences between them. As discussed earlier, particle size and the concentration of particles in the suspension plays a crucial role in the morphology of colloidal suspensions, but these parameters are not seen in the equation suggested for binary alloys. So far there has been great effort to predict lamellar spacing (which are consistent through the cross section) in scaffolds, but there has yet to be a general equation to predict lamellar spacing for different processing conditions.

CHAPTER 5

MAGNETIC FREEZE CASTING

Ceramic scaffolds made by freeze casting often exhibit excellent compressive properties in the solidification direction but lack high strength and stiffness in the transverse direction. To enhance the compressive properties in the transverse direction, a few approaches have been developed, including templated grain growth[251], bidirectional freezing[198,252], freezing under flow[251,253], or magnetic field alignment[249,254]. In magnetic field aligned freeze casting, magnetic or magnetized particles are manipulated by an external magnetic field during solidification[255,256]. External magnetic fields can be oriented axially, radially or transversely (see **Figure 5.1**). The magnetic field causes the magnetic/magnetized particles to reorient and/or cluster into directionally aligned chains in the magnetic field direction (see **Figure 5.2**)[255,256], leveraging similar mechanisms observed in other magnetically-aligned materials[257–262].

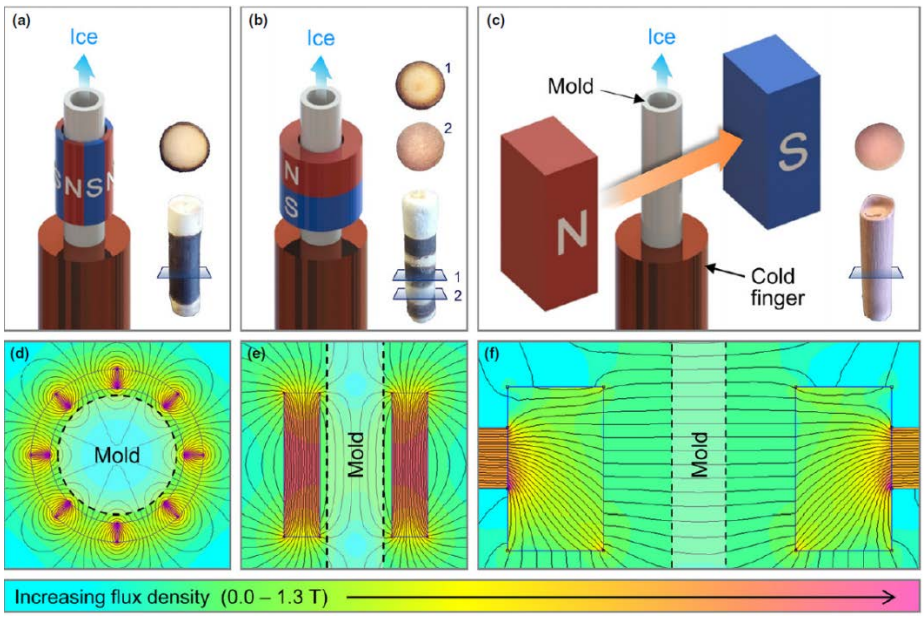

Figure 5.1 Magnetic poles are configured in a way that produce **(a)** radial, **(b)** axial and **(c)** transverse magnetic fields. Image adapted from[244].

Lamellar walls are formed by ceramic particles expelled from the ice front and entrapped between two adjacent ice columns. Mineral bridges are formed by particles engulfed by the ice front and connect adjacent walls to each other (see **Figure 5.3**). In magnetic freeze casting, mixtures of diamagnetic and paramagnetic ceramics with Fe_3O_4 nanoparticles have shown different behaviors under the influence of external magnetic fields[244,249,254]. Paramagnetic materials acquire magnetization parallel to the magnetic field direction while diamagnetic materials acquire magnetization opposite to the magnetic field direction[263]. For TiO_2, a paramagnetic material with a magnetic susceptibility of 5.9×10^{-6} $cm^3.mol^{-1}$ freeze cast under a magnetic field of ~120 mT, lamellar walls were observed to align parallel to the magnetic field and there was a uniform distribution of iron (Fe) in the scaffolds[249]. In contrast, for ZrO_2 a diamagnetic material with a magnetic

susceptibility of -13.8 $cm^3.mol^{-1}$, bridges were observed to align parallel to the field (see **Figure 5.4**)[244].

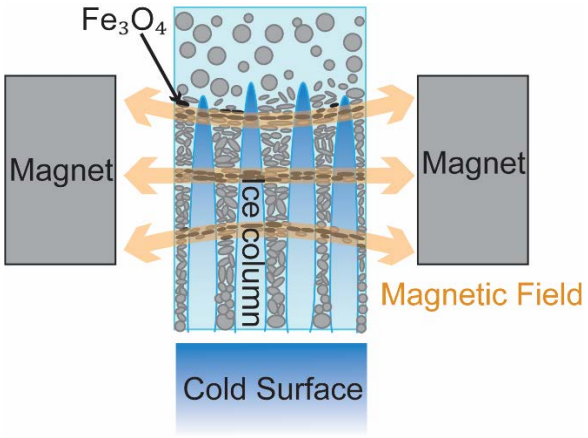

Figure 5.2 Magnetic Freeze Casting. Applying external magnetic fields during solidification will result in alignment of magnetic particles in the direction of the magnetic field.

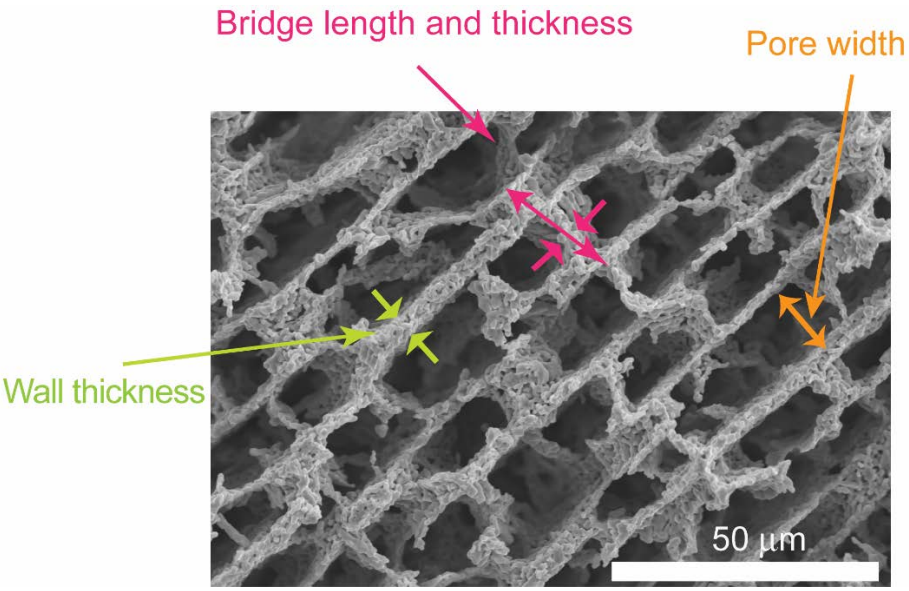

Figure 5.3 Scanning electron micrograph of the cross section of a CeO_2-Fe_3O_4 scaffold. Lamellar walls are formed by ceramic particles trapped between adjacent pores, formed by the ice columns. Mineral bridges are particles entrapped by ice front and connect two or more lamellar walls to each other.

These patterns consisted of iron-rich and iron-poor regions, respectively concentrated at the poles and centers of the scaffolds. In both cases, alignment of the lamellar walls or mineral bridges resulted in enhanced compressive strengths in the transverse direction, parallel to the magnetic field. Interestingly, for TiO_2, although strength in the transverse direction was enhanced, longitudinal strength was decreased (see **Figure 5.5**). Different behaviors observed in paramagnetic TiO_2 (wall alignment) and diamagnetic Al_2O_3, ZrO_2 and HA (bridge alignment) were initially believed to be due to their different magnetic susceptibilities. To further investigate effect of magnetic susceptibility, two additional paramagnetic materials, CeO_2 and Y_2O_3 with magnetic susceptibilities of $+26.0x10^{-6}$ and $+44.4x10^{-6}$ $cm^3.mol^{-1}$ were considered. The processing conditions were the same as in previous works[219,244,249].

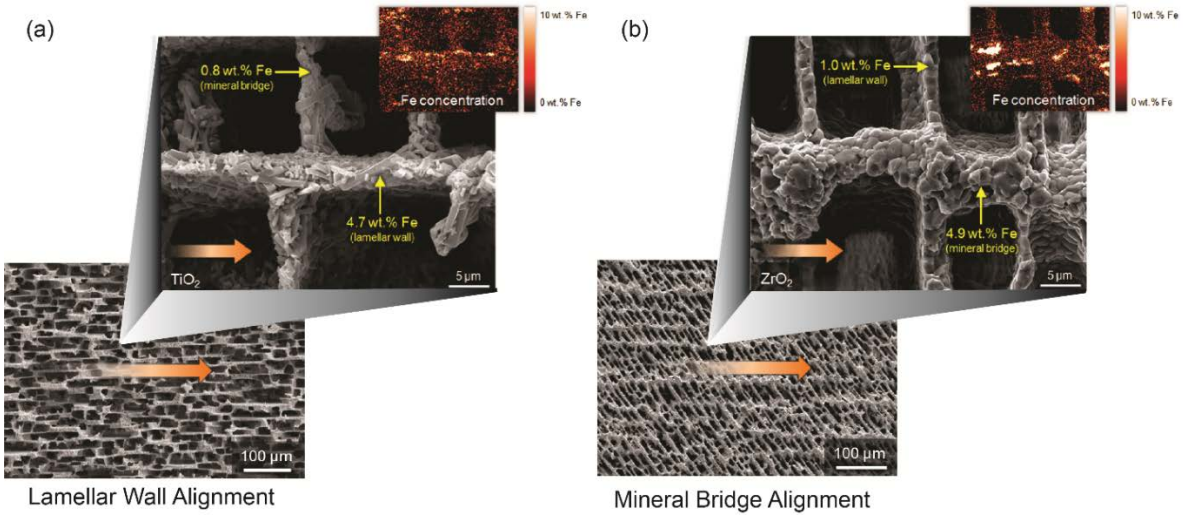

Figure 5.4 Scanning electron micrographs of **(a)** TiO_2-Fe_3O_4 and **(b)** ZrO_2-Fe_3O_4 scaffolds at different magnifications. Elemental mappings (top, right) show the Fe concentrations in the walls/bridges. The orange arrow indicates the magnetic field direction. For TiO_2, lamellar walls are aligned in magnetic field direction at 120 mT

while for ZrO_2 mineral bridges are aligned in magnetic field direction. Image adapted from[264].

5.1 Experimental Procedure

Ceramic powders of CeO_2 and Y_2O_3 (Sigma Aldrich, St. Louis, MO) used in this study had mean particle sizes of 500 nm (according to the manufacturer). Separate batches of the two powders were suspended in water, similar to previous works [244249254], at fractions of 10 vol.%, and mixed with 3 wt.% Fe_3O_4 nanoparticles (~50 nm particle size), 1 wt.% polyvinyl alcohol (PVA) (Alfa Aesar, Ward Hill, MA), 1 wt.% polyethylene glycol (PEG) (Alfa Aesar, Ward Hill, MA), and 1 wt.% ammonium polymethacrylate anionic dispersant, Darvan® 811 (R. T. Vanderbilt Company, Inc., Norwalk, CT). The slurries were ball milled for 24 hrs in alumina grinding media, then degassed for 10-20 minutes and poured into PVC molds attached to a copper cold surface, which was then subsequently cooled at a rate of 10˚C/min. Two neodymium permanent magnets with residual flux density of 14,800 Gauss (BY0X08BR-N52, K&J Magnetic, Inc., USA) were oriented transversely across the freezing mold to apply the magnetic fields during solidification. After freezing, the scaffolds were lyophilized (Labconco, Kansas City, MO) at -50˚C and 350 Pa for 72 hrs. Finally, the scaffolds were sintered at 1200˚C for CeO_2 and 1250˚C for Y_2O_3 at heating and cooling rates of 2˚C/min. Finite element models of the magnetic field distributions were developed using the FEMM (Finite Element Method Magnetics) software (David Meeker, Waltham, MA). For more details on the experimental setup, please refer to Porter et al. work[249].

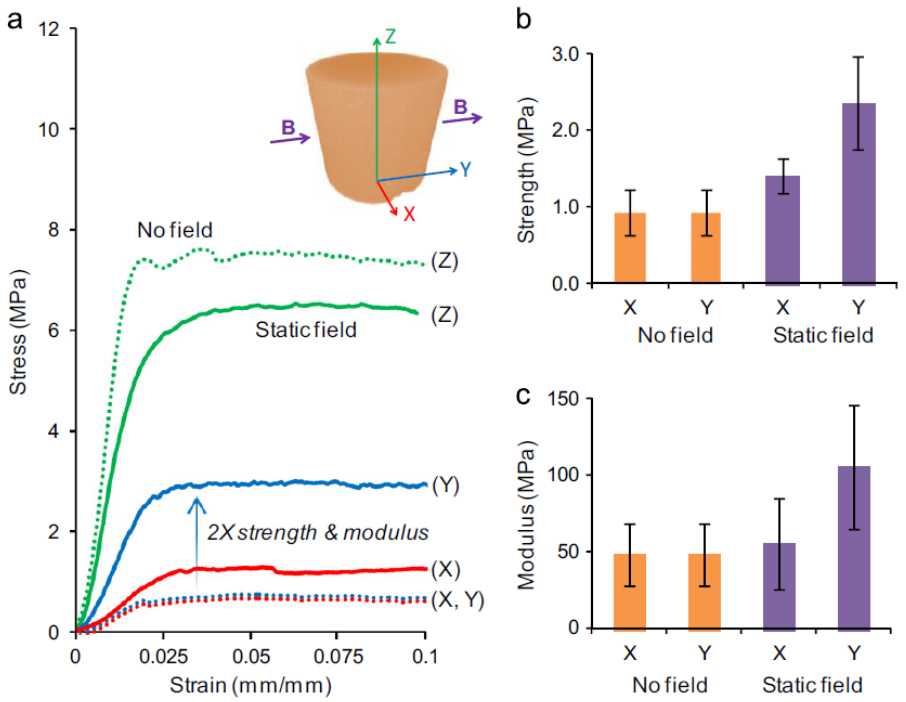

Figure 5.5 Strength and modulus of freeze cast scaffolds. **(a)** Applying external magnetic field increases the strength in transverse direction but longitudinal direction strength drops a little bit. **(b)** Strength and **(c)** modulus of freeze cast scaffolds with and without external magnetic field. Image adapted from[249].

5.2 Material Characterization

A Wolfe® DigiVu™ SMZ 3.0 stereomicroscope equipped with a built-in camera (Carolina Biological Supply Company, Burlington, NC) was used to take the optical images. Scanning electron microscopy (SEM) images were taken at Clemson University's Advanced Materials Research Laboratory (AMRL) on a Hitachi S-3400N SEM microscope (Hitachi, Schaumburg, IL). Samples were sputter-coated with platinum using a Hummer 6.2 sputtering system (Anatech, Hayward, CA). Energy dispersive X-ray spectroscopy (EDS) was performed to determine the distributions of Fe throughout the scaffolds. Measurements of the mineral bridges,

lamellar walls and pore widths (**Figure 5.3**) from SEM images of the scaffolds were taken using ImageJ (NIH, Bethesda, MD).

5.3 Results

5.3.1 Radial and axial magnetic field orientation

ZrO_2-based slurries were freeze cast under radial and axial magnetic fields as shown in **Figure 5.1a & b**. In the radial orientation, the cross-section exhibited a core-shell structure. The shell was denser in the outer region (~%25) where the lamellar walls have a radial orientation following the magnetic field lines, while the core was more porous (~%40) with randomly oriented walls (see **Figure 5.6)**. The thickness of the shell was ~ 750 µm and the core had diameter of ~7.5 mm. In the axial orientation, banded regions were formed consisting of iron-rich and iron-poor regions (see **Figure 5.7**). The dense outer shell (porosity of ~20%) consists of brown regions of a high concentration of iron, while in the center of the cross section is cellular and the inner region lamellar walls have random orientation (see **Figure 5.7 b & c**). In low iron concentration regions the dense outer shell (porosity of ~15%) has a cellular structure while the inner region has random orientation of lamellar walls (see **Figure 5.7e & f**).

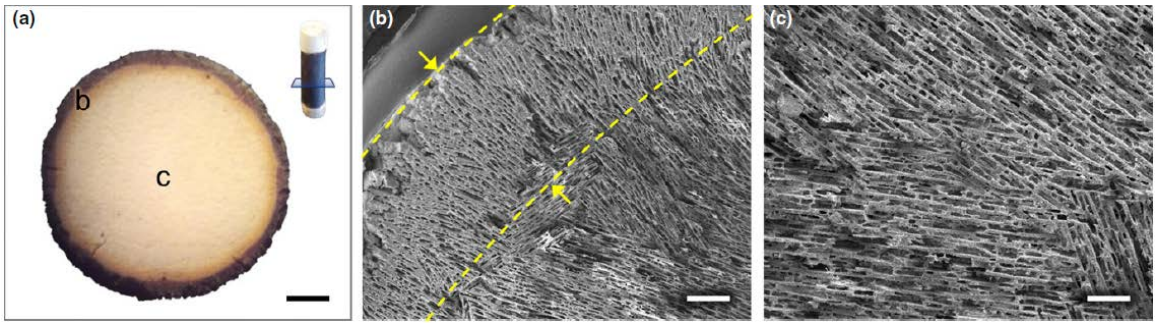

Figure 5.6 **(a)** Radial orientation of magnetic field. Cross section of scaffolds consist of **(b)** outer dense region that have radial orientation of walls while **(c)** inner region has random orientation. Image adapted from[244].

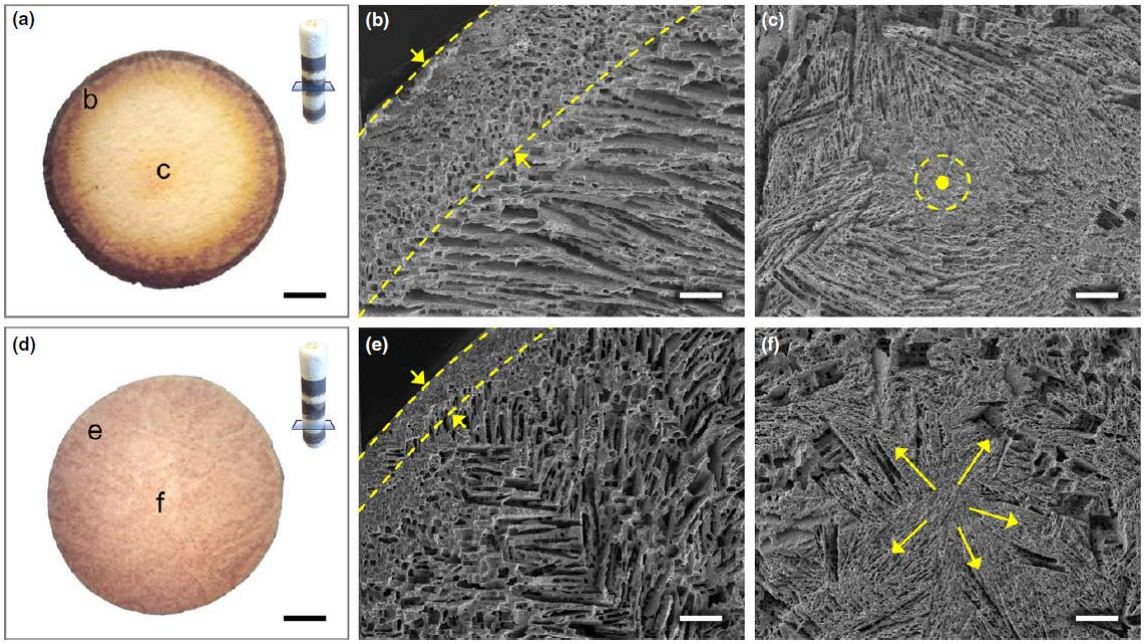

Figure 5.7 Axial orientation of magnetic field. Scaffold show banded regions consisting of **(a)** iron-rich and **(b)** iron-poor regions. In iron rich regions, outer shell **(b)** and center **(c)** have cellular structure while inner region has random orientation of the walls. In iron-poor region outer shell is dense area with cellular structure while inner area has random orientation of the walls. Image adapted from[244].

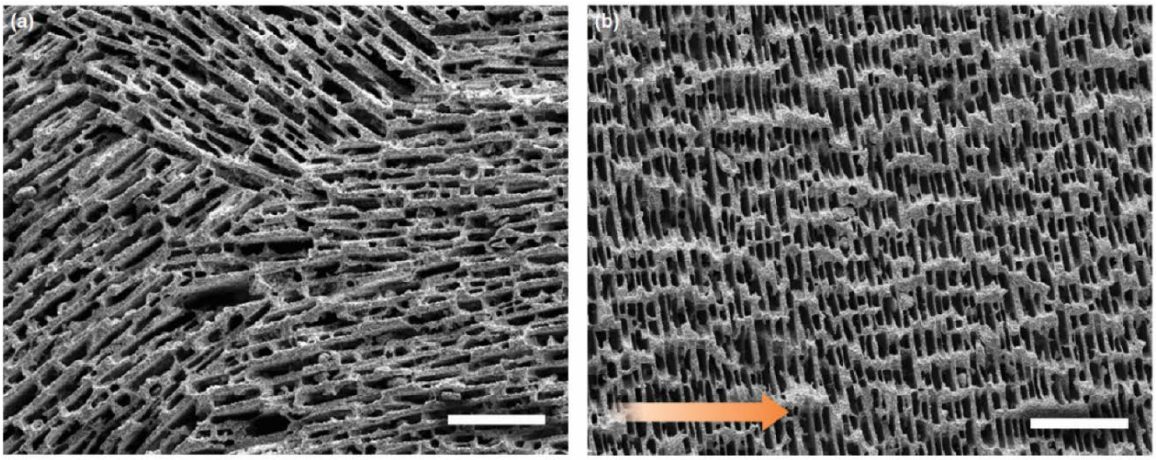

Figure 5.8 Effect of external magnetic field on the microstructure of ZrO_2 scaffolds **(a)** no magnetic field results in random orientation while **(b)** applying transverse magnetic field result in mineral bridge alignment. Image adapted from[244].

5.3.2 Transverse magnetic field orientation

Transverse magnetic fields were applied to the freeze casting of ZrO_2, CeO_2 and Y_2O_3. Applying transverse magnetic fields for ZrO_2 (see **Figure 5.1 c**) caused alignment of mineral bridges in the magnetic field direction (see **Figure 5.8**). The effect of Fe_3O_4 concentration and magnetic field strength was investigated in the ZrO_2 scaffolds. Increasing the Fe_3O_4 concentration increased both the mineral bridge length and thickness (see **Figure 5.9a**). Similarly, increasing the magnetic field strength resulted in longer and thicker bridges. Also, higher Fe_3O_4 concentration and stronger magnetic fields led to more aligned mineral bridges oriented in the magnetic field direction (see **Figure 5.9c&d**). Increased length and thickness of the mineral bridges resulted in enhanced ultimate strength and Young's modulus of scaffolds in transverse direction (see **Figure 5.10**).

Similar to ZrO_2, CeO_2 and Y_2O_3 (both paramagnetic materials) were magnetic freeze cast under transverse magnetic fields. In ZrO_2 scaffolds magnetic field strength was increased up to 90 mT but for CeO_2 and Y_2O_3 scaffolds, the magnetic field strength was increased up to 153 mT. **Figure 5.11** shows schematics of the magnetic field setup. Two locations on the sample cross sections were measured: 'close to the pole' and at the 'center' of the cross section (**Figure 5.11a**). The magnetic field strength along the height of the scaffold (**Figure 5.11a**) and between the magnetic poles (**Figure 5.12b)** were calculated by finite element analysis using the FEMM software. **Figures 5.11c & d** show the variation in magnetic field strength in both the vertical and horizontal directions. Different field strengths were created by setting the poles 4.7 cm, 7.0 cm and 10.0 cm apart from each other. FEMM calculations for the different positions are shown in **Figure 5.11d**.

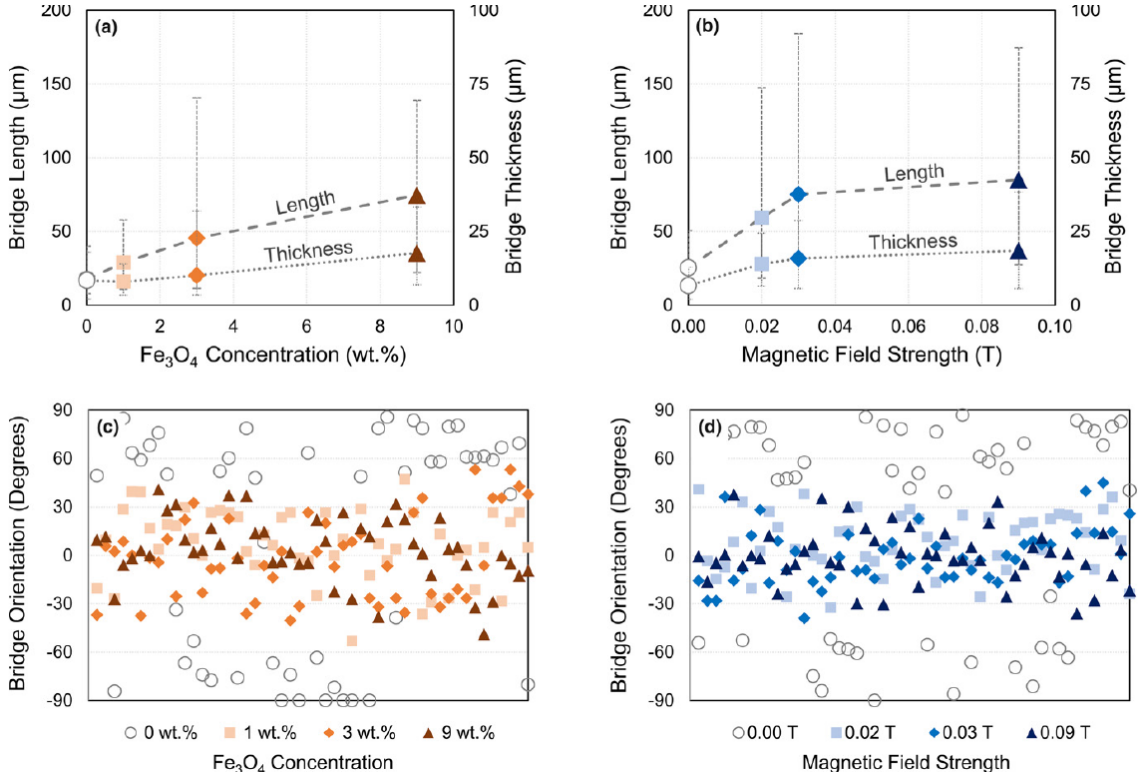

Figure 5.9 Effect of **(a)** Fe_3O_4 concentration and **(b)** magnetic field strength on mineral bridge length and thickness. By increasing **(c)** Fe_3O_4 concentration and **(d)** magnetic field strength mineral bridge were more oriented toward the magnetic field direction.

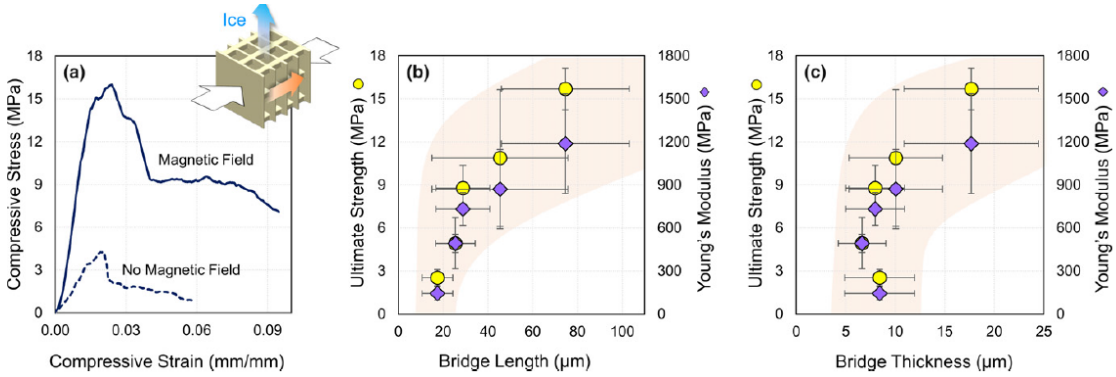

Figure 5.10 **(a)** Stress-strain plot in solidification and magnetic field directions. Direction of applied magnetic field is shown with respect to the solidification direction. Increased **(b)** length and **(c)** thickness of mineral bridges led to enhanced ultimate strength and stiffness of the scaffolds.

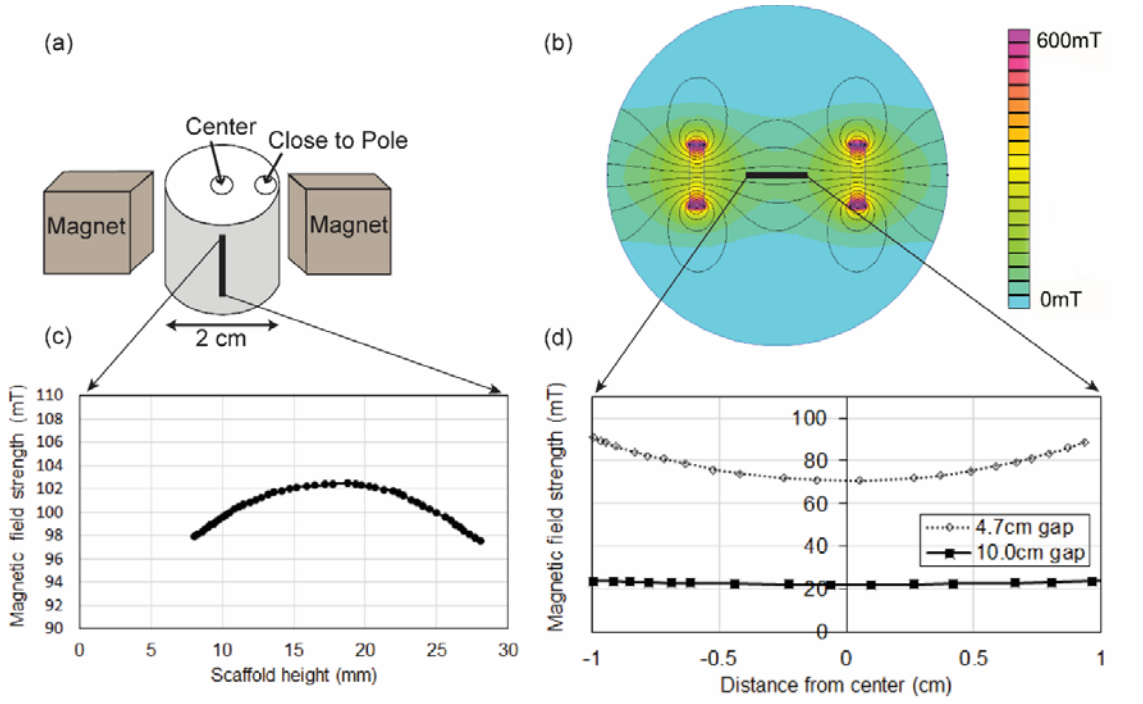

Figure 5. 11**(a)** Two locations where SEM images were taken for measurements of the scaffold cross sections; **(b)** top view, finite element model of the magnetic field applied in the experimental setup; **(c)** plot of the magnetic field strength along the scaffold height, showing that the magnetic field is stronger at the middle of the scaffolds; **(d)** plot of the magnetic field strength at the central region of the experimental setup, showing that the magnetic gradient is stronger for the 4.7 cm gap.

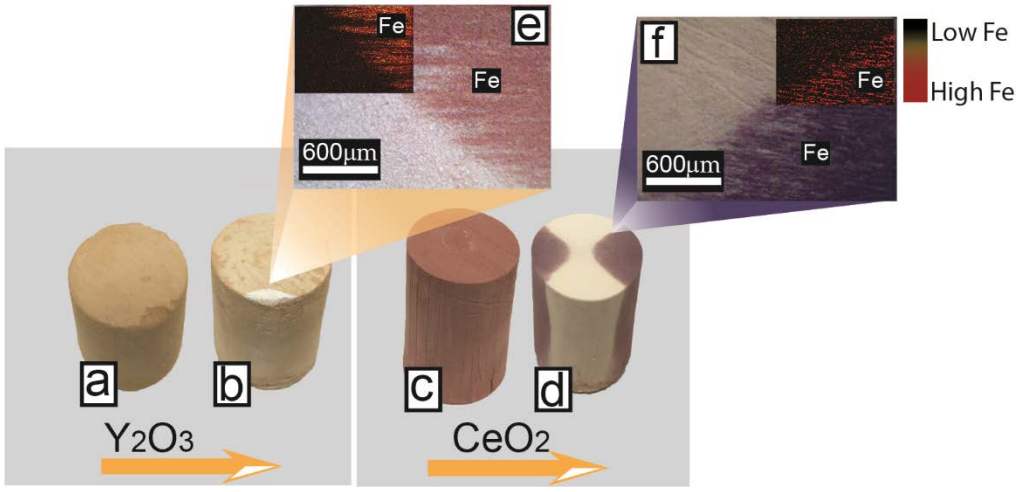

Figure 5.12 Magnetic freeze cast scaffolds of CeO_2 and Y_2O_3 containing 3 wt.% Fe_3O_4. **(a-b)** Y_2O_3 freeze cast under **(a)** 25 mT and **(b)** 42 mT; **(c-d)** CeO_2 under

(c) 25 mT and **(d)** 71 mT. Orange arrows show direction of the magnetic field, and the insets **(e) & (f)** show elemental mappings of Fe_3O_4 at the iron oxide-rich/poor boundary for Y_2O_3 and CeO_2, respectively.

At low magnetic fields (~25 mT), the Fe_3O_4 nanoparticles were nearly uniformly distributed throughout the CeO_2 and Y_2O_3-based scaffolds (**Figure 5.12a & 5.12c**). However, increasing the magnetic field strength (>70 mT) resulted in a segregation of Fe_3O_4 particles, which moved Fe_3O_4 particles toward the magnetic poles, forming iron-rich and iron-poor regions (see **Figure 5.12b & 5.12d**). At the microstructural level, the lengths of the mineral bridges in CeO_2 and Y_2O_3 scaffolds increased up to a field strength of ~120 mT and ~71 mT respectively. Beyond this, the mineral bridges tended to decrease in size (**Figure 5.13a**). Unlike mineral bridge length, their thickness increased with the magnetic field strength and height of the scaffolds (**Figure 5.13b & 5.14b**). For measurements along the height of the CeO_2 scaffolds, as seen in **Figure 5.14a**, there is a decreasing trend of the mineral bridge length versus height of the samples due to the decreasing velocity of the solidification front[192]; faster solidification velocities entrap more particles, forming longer bridges. There is also a jump at the middle of the scaffold that was caused by the stronger magnetic field at a height of ~17 mm. The magnetic field strength along the height of the scaffold was calculated by FEMM software, which shows a maximum magnetic field strength at the middle (see **Figure 5.11c**).

Measurements of wall thickness and pore width of the CeO_2 scaffolds versus the magnetic field strength show that the external magnetic field does not significantly affect the freezing properties as there is no clear trend in these measurements (**Figure 5.15a**). The lamellar wall thickness and pore width,

however, increase with the scaffold height due to a decreasing velocity of the solidification front, as there is an inverse relationship between pore width and solidification velocity (**Figure 5.15b**)[186,260].

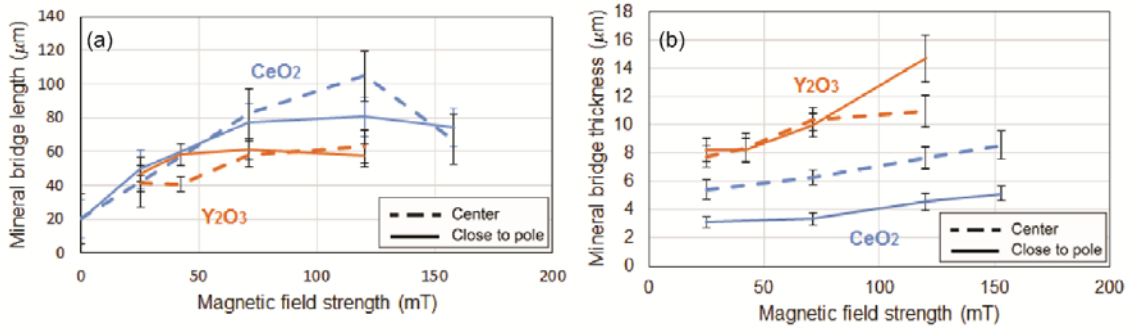

Figure 5.13 **(a)** Mineral bridge length of CeO_2 and Y_2O_3 scaffolds as functions of magnetic field strength for the two different locations on the cross section: 'close to pole' and 'center' (see **Figure 3.11a**). **(b)** Mineral bridge thickness of CeO_2 and Y_2O_3 scaffolds as functions of magnetic field strength for the two different locations on the cross section: 'close to pole' and 'center'. CeO_2 measurements are done at 10 mm height from the bottom of the scaffold (of 25 mm length scaffolds) and Y_2O_3 measurements are done at 18mm height for both graphs. Error bars show confidence intervals for 95% probability.

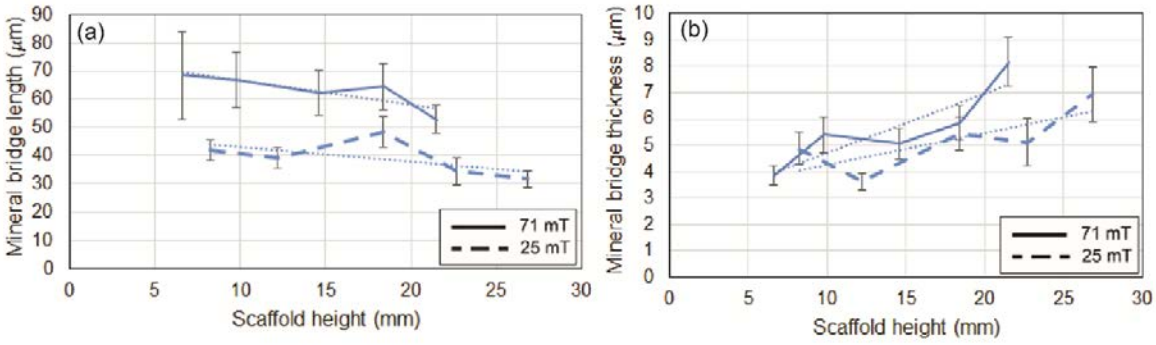

Figure 5.14 **(a)** Mineral bridge lengths of CeO_2 scaffolds are measured as a function of height for the 25mT and 71mT fields. **(b)** Mineral bridge thicknesses of CeO_2 scaffolds are measured as a function of height for the 25mT and 71mT fields. Measurements are from the 'center' location. Error bars show confidence intervals for 95% probability.

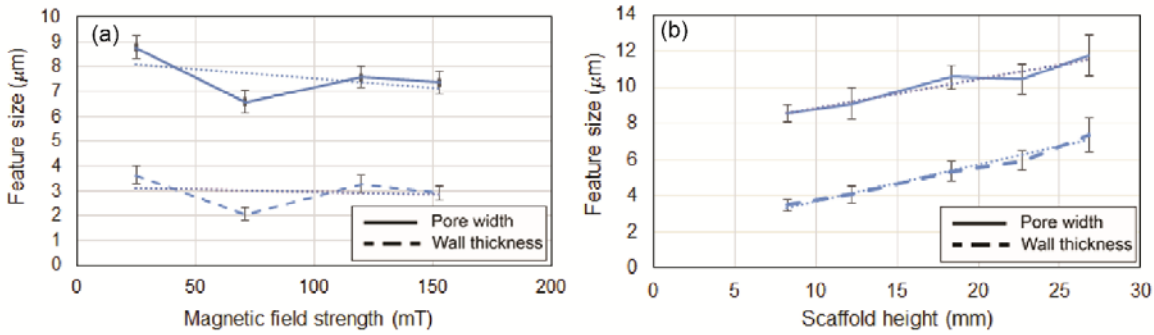

Figure 5.15 Lamellar wall thickness and pore width of CeO_2 scaffolds measured as a function of **(a)** different magnetic field strengths, measurements are done at 10 mm height from the bottom of the scaffold, and **(b)** scaffold height at the 'close to pole' location. Error bars show confidence intervals for 95% probability.

5.4 Magnetic Manipulation

In electromagnetism, $\boldsymbol{B}$ is the magnetic field and $\boldsymbol{H}$ comes from the definition in Ampere law which is defined as[263,265]:

$$\boldsymbol{H} = \frac{1}{\mu_0}\boldsymbol{B} - \boldsymbol{M} \tag{5.1}$$

where $\mu_0 = 4\pi \times 10^{-7} N/A^2$ is the permeability of free space, $\boldsymbol{B}$ is magnetic field and $\boldsymbol{M}$ is magnetization. $\boldsymbol{B}$ and $\boldsymbol{H}$ are often mistaken, as $\boldsymbol{H}$ can be measured easily in the laboratory; to make an electromagnet a current is run through a coil and by knowing current, $\boldsymbol{H}$ can be calculated. On the other hand, to obtain $\boldsymbol{B}$**,** the type of material used in the electromagnet, whether or not iron is present, and the history of the magnetization must be known[263]. When a material is placed in an external magnetic field, a magnetic field is induced in the material with magnitude shown by the magnetization, $\boldsymbol{M}$. Magnetization is defined as magnetic dipole moments

per unit volume. Torque exerted on a current-carrying wire loop in a magnetic field is given by[263]:

$$\boldsymbol{N} = \boldsymbol{m} \times \boldsymbol{B} \tag{5.2}$$

where $\boldsymbol{m} = I \times A$, is called the magnetic dipole moment, *I* is the current and *A* is the surface enclosed by the loop. By analogy, torque exerted from an electric field on an electric dipole ($\boldsymbol{N} = \boldsymbol{P} \times \boldsymbol{E}$, $\boldsymbol{N}$, $\boldsymbol{P}$ and $\boldsymbol{E}$ are electric torque, dipole and field). Magnets, current-carrying loops, or molecules all are example of magnetic dipoles [263]. The relationship between $\boldsymbol{M}$ and $\boldsymbol{H}$ is given by:

$$\boldsymbol{M} = \chi_m \boldsymbol{H} \tag{5.3}$$

where χ_m is the magnetic susceptibility of a material. Diamagnetic materials have negative magnetic susceptibility while paramagnetic materials have positive[266]. When paramagnetic materials are placed in a magnetic field they acquire magnetization parallel to the external field and strengthen the field, while diamagnetic materials acquire magnetization opposite to the field and weaken the field. For diamagnetic and paramagnetic materials ***H*** and ***B*** are related as:

$$\boldsymbol{B} = \mu_m \boldsymbol{H} \tag{5.4}$$

where μ_m is magnetic permeability.

5.5 Uniform magnetic field versus gradient magnetic field

If a magnetic particle is placed in a uniform magnetic field within a non-magnetic medium, a magnetic torque is exerted on, which aligns the particle in the direction

of the field. This torque is given by equation (5.2) which equations 5.3 & 5.4 can be written as[267]:

$$N = \mu_m V \boldsymbol{M} \times \boldsymbol{H}, \tag{5.5}$$

where *V* is the volume of the particle. Also note that $\boldsymbol{m}$ = V$\boldsymbol{M}$. Torque, given by equation 5.5, for isotropic paramagnetic particle is zero, but when there is geometric anisotropy it is non-zero[267]. If the particle is placed in a gradient (non-uniform) magnetic field, it experiences a magnetic force as well. This force in the horizontal direction is given by[268,269]:

$$F_M = V_p \left(\frac{1}{\mu_0}\right)(\chi_p - \chi_l)\boldsymbol{B}\frac{\mathrm{d}\mathbf{B}}{\mathrm{dx}} \tag{5.6}$$

where V_P is the volume of a particle, μ_0 is the vacuum permeability, **B** is the magnetic field strength, $\frac{\mathrm{d}\mathbf{B}}{\mathrm{dx}}$ is the magnetic field gradient in x direction, χ_p is the magnetic susceptibility of the particle, and χ_l is the magnetic susceptibility of medium.

5.6 Magnetic particles in non-magnetic suspensions under uniform and gradient magnetic fields

When a mixture of magnetic and non-magnetic particles are placed in a static magnetic field, a magnetic torque, given by equation (5.5), aligns magnetic particles in the magnetic field direction[226,229]. Magnetic torque must compete with Brownian motion and gravitational torque (for particles with anisotropic geometry) to align the particles in the field direction[273]. Brownian motion randomizes alignment of the particles while gravitational torque aligns the long axis of particles

to the horizontal position. Brownian force is dominant for small particle sizes[274] while gravitational torque is dominant for larger particles. Hence, only particles in a very specific size range are aligned in the field direction by the magnetic torque. When an oscillating magnetic field is applied on a particle with anisotropic geometry (e.g., a platelet), low frequencies of rotation cause platelets to follow the magnetic field, but increasing rotation frequencies, cause viscous forces to dominate and platelets align parallel to the plane of rotation[275]. Drag, buoyancy, inertia, and interparticle forces are also exerted on the magnetite particles[274]. Buoyant and inertial forces are usually neglected as they are small. Peng et al. neglected Brownian and dynamic related forces and focused on the simulation of static equilibrium[224]. In uniform magnetic fields, no force is exerted on the magnetite particles from the field, but induced magnetization in magnetite alters the magnetic field in the vicinity of magnetite particles[278,279]. These local gradients around magnetite cause attraction of magnetite particles to each other and form chain-like clusters[270–272,277,280–283] (see **Figure 5.16**) similar to patterns formed in ferrofluids[284–288]. Two-dimensional Monte Carlo simulations have shown that increasing magnetic field strength, magnetite particle size, and concentration of magnetite all result in longer clusters, while increasing concentration of non-magnetic particles reduces cluster length[277]. Alignment of magnetic particles may lead to alignment of non-magnetic particles in the field direction depending on particle size and shape of both magnetic and non-magnetic particles[289].

When a mixture of magnetic and non-magnetic particles is placed in gradient magnetic field, in addition to magnetic torque, a magnetic force is also

exerted on the particles. In another study, Peng et al.[276] considered a distribution of magnetite particles in the gradient field. They also considered forces from interaction between magnetite particles and repulsive forces due to overlapping steric layers. By increasing the magnetic field gradient, magnetite particles migrate toward higher fields, and a gradient composition is formed (see **Figure 5.12b&d**)[276,290]. Increasing the size of magnetite forms chain-like clusters and hinder translation of magnetite particles toward the higher fields[276], similar to the effect of increasing concentration of non-magnetic particles which hinder translation of magnetite particles too[276]. Usually when interparticle interactions between magnetite particles are stronger than the interaction of magnetite with a field, magnetite particles do not align with the field direction [291–294] and other patterns are formed [295–297].

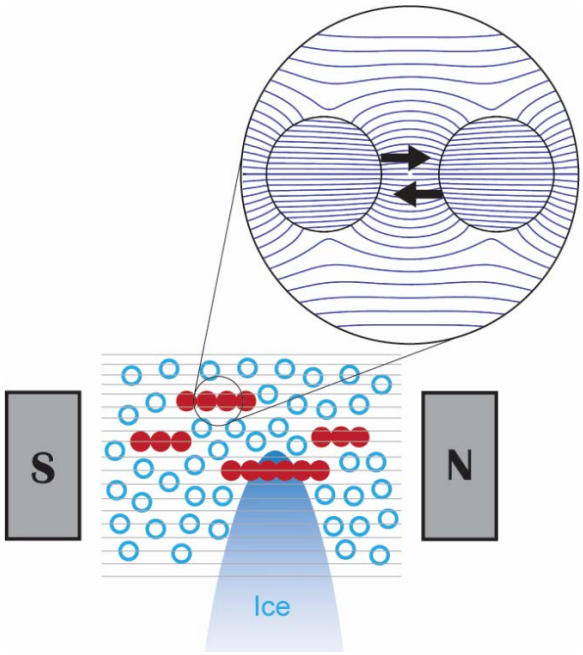

Figure 5.16 External magnetic field induce magnetization in Fe_3O_4 particles and this induced field will create local gradient around the Fe_3O_4 particles. Local

gradient cause Fe_3O_4 particles exert force on each other and form chain0like structures. These clusters will be easily entrapped by ice columns and form mineral bridges. Red particles are Fe_3O_4 and blue ones are ceramic particles. Image partially adapted from[278].

5.7 Magnetite and paramagnetic particle interaction

Magnetite has been used as a separating tool in the mineral processing industry to separate paramagnetic particles from mineral ores. In this process, magnetite is embedded in a porous matrix and a slurry containing paramagnetic particles flows through the matrix. Paramagnetic particles move in the direction of the increasing gradient field and are attracted to the magnetite[298]. Ebner et al.[266,298,299] theoretically analyzed adsorption of paramagnetic particles by magnetite. Forces between magnetite and paramagnetic particles are magnetic, electrostatic, van der Waals, viscous and Brownian forces[266,295]. When magnetite and a paramagnetic particle is placed in a magnetic field, magnetization in magnetite and paramagnetic particles alter the magnetic field in the vicinity of the particle and magnetite. The magnetic force between magnetite and paramagnetic particle is given by [266,299]:

$$F_{mp} = \frac{V_p}{2}\mu_0(\chi_p - \chi_m)\nabla\mathbf{H^2} \tag{5.7}$$

where V_P is the volume of the particle, μ_0 is the vacuum permeability, and χ_p and χ_m are the magnetic susceptibilities of the particle and magnetite respectively. The magnetic field experienced by paramagnetic particles is the sum of the external magnetic field and the magnetic field created by magnetization of magnetite. The components of $\mathbf{H}$ in spherical coordinates are given by[266,299]:

$$H_r = (H_a + \frac{2{R_m}^3}{3r^3}M_{s,m})\cos\theta \tag{5.8a}$$

$$H_\theta = (-H_a + \frac{2{R_m}^3}{3r^3} M_{s,m}) \sin\theta \quad (5.8b)$$

where $M_{s,m}$ is the saturation magnetization of the magnetite ($M_{s,m} = 4.8 \times 10^5\ Am^{-1}$), H_a is the magnitude of the applied magnetic field, R_m is the diameter of the magnetite, and r is the distance between the magnetite and paramagnetic particle. If the paramagnetic particle approaches the magnetite with angles 0°-60° and 120°-180°, the force is attractive; otherwise, the force is repulsive[266]. This is similar to magnetite-magnetite interactions under a magnetic field[295]. Van der Waals forces are short range and depend considerably on the size of particles, but they can be neglected at distances greater than 30 nm. Both magnetite and paramagnetic particles contain acidic and basic groups, which form charged surfaces when they are submerged in liquids with a high dielectric constant like water[300]. This causes a repulsive electrostatic force between the magnetite and paramagnetic particles whose magnitude depends on the concentration of background electrolytes[299,301]. The sum of all these forces is compared with the Brownian force and represented by the dimensionless Peclet number, Pe [266,299]. If Pe<-10, then the paramagnetic particle is attracted to magnetite; otherwise retention would not happen. Ebner et al.[266] investigated the effect of five parameters in retention of paramagnetic particle by magnetite. Parameters were paramagnetic particle size, magnetite particle size, magnetic field strength, magnetic susceptibility of paramagnetic particle and electrolyte concentration. Among these, paramagnetic particle size had the greatest effect. For example, by increasing particle size two times, net force increased ten times. They also concluded that particles with diameters less than 80 nm are not absorbed since

the magnetic force is too small to overcome Brownian motion. The magnetic susceptibility of paramagnetic particles have a direct linear relationship -- increasing magnetic susceptibility two times leads to a two fold increase in net force[299]. Magnetite particle size, however, has negligible effect on net force, as smaller magnetite particles have larger curvature, creating a larger field gradients around their surface. Magnetic field strength has a dramatic effect on adsorption, but its effect diminishes quickly by reducing the particle size. For example, particles with a diameter smaller than 40 nm are not adsorbed at any magnetic field strength[266]. Finally, increasing electrolyte concentration is favorable for retention of paramagnetic particles[299]. Ebner et al.[301,302] expanded their work by considering the interaction of a paramagnetic particle with an array of magnetite particles rather than a single one. Similar to single particle interaction, there were regions in which the interaction was repulsive and others where the interaction was attractive. Also, when the spacing between magnetite particles becomes larger than two magnetite particle diameters, the paramagnetic particles basically interact with just one magnetite particle in the array and the effect of neighboring magnetite particles is negligible.

5.8 Paramagnetic and diamagnetic ceramics in magnetic freeze casting

Six different ceramic materials were used in magnetic freeze casting (MFC); Al_2O_3, ZrO_2, Hydroxyapatite (HA), CeO_2, TiO_2 and Y_2O_3. Al_2O_3, ZrO_2 and HA are diamagnetic material while CeO_2, TiO_2 and Y_2O_3 are paramagnetic materials. The magnetic susceptibility and particle size of these materials are listed in **Table 5.1**.

In MFC, a mixture of these particles with magnetite (~50nm) was freeze cast under stationary and rotating magnetic fields to align the microstructures in desired directions[242] . Diamagnetic materials are repelled from higher field gradients to lower field gradients, which causes repulsive interaction between them and magnetite, as magnetite creates a local gradient in its vicinity[279,298]. Under low magnetic fields, Fe_3O_4 particles have almost uniform distribution within the scaffolds, but by increasing magnetic field strength, magnetite particles chain up with each other and form clusters. These clusters are easily entrapped by the advancing ice front and form bridges connecting walls to each other[117]. By increasing the magnetic field strength, the length of the mineral bridges increases and reaches a maximum. Beyond that point, the length of the bridges decrease. Bridge thickness increases monotonically by field strength, similar to ferrofluid behavior[293].

The magnetic setup used in MFC consisted of two magnets placed across the mold[249]. In this configuration increasing the magnetic field strength increased the gradient. Stronger gradients exerted magnetic forces on magnetite particles and attract them toward the poles, forming biphasic regions. Also, this force attracted magnetite particles toward pole and caused a drop in mineral bridge length beyond specific magnetic field strength.

Paramagnetic particles are attracted to magnetite under magnetic fields provided they overcome Brownian and electrostatic forces. For CeO_2 and Y_2O_3 of small particle size, the magnetic force cannot overcome Brownian motion and no significant interaction between these and magnetite particles is observed. Hence,

similar to diamagnetic particles, magnetite particles chain up and form clusters. For TiO_2 of larger particle size (see **Table 5.1**), the magnetic force overcomes Brownian and electrostatic force, and TiO_2 particles are adsorbed by magnetite[249]. Therefore, the alignment of magnetite particles in the magnetic field direction align non-magnetic ceramic particles as well. At 120 mT, it was observed that lamellar walls aligned in the magnetic field direction[249]. Increasing the magnetic field strength further increases the gradient as well, which applies stronger forces on the magnetite particles and attracts them toward the poles, whereas wall alignment in TiO_2 does not occur at higher fields.

Table 5.1 Particle size, density and magnetic susceptibility of different ceramic particles investigated. Particle sizes are obtained from SEM measurements and manufacturer information.

	Magnetic Category	**Density** ($g\ m^{-3}$)	**Particle size** (nm)	**Magnetic susceptibility** ($10^{-6}\ cm^3\ mol^{-1}$)
TiO_2	Paramagnetic	4.26	139*	5.9 [264]
CeO_2	Paramagnetic	7.22	46*	26.0 [305]
Y_2O_3	Paramagnetic	5.01	70*	44.4 [305]
Al_2O_3	Diamagnetic	4.00	200~350[$]	-37.0 [255]
HA	Diamagnetic	3.15	1000~3000[$]	-81.5 [305,306]
ZrO_2	Diamagnetic	5.89	200~500[$]	-13.8 [264]

(*grain size measured from SEM images)

([$]data are from manufacturer)

To ensure adsorption of magnetite onto ceramic particles, Frank et al.[255,307] used superparamagnetic magnetite (~10nm) particles to surface magnetize Al_2O_3

particles. Three different particle sizes were used; 195nm, 225nm and 350nm. For 195nm, no alignment of walls was observed. For 225nm at 150 mT, some regions were aligned in the magnetic field direction, and for 350nm at 75 mT, more regions were aligned in the magnetic field direction[304,307]. A summary of studies in magnetic freeze casting using different materials and different additives are displayed in **Table 5.2**.

Table 5.2 Magnetic freeze casting studies considering aqueous slurry with different additives and particles with different susceptibility

					Magnetic field			
Study	**Solvent**	**Particle**	**Additive**	**Freezing rate/direction**	**Strength/ Orientation**	**Susceptibility/Magnetization**	**Composition**	**Outcome**
Porter, MSEA 2012	Water	HA, ZrO_2, Al_2O_3, TiO_2	Binder, dispersant	10 °C/min, longitudinal	0.12 T, Transverse & rotatory	Susceptibility -81.5×10^{-6}, -13.8×10^{-6}, -37×10^{-6}, 5.9×10^{-6} (cm^3/mol)	Mixture of Fe_3O_4 & ceramics	In TiO_2 scaffolds iron had uniform distribution while for others iron-rich and iron-poor regions were formed. Also, in TiO_2 walls were aligned in the magnetic field direction and no alignment was observed for others.
Porter, CS, 2015	Water	ZrO_2	Binder, dispersant	10 °C/min, longitudinal	0.12 T, Rotatory	Susceptibility -13.8×10^{-6} (cm^3/mol)	Mixture of Fe_3O_4 & ZrO_2	Rotating magnetic field created helix-reinforced ZrO_2-epoxy composite with enhanced torsional properties.
Porter, JACS, 2016	Water	ZrO_2	Binder, dispersant	10 °C/min, longitudinal	0~0.5 T, Transverse	Susceptibility -13.8×10^{-6} (cm^3/mol)	Mixture of Fe_3O_4 & ZrO_2	Axial, radial and transverse magnetic fields, created biphasic regions in the scaffolds. Length of bridges increased by increased magnetic field strength. Bridge formation contributed to enhanced strength in transverse direction.
Niksiar, JMRT, 2018	Water	CeO_2, Y_2O_3	Binder, dispersant	10 °C/min, longitudinal	0~0.158 T, Transverse	Susceptibility 26×10^{-6}, 44.4×10^{-6} (cm^3/mol)	Mixture of Fe_3O_4 & CeO_2, Y_2O_3	Bridges were aligned in the magnetic field direction and no wall alignment was observed. Increased gradient in magnetic field created biphasic regions.
Frank, JMBBM, 2017	Water	Al_2O_3	Binder, dispersant	10 °C/min, longitudinal	0.025~0.15 T Transverse	Magnetization $0.6\sim2\times10^{-14}$ (emu)	Surface magnetized Al_2O_3	Best alignment of walls in transverse direction was observed for 350 nm particle (out of 195, 225, 350 nm) at 75 mT. Strength in transverse direction was enhanced due to alignment of the walls in transverse direction.

Frank, MSEC, 2017	Water	Al_2O_3	Binder, dispersant	10 °C/min, longitudinal	0.075 T Transverse	Magnetization 1.97×10^{-14} & 454×10^{-14} emu (particle, platelet)	Surface magnetized Al_2O_3	By using big 5 µm Al_2O_3 platelets, walls were aligned in the magnetic field direction at 75 mT. Best mechanical properties was obtained when 7:1 ratio of particles (~350 nm) to platelets (5 µm) were used.

CHAPTER 6

3D-PRINTED SCAFFOLDS MIMICKING MAGNETIC FREEZE CASTING PATTERNS

In materials processing, changing the processing conditions will alter microstructure, which affects the mechanical properties of the materials. Relationships between the microstructure and mechanical properties of scaffolds made by freeze casting is investigated in several studies[219,244,308,309]. In freeze casting, processing conditions that affect the microstructural architecture are: freezing velocity, initial concentration of the ceramics, particle size, particle thermal conductivity, particle free energy in contact by the liquid, freezing liquid viscosity, freezing liquid latent heat, freezing liquid free energy in contact with a particle, and finally the concentration of additives (e.g. binder, dispersant, etc.). Scaffolds made by magnetic freeze casting have two main microstructural characteristics: lamellar walls and bridges. The thickness and orientation of lamellar walls, length, thickness

and orientation of transverse bridges (see **Figure 5.3**) and number of domains in a cross section (see **Figure 6.1)** are parameters that most affect the mechanical properties of freeze cast scaffolds. In freeze casting, changing one of the processing conditions usually changes multiple microstructural characteristics at the same time. For example, increasing the freezing velocity will decrease the lamellar wall thickness and spacing, but also increase the number of domains through the cross section. Therefore, finding relationships between microstructure and mechanical properties is challenging because keeping all microstructural characteristics constant, while varying a single feature is impossible.

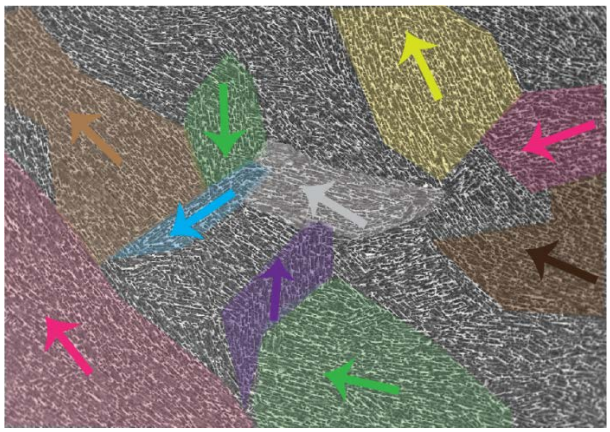

Figure 6.1 Cross sectional view of CeO_2 scaffold fabricated by magnetic freeze casting.

Recently, by the advent of additive manufacturing, a powerful tool for design has been introduced. 3D printing is becoming popular in almost every field and it has recently been used to fabricate porous materials[25–27,310]. By taking advantage of 3D printing, scaffolds are designed in a way that one microstructural parameter is changed at a time, while keeping all other parameters constant. In this chapter, we investigate the relationship between microstructure and mechanical properties.

As it was discussed in chapter 5, applying an external magnetic field during the solidification of TiO_2, lamellar walls were aligned in the transverse direction. This led to an enhanced strength and stiffness of scaffolds in the transverse direction, while strength in the longitudinal direction was decreased. Here, we investigate this behavior by 3D printing, which enables us to change one parameter at a time. This let us understand the effects of each microstructural characteristic individually.

6.1 3D printing process

Scaffolds mimicking magnetic freeze casting patterns were designed in Solidworks software (see **Figure 6.2a**) and were exported as STL files to Formlab's PreForm software (see **Figure 6.2b**) and sent to the Form2 printer (Formlabs, Somerville, MA) (see **Figure 6.2c**). For printing, supports (see **Figure 6.2d**) are used to make sure parts attach to the build platform during the print. Also, using supports helps reduce damage in the printed parts when removing them from the platform. After 3D printing, the scaffolds were washed with Isopropyl alcohol 90% for 1 minute to remove residual resins from the surface of the prints. In SLA (stereolithography) 3D printers, resin is cured with a laser during printing. However, some of the polymers remain uncured after printing. Therefore, to make sure all polymers are fully cured, the parts are post cured with 405 nm lights for 1 hour, which promotes further polymer crosslinking. This strengthens the print and increases their stiffness and temperature resistance. A final scaffold after post curing is shown in **Figure 6.2e**.

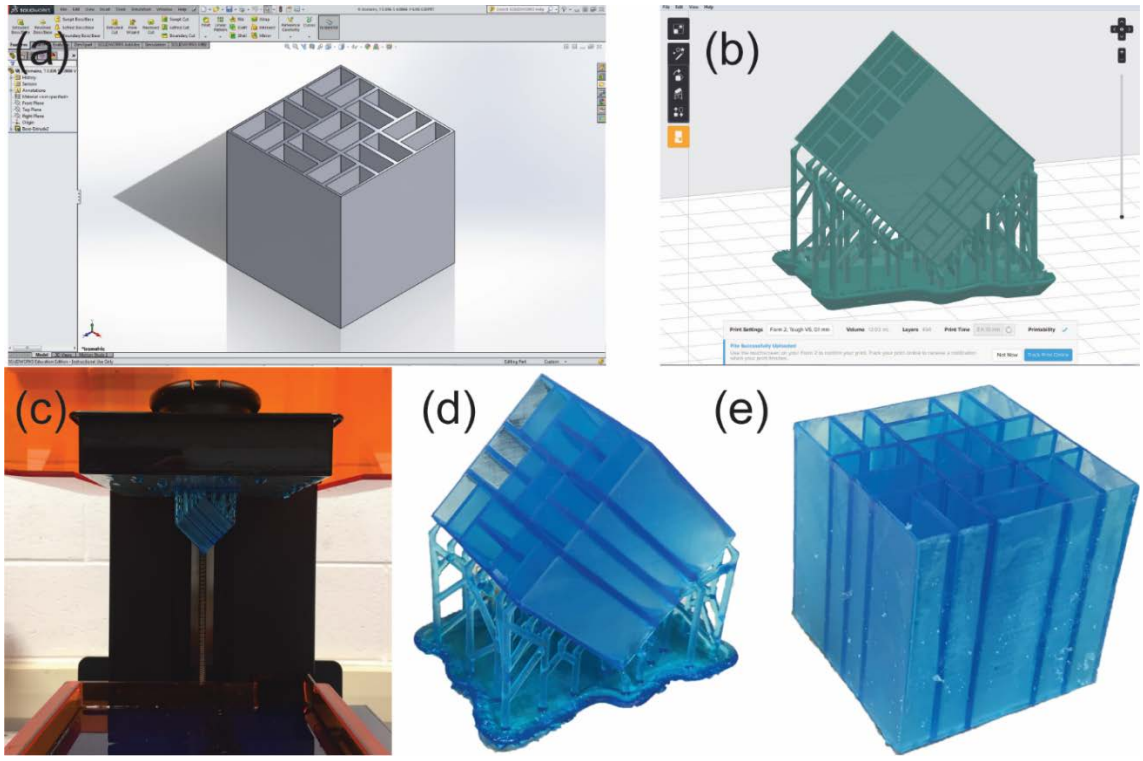

Figure 6.2 3D printed scaffolds. **(a)** Scaffolds are designed in Solidworks; **(b)** Models are uploaded in PreForm software **(c)** 3D printed in Form2 printer **(d)** Finished scaffold with supports, model is 3D printed with 45º to avoid warping **(e)** Final scaffold after removing the supports

6.1.1 Issues arising during 3D printing

When printing parts, the surfaces that are attached to supports are not flat, but slightly bumpy (see **Figure 6.3a**). Another issue was warping of the walls after the printing and post-cure processes (see **Figure 6.3b**). This happens when there are thin (<0.5 mm) walls. To avoid surface bumps and warping, the parts were oriented at 45º with respect to the platform; time washing with IPA was minimized, and they were left in a dark place until completely dried. Another useful practice to reduce the warping is regular rotation of the parts during post curing.

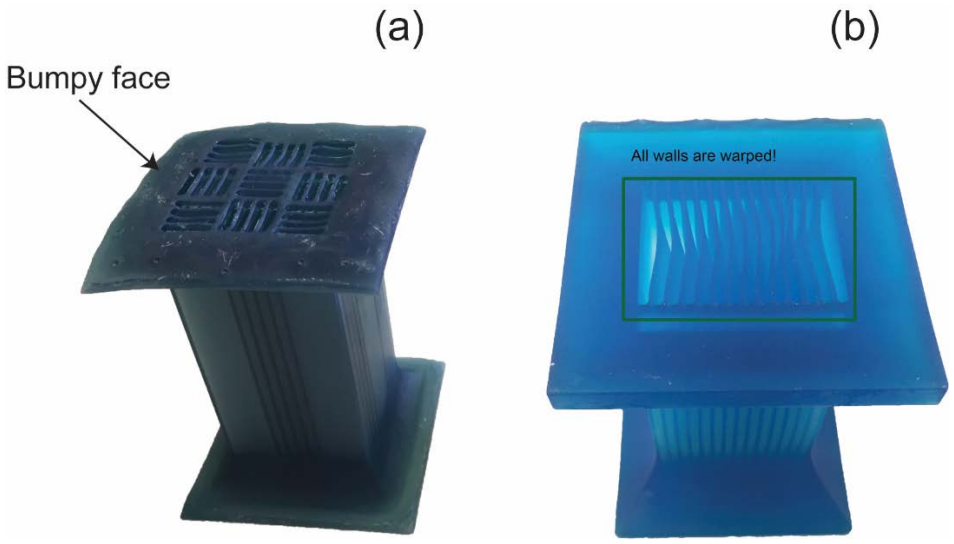

Figure 6.3 **(a)** Surfaces connected to the supports are printed bumpy and not totally flat; **(b)** For 3D printed parts, when wall are thin and large, warping happens

The mechanical properties of scaffolds made by 3D printing are functions of the processing parameters. These parameters include the type of resin used, washing time in IPA, post-curing duration, and quality of the resin tank. According to observations, longer wash time reduces the strength of the scaffolds, while longer cure-time increases strength. Scaffolds printed on brand new resin tanks had higher strength than those printed with old and opaque resin tanks. To minimize variance and uncertainty in our experiments, four scaffolds belonging to a single category (three different categories were tested: wall thickness, number of domains, and bridge thickness) were printed together. Then, parts were washed for one minute in IPA and left in a dark room to dry for one hour. After drying, they were cured for one hour. As ambient light affects the strength of the scaffolds, compression tests were run 15 minutes after post-curing.

6.2 Compression testing

To make sure results obtained are not material specific, four different commercially-available resins were investigated: Tough, Durable, High Temperature and Rigid resins. High Temperature resin had a brittle response, while durable, rigid, and tough resins had more ductile responses (see **Figure 6.4**). Furthermore, to ensure experimental repeatability, each design was printed and tested three times. A Shimadzu AGS-X tensile testing machine (Nishinokyo-Kuwabara-cho, Japan) was used for the compression testing. The displacement rate was 1cm/min and a 50 kN load cell recorded the applied force. A limit for the displacement was set to 20 mm. For break detection, the instrument sensitivity was set to 90%, and the break detection start point was 0.035%. Scaffolds had outer cross sectional dimensions of 30 mm × 30 mm and heights of 30 mm, compliant by ASTM E9-09 standard. Furthermore, in this study we tested scaffolds in two other directions: X and Y (see **Figure 7.3)** and compared the performance of the scaffolds based on their properties in X, Y and Z directions. Stress is found by dividing force by the cross-sectional area (30 mm X 30 mm).

In this chapter we investigate the reason of strength enhancement for scaffolds made at higher solidification velocities by designing scaffolds in which one parameter is changed while the others are kept constant. At higher solidification velocities three patterns are observed. First, thickness and spacing of the lamellar walls were decreased which led to a finer structure. Second, the number of domains at the cross section was increased and finally, density of bridges connecting adjacent walls to each other was increased since at higher

velocities more particles are entrapped by the solidification front. Now we are going to investigate the effect of each parameter individually.

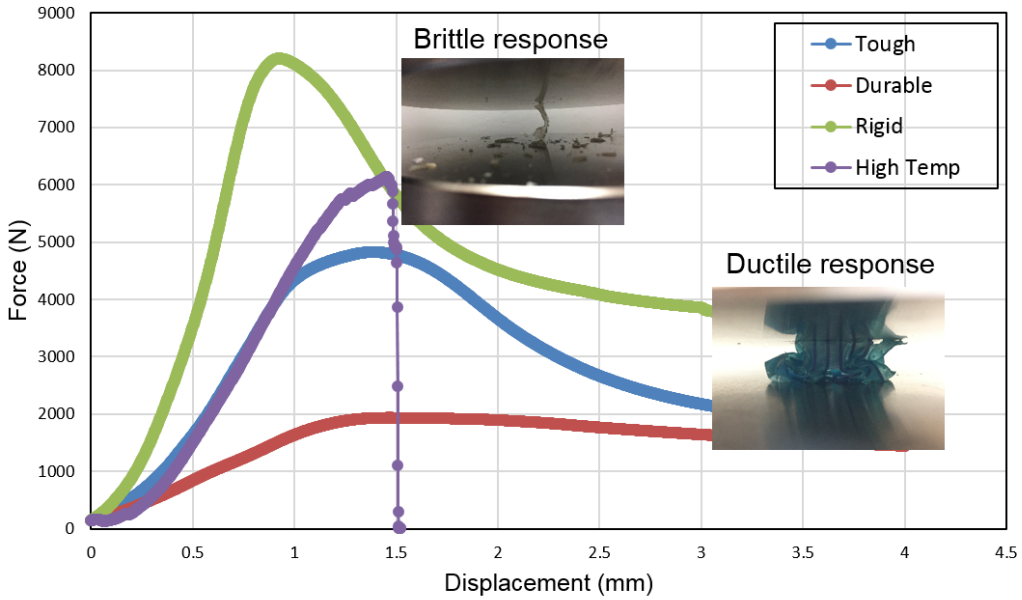

Figure 6.4 Response of three different resins in compression test. High temperature resin had brittle behavior while tough and durable resins have ductile response.

6.2.1 Wall thickness effect

We investigated variations of wall thickness, number of domains, and bridge density in comparative sets of 3D-printed scaffolds. For the wall thickness effect, four different scaffolds were designed where the thickness and number of walls were varied, listed in **Table 6.1**. Dimensions of the scaffolds are shown in **Figure 6.5(b).** To reduce the effect of the outer walls, their thickness was design to be 0.5 mm. Also, the cross sectional area of all scaffolds was kept constant to ensure

results reflect the wall thickness and number of domains effects not the material mass.

Table 6.1 Thickness and maximum force obtained for scaffolds with different number of walls

Number of walls	8	4	2	1
Wall thickness (mm)	1.65	3.3	6.6	13.2

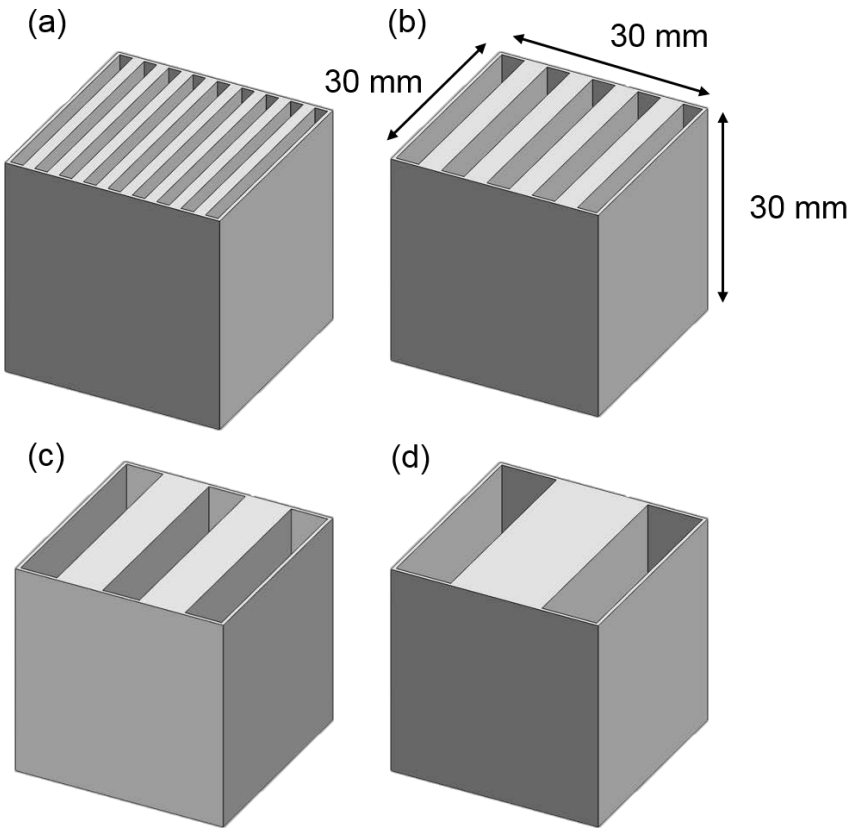

Figure 6.5 Scaffolds designed by **(a)** 8 walls, **(b)** 4 walls, **(c)** 2 walls and **(d)** 1 wall.

Results obtained from the compression test show that by decreasing the number of walls and increasing their thickness the strength of the scaffolds increased. Also, scaffolds with one wall and two walls exhibited similar behaviors.

Similar to freeze cast scaffolds[219], the predominant mode of failure was buckling (see **Figure 6.7**). Buckling of a thin plate simply supported along its edges is a standard problem in elasticity[311]. The buckling load for a thin plate with length *L*, height *H*, and thickness *t* (see **Figure 6.8**) simply supported at its edge is given by[311,312]:

$$P_c = \frac{k\pi^2}{6(1-\nu)} G \frac{t^3}{L} \tag{6.1}$$

where *G* is shear modulus, ν is Poisson's ratio, and *k* is a factor that depends on the *H/L* aspect ratio. It can be seen in equation 6.1 that elastic buckling loading for individual walls has cubic dependence on thickness. Therefore, having thicker walls is favorable for resistance against buckling.

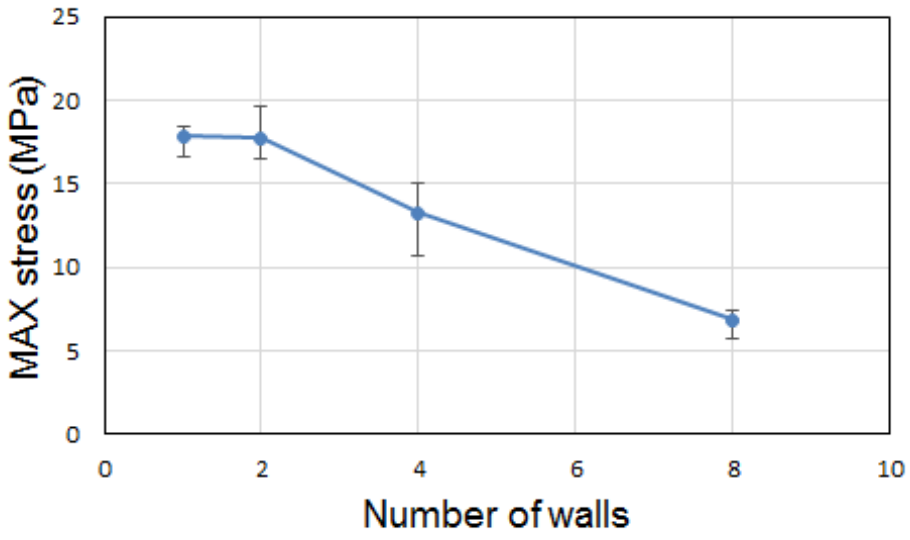

Figure 6.6 Maximum stress obtained in compression testing for scaffolds with one, two, four and eight walls. Each data has been repeated three times and error bars shows range of the data.

By dividing the buckling force by the total number of walls, a critical force per wall can be obtained. By plotting the individual wall buckling force versus thickness in **Figure 6.9**, a power law trend-line can be obtained. As it can be seen from **Figure 6.9,** buckling force is a function of plate thickness to the power of 1.934. This difference between experimental results and elastic buckling is likely due to plastic buckling for thinner walls. In fact, for slender thin plates the effect of imperfections will dominate and they will buckle earlier than the force predicted by elastic buckling[313–315]. These imperfections can arise from manufacturing or boundary conditions. By increasing the wall thickness, the effect of plastic buckling will reduce and the behavior of the plates approaches elastic buckling.

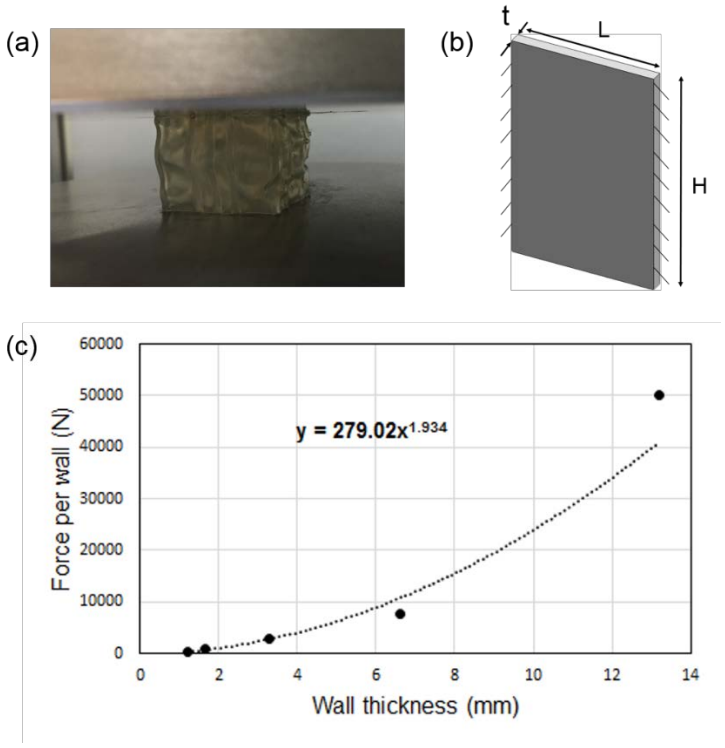

Figure 6.7 **(a)** Buckling is mode of failure. **(b)** Thin plate simply supported at the edges. H is plate height, L is plate length and t is plate thickness. **(c)** Trend of buckling load versus wall thickness.

6.2.2 Number of domains

Here, by designing different scaffolds with a various number of domains, we investigate the effect of the number of domains on strength. Scaffolds were designed with one, four, nine, sixteen and thirty six domains as shown in **Figure 6.10**. To keep the weight of all scaffolds the same, by increasing the number of domains, the thickness of these walls decreased slightly (see **Figure 6.11**). **Figure 6.12** supports the explanation. Four domains were formed by rotating sections two & three by 90 º (see **Figure 6.8b**), while sections one & four remain in the same orientation as the single-domain scaffold (see **Figure 6.8a**). However, an additional wall was added at the center to separate and stabilize the domains (yellow wall in **Figure 6.8b**). For nine domains, a similar scheme of rotating every other section 90º was maintained, but two additional walls were added (two yellow walls in **Figure 6.8c**). Thus, as walls are added, their thickness must be decreased to keep the cross-sectional area constant. The different wall thicknesses are shown in **Table 6.2**.

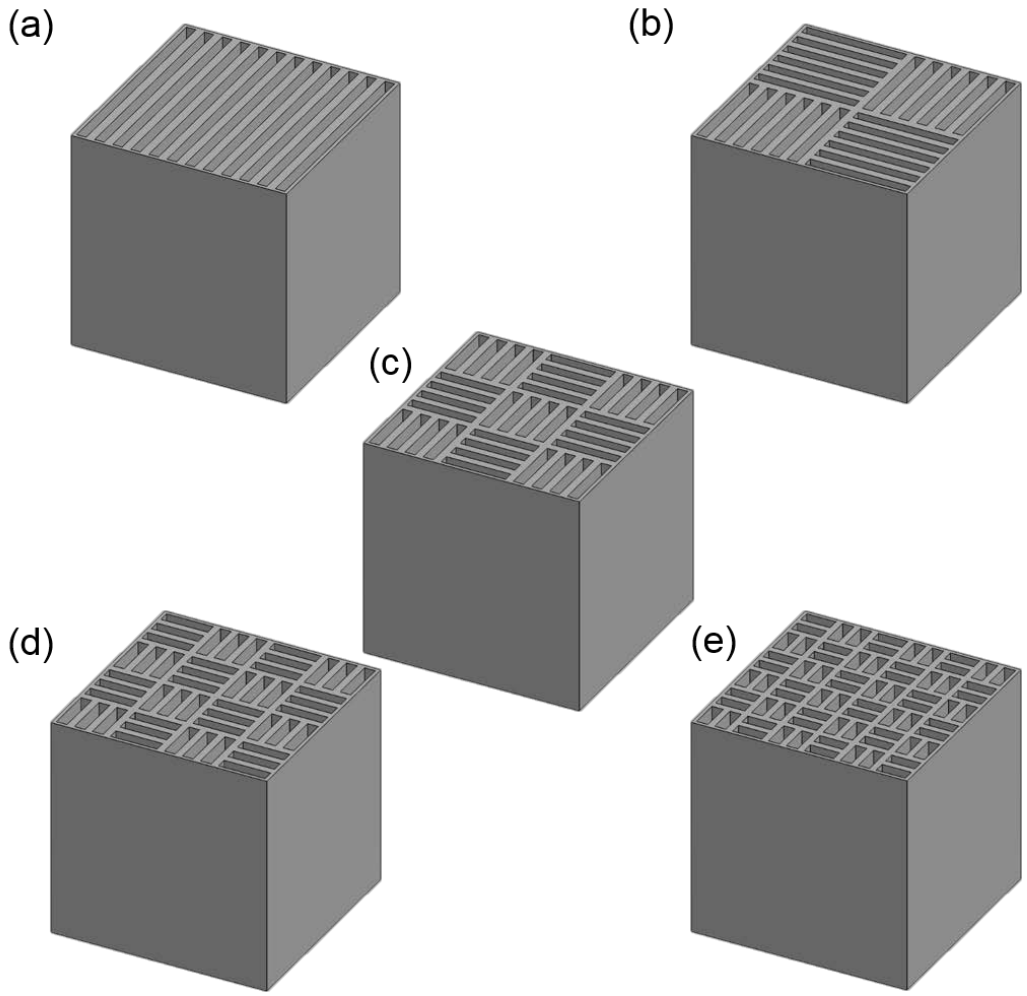

Figure 6.8 Scaffolds designed by **(a)** 1, **(b)** 4, **(c)** 9, **(d)** 16 and **(e)** 36 domains.

Table 6.2 Thickness and maximum force obtained for scaffolds with different number of domains

Number of domains	1	4	9	16	36
Wall thickness (mm)	1.2	1.14	1.09	1.02	0.93

Results of compression test are shown in **Figure 6.13.** By increasing the number of domains, the maximum force increases. Considering each wall as thin

plate simply supported at its edges and under uniaxial compression, it can be seen from equation 6.1 that the effect of increased domains results in *L* being reduced. Although increasing the number of domain reduces the wall thickness slightly, which has a negative effect on buckling, the wall length *L* dominates, leading to an increased buckling force. A similar behavior is observed in metallic square honeycomb structures under uniaxial compression[312]. To ensure material-independence, all resins were tested, and resulted in similar increasing trends as observed in the Tough resin (see **Figure 6.16**).

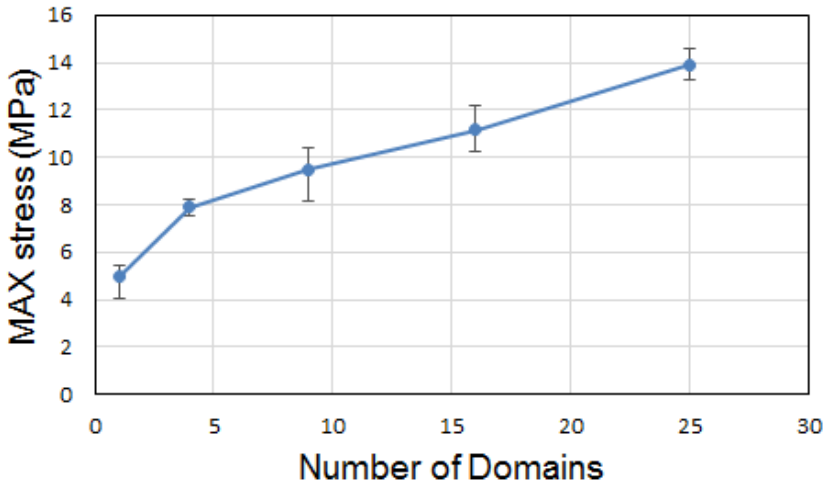

Figure 6.9 Results from the number of domains on the maximum force in the Z direction. Each test has been repeated three times and error bars show the maximum and minimum of three measurements.

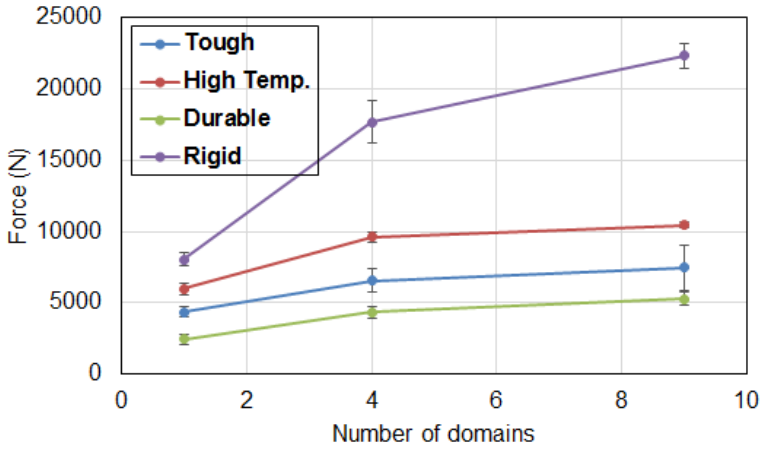

Figure 6.10 One, four and nine domains design tested with Tough, Rigid, Durable and High temperature resins.

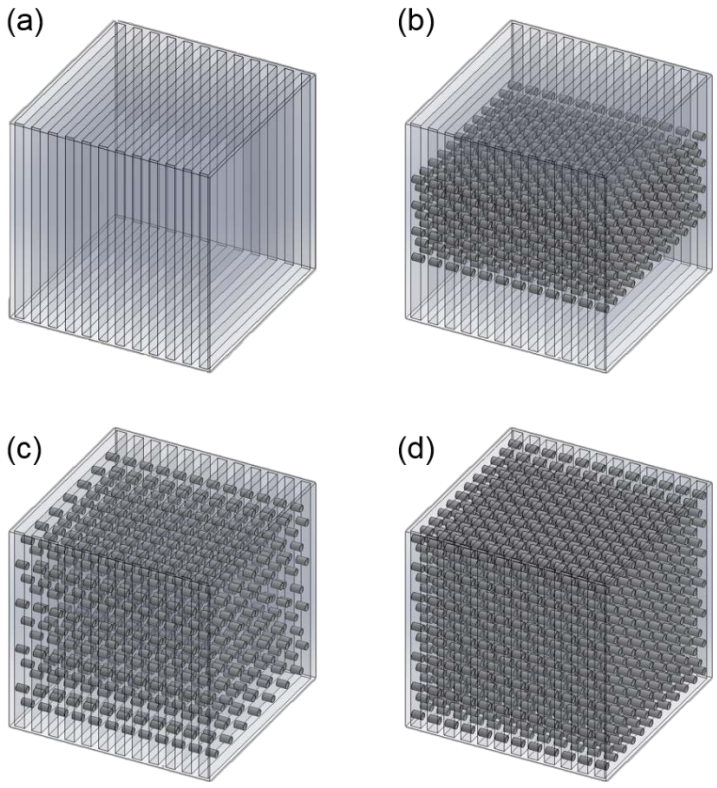

Figure 6.11 Scaffolds designed with bridges connecting adjacent walls to each other. **(a)** Scaffold with no bridge, **(b)** bridges are "around center", **(c)** bridges are distributed over the walls with "low density" and **(d)** bridges are distributed over the walls with "higher density". Transparency of the walls is reduced to show the bridges.

6.2.2 Bridge effect

Finally, the effect of bridges are investigated by adding circular bridges with 1 mm diameter between adjacent walls connecting them together. As one domain scaffold buckles at the middle, 81 bridges added were concentrated around the center of the walls with 2.3 mm spacing between them (see **Figure 6.14b**). In the next design, 67 bridges were distributed over the walls with 4 mm spacing between them (see **Figure 6.14c**). Finally, 150 bridges with 2.5 mm spacing between them were added (see **Figure 6.14d**). As observed, adding bridges between adjacent walls contributed to enhancing the strength of the scaffolds in the longitudinal (parallel to the walls) direction (see **Figure 6.15**). This is because the bridges help support the walls, providing resistance against buckling. In fact bridges act like a new boundary condition on one face, supporting the thin plate from two edges and one face. Increasing the density of the bridges contributed to enhanced strength, and also a uniform distribution of bridges resulted in even higher strength with respect to the case when bridges were concentrated at the scaffold center.

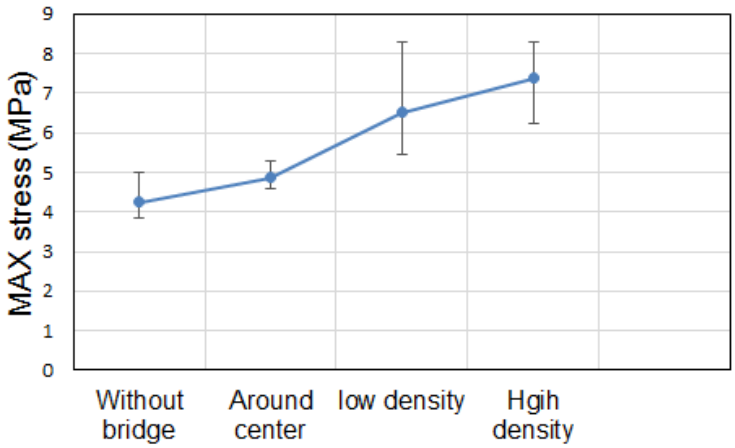

Figure 6.12 Scaffolds designed **(a)** without bridge, **(b)** bridges concentrated around the middle, **(c)** bridges distributed over the walls with lower density and **(d)** bridges distributed over the wall with higher density. Each test has been repeated three times and error bars shows the maximum and minimum of three measurements.

6.3 Discussion

As can be seen from the results obtained from the 3D printed scaffolds, thicker walls, higher number of domains, and higher density of bridges enhance the longitudinal compressive strength of the scaffolds. Therefore, in freeze cast scaffolds it is likely that higher solidification velocities, resulting in thinner walls are detrimental to strength, but at the same time a higher number of domains and bridge densities enhance strength. By considering each individual wall as a thin plate simply supported at its edges, the buckling force increases as length of the walls decreases or thickness of the walls increases. Hence, the effect of increased numbers of the domains reduces the effective length of the individual walls.

6.4 Concluding remarks

Although 3D printed scaffolds do not exactly mimic freeze cast scaffolds, the relationship between their microstructural characteristics and mechanical

properties reveal failure trends based on buckling analysis of thin plates. Our investigation shows that as long as the mode of failure is buckling, for porous scaffold-like materials with a different number of domains and wall thicknesses, thicker walls with shorter length are able to resist buckling better. Also, adding bridges between adjacent walls helps in buckling resistance. Still there are differences in microstructural morphology between the 3D printed scaffolds and freeze cast scaffolds. First, the walls in freeze cast scaffolds are porous and composed of ceramic grains (in these studies), while the 3D printed scaffolds have solid walls composed of polymers. Other differences include the orientation and size of the walls and different domains; in freeze cast scaffolds, their size and orientation are not regular, while in 3D printed ones they are of consistent size oriented in two perpendicular directions. Also, freeze cast scaffolds are made of ceramics and have micrometer length scale while 3D printed scaffolds were made of polymers with millimeter length scale which may cause different structural behavior.

CHAPTER 7

MULTIDIMENSIONAL MECHANICS

Freeze cast scaffolds made without magnetic fields have higher strength in the solidification direction but lack sufficient strength in the transverse direction. On the other hand, scaffolds made by magnetic freeze casting tend to have increased strength in the transverse direction at the cost of reduced strength in the solidification direction (see **Figure 5.5**).

Now the question arises: which scaffold is performing better? The one with outstanding properties in one direction or the other one with reasonable properties in multiple directions? Scaffolds can be compared on basis of different modes of loading as well, e.g. compression, bending, tension, impact, wear resistance. The materials that have a good amount of strength under compression, tension, and impact will be more multi-functional than the materials having outstanding values

in just one direction/mode of loading. Furthermore, this can be generalized to combine mechanical properties and performance. For example, bones not only have strength to support an organism's weight but also ensure the growth of red blood cells and protection of inner organs. So comparing materials based on their various mechanical properties or performances requires an approach capable of comparing multiple properties at the same time. Most material comparisons are commonly displayed on two-dimensional property charts comparing two properties at a time. In this study, we use radar charts to compare multiple properties at the same time. By using the radar chart, the order that properties are sequenced can provide significant information. Usually, one property can't be descriptive of the functionality of a material/organism. To find the sequence in which properties should be arranged on a radar chart, we have calculated the total maximum area of the plotted data.

7.1 Comparison of 3D-printed scaffolds based on multiple properties

From the stress-strain plot of a compression test, toughness, resilience, strain to failure and Young's modulus can be found in addition to the strength. Resilience is the area under a stress-strain curve in the elastic region; toughness is the area under the curve until compaction (for porous materials); Young's modulus is the slope of a stress-strain plot in the elastic region; and strain to failure is equal to compaction point (see **Figure 7.1**). Since scaffolds exhibit different behavior after yielding, the compaction point was defined as the point where the slope of the force increases at a rate >1000 N/mm. One additional property considered here was pore size. Pore size was each individual pore.

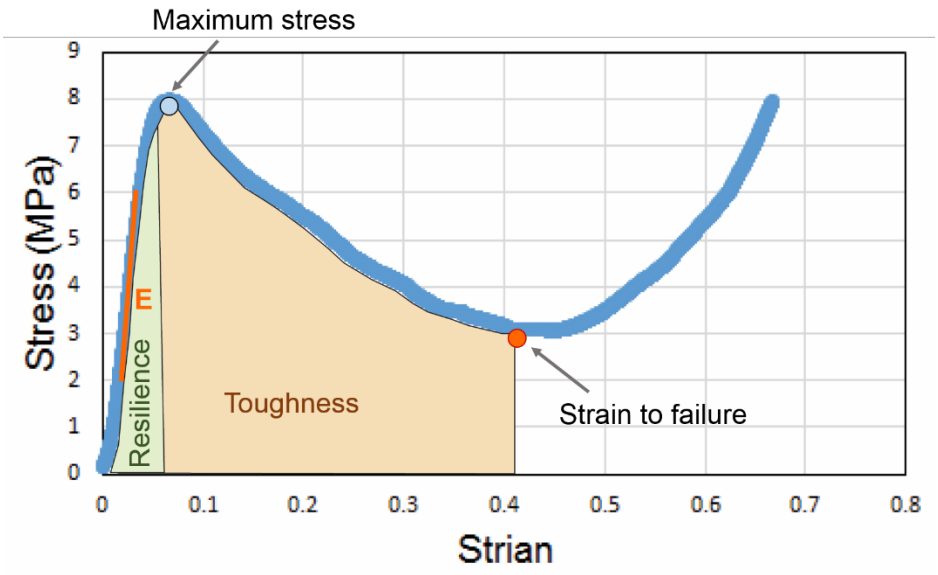

Figure 7.1 Different properties obtained from stress-strain graph. Stiffness, maximum stress, toughness, resilience and strain to failure are shown in the graph.

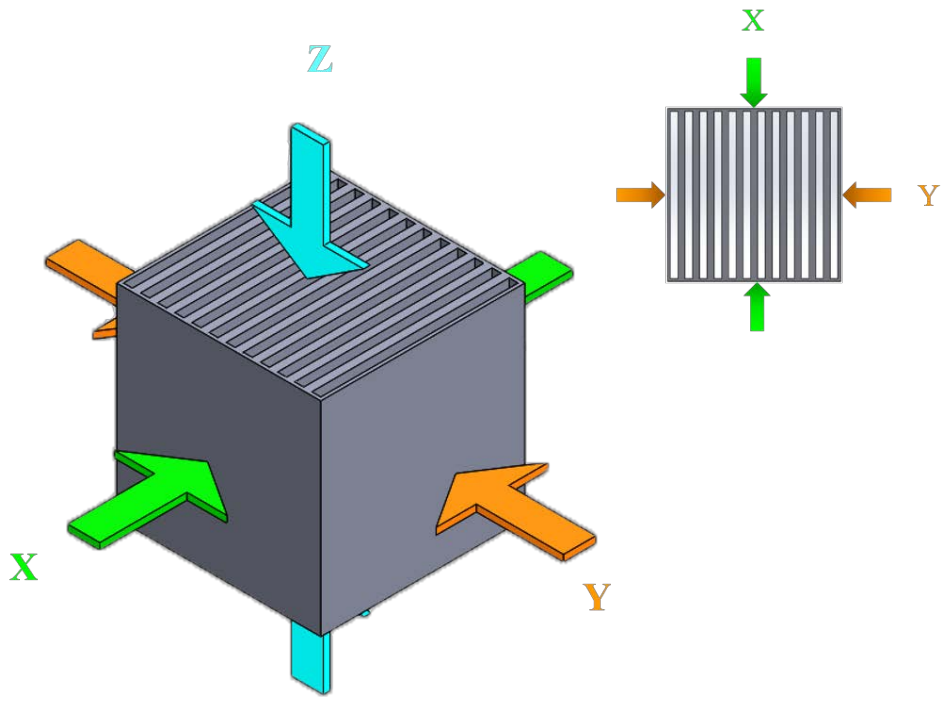

Figure 7.2 3D-printed scaffolds were tested in X, Y and Z directions.

7.2 Mechanical properties of 3D-printed scaffolds in Z direction

Scaffolds designed based on the number of walls, number of domains, and bridge density were tested in three orthogonal directions. The strength, toughness, resilience, stiffness and strain to failure were obtained from each test as discussed previously. Results are plotted in **Figure 7.4-7.6**. As seen in **Figure 7.4**, increasing the number of domains, then increases strength, toughness, resilience and stiffness. From one domain to four domains the stiffness increased noticeably. However, increasing domains further resulted in no appreciably increase in stiffness. Among the different number of domains tests, the thirty-six domains outperformed all the others while single domain scaffold had weakest performance.

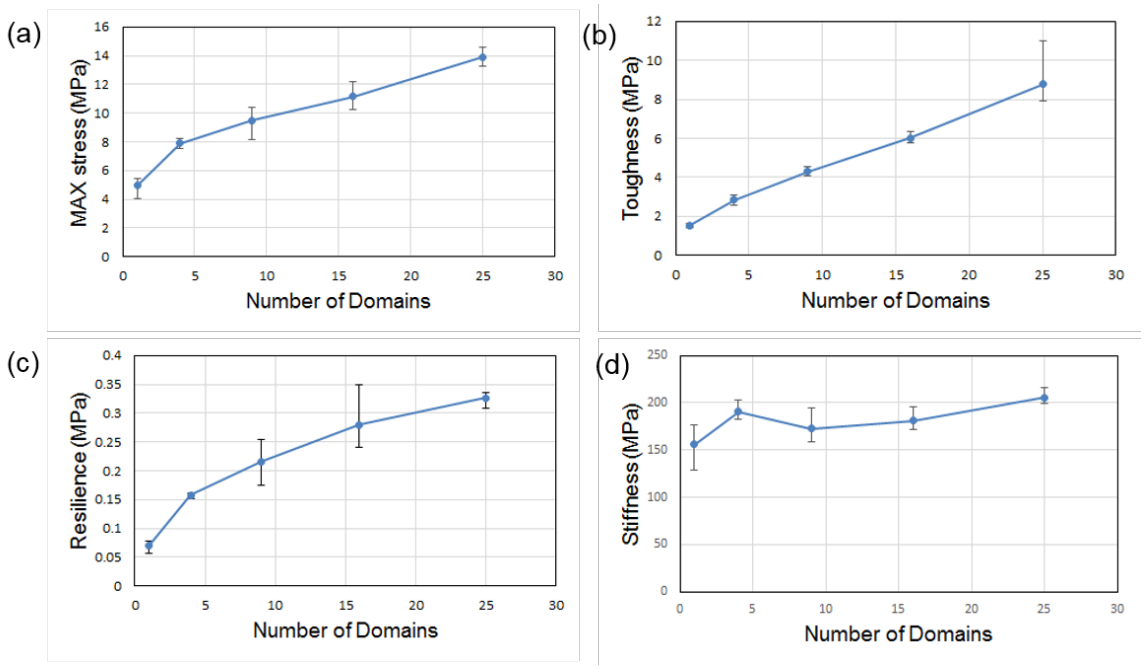

Figure 7.3 Effect of number of domains on the **(a)** maximum force, **(b)** toughness, **(c)** resilience and **(d)** stiffness in the Z direction.

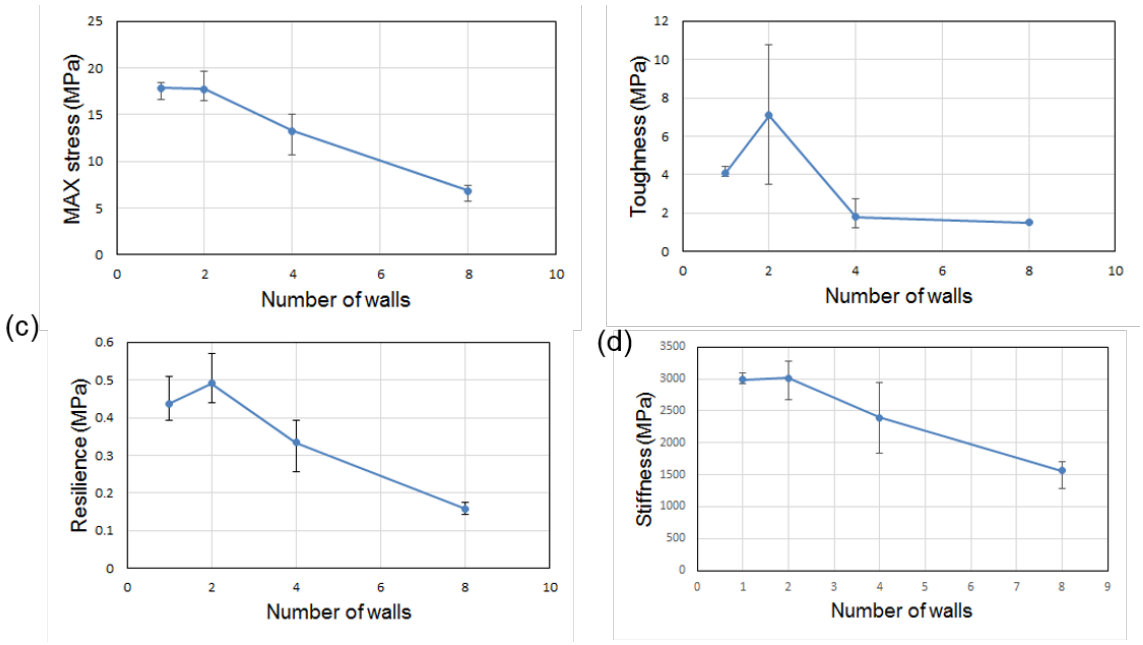

Figure 7.4 Effect of wall thickness (i.e. number of the walls) on the **(a)** maximum force, **(b)** toughness, **(c)** resilience and **(d)** stiffness in the Z direction.

For different wall thickness, it can be seen from **Figure 7.5** that by increasing thickness of the walls and decreasing number of the walls, strength, toughness, resilience and stiffness increase. Again no specific trend was observed for strain to failure. Here, scaffolds with two walls outperform the others, and those with eight walls have the weakest performance. Adding bridges led to increased strength, toughness, resilience and stiffness of the scaffolds. Also, by increasing density of the bridges, all properties enhanced too. "Around center" design yield higher toughness than low density ones, although they had the same amount of the bridges. In this design, scaffolds with the highest density of bridges had the highest performance while scaffolds without bridges had the weakest performance.

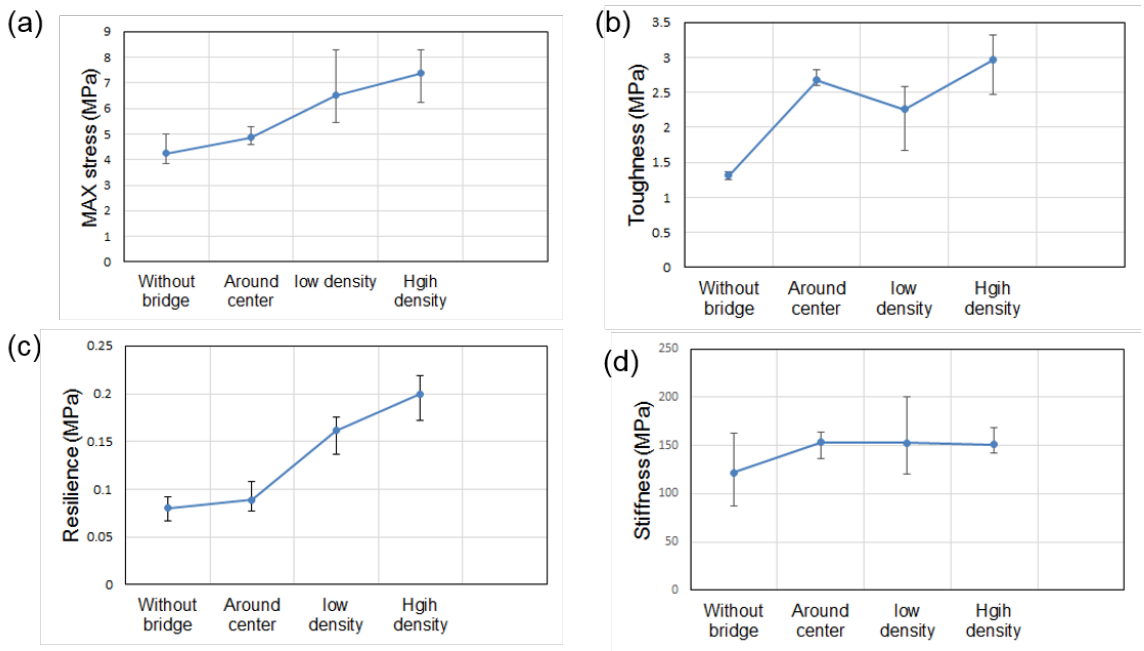

Figure 7.5 Effect of bridges on the **(a)** maximum force, **(b)** toughness, **(c)** resilience and **(d)** stiffness in the Z direction. Different designs of bridges are shown in **Figure 6.15**.

7.2 Mechanical properties of 3D-printed scaffolds in X and Y directions

In X &Y directions scaffolds with different numbers of domains had different behaviors than the Z direction. As can be seen from **Figure 7.7**, scaffolds with one domain outperformed those with four and nine domains, but by increasing the number domains to sixteen and thirty six, mechanical properties will go beyond those of one domain. Therefore, scaffolds with thirty six domains had best performance and those with four domains had weakest performance. The reason for this is the alignment of walls in X direction for one domain. By increasing number of domains, the number of straight walls in X direction increases, which results in enhancement of mechanical properties in this direction (see **Figure 7.8**). Although scaffolds with thirty six domains have five walls and those with one

domain have eleven walls, those with thirty six domains have superior mechanical properties due to fact that walls are strengthen with horizontal walls.

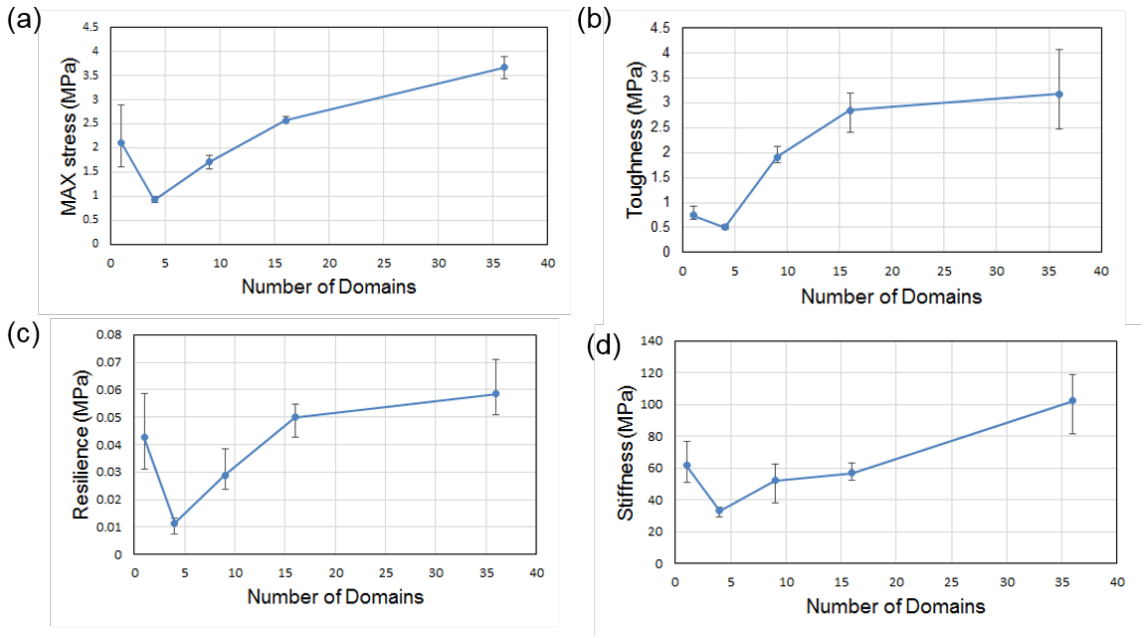

Figure 7.6 Effect of number of domains on the **(a)** maximum force, **(b)** toughness, **(c)** resilience and **(d)** stiffness in the X direction.

For bridges, “around the center” design had superior performance. It was observed first scaffolds buckle at opposite directions then they all buckle in one direction (see **Figure 7.10**). The reason for such behavior is not clear yet. By increasing the bridge density, all properties increased.

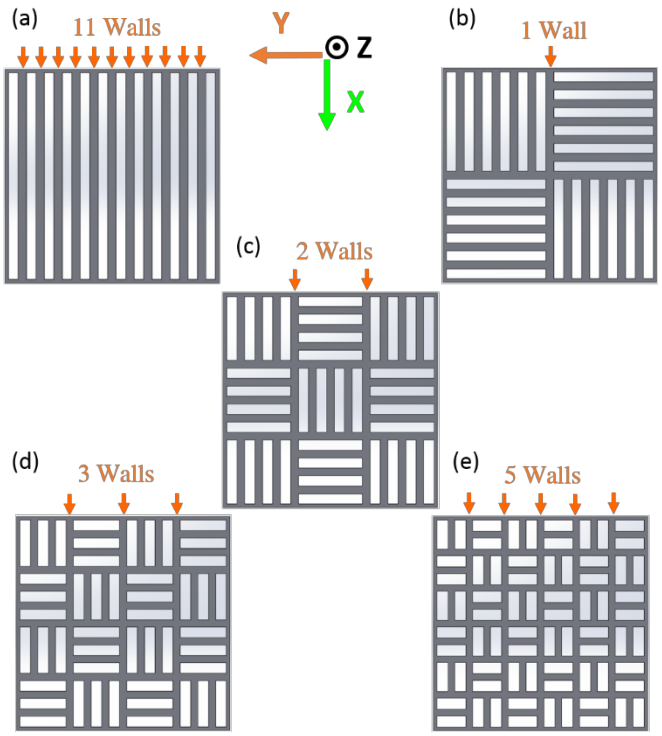

Figure 7.7 Cross section of scaffolds with different number of domains. **(a)** For one domain all walls are in X direction, **(b)** for four domains, one wall is in X direction, **(c)** for nine domains two walls are in X direction, **(d)** for sixteen domains three walls are in X direction and **(e)** for thirty six domains five walls are in X direction. X,Y and Z directions are shown in the image.

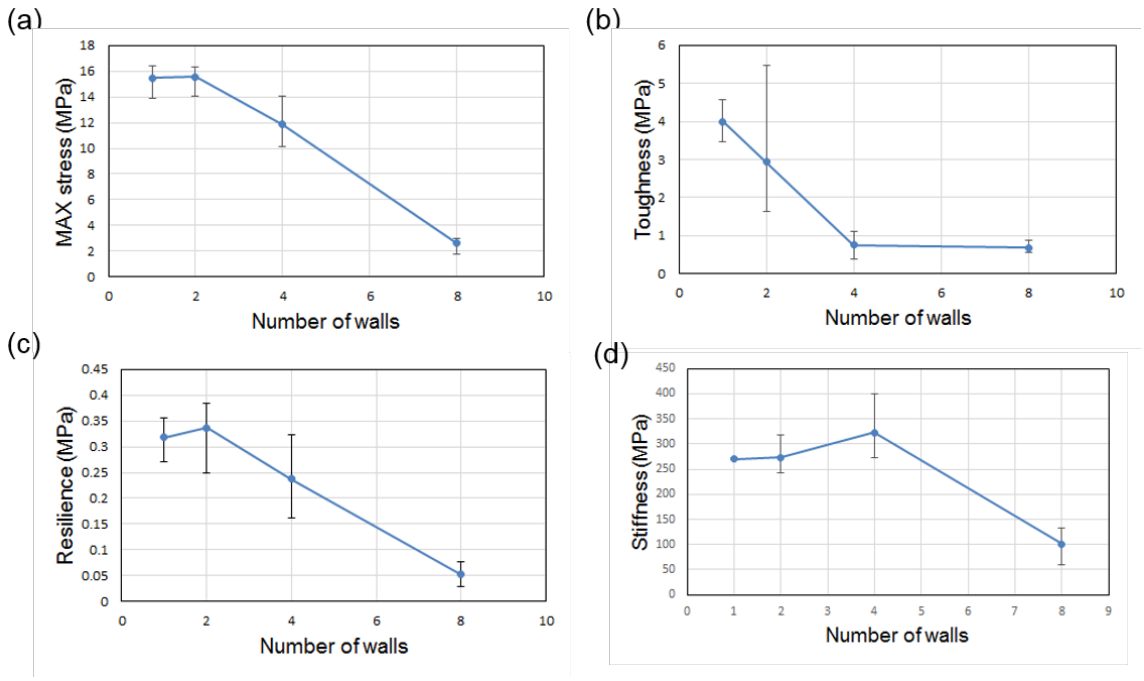

Figure 7.8 Effect of wall thickness on the **(a)** maximum force, **(b)** toughness, **(c)** resilience and **(d)** stiffness in the X direction.

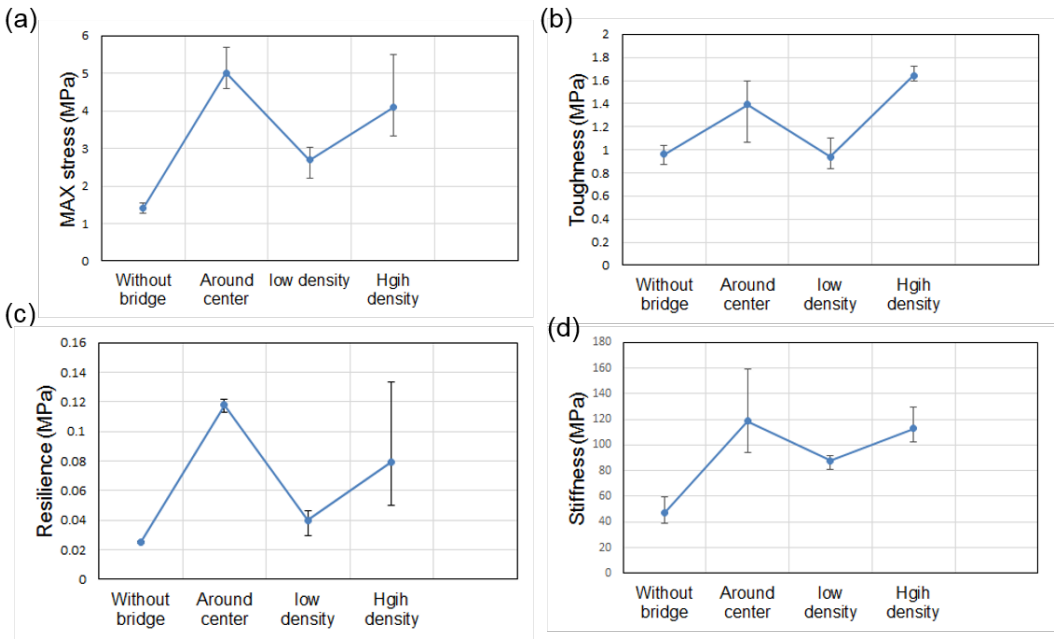

Figure 7.9 Effect of bridges on the **(a)** maximum force, **(b)** toughness, **(c)** resilience and **(d)** stiffness in the X direction.

In the Y direction, the behaviors of the scaffolds were similar to that of Z direction, as by increasing the number of domains, strength, toughness, resilience, and stiffness also increased (see **Figure 7.12**). Regardless of wall thickness, the behavior was opposite to the Z and X directions; by increasing wall thickness and decreasing number of walls, all properties decreased (see **Figure 7.13**). The reason is that in the Y direction, force is tolerated by the outer shell, and for scaffolds with more walls, spacing between walls decreases, which enhances buckling resistance of the outer shell. For those with bridges, adding and increasing density of bridges, enhances all properties in Y direction, as bridges bear the load in the Y direction (see **Figure 7.14**).

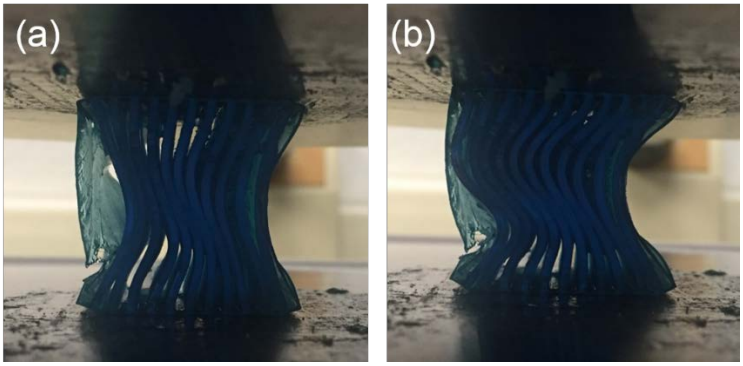

Figure 7.10 Deflection of “around the center” design of bridges in the X direction. **(a)** First walls buckle in opposite directions, **(b)** then they all buckle in the same direction.

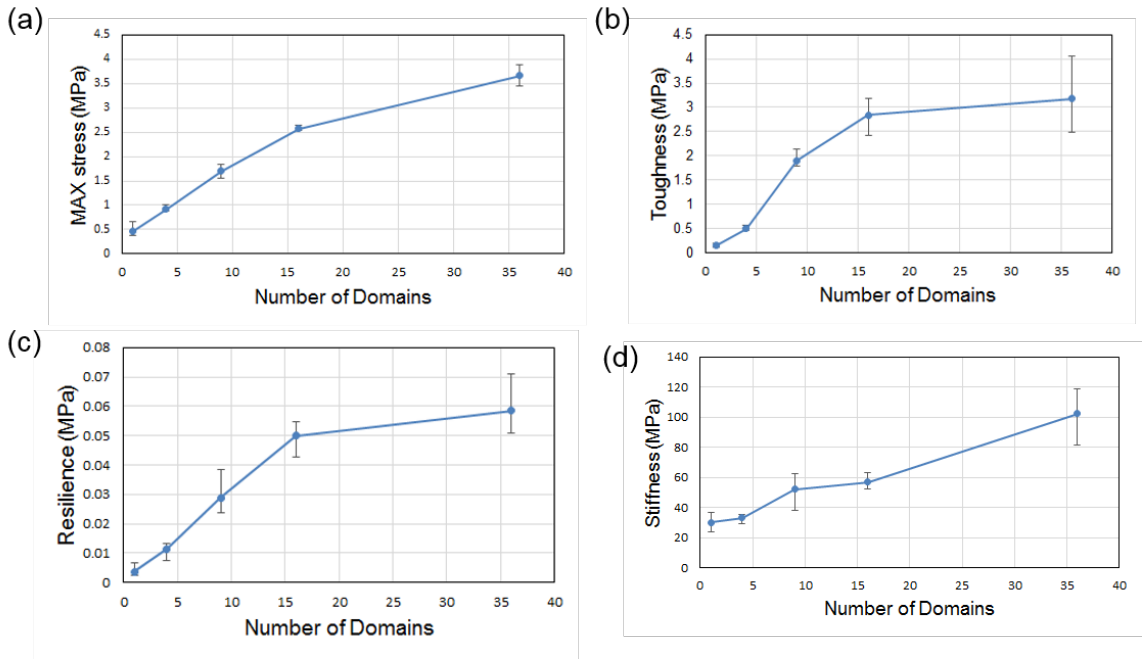

Figure 7.11 Effect of number of domains on the **(a)** maximum force, **(b)** toughness, **(c)** resilience and **(d)** stiffness in the Y direction.

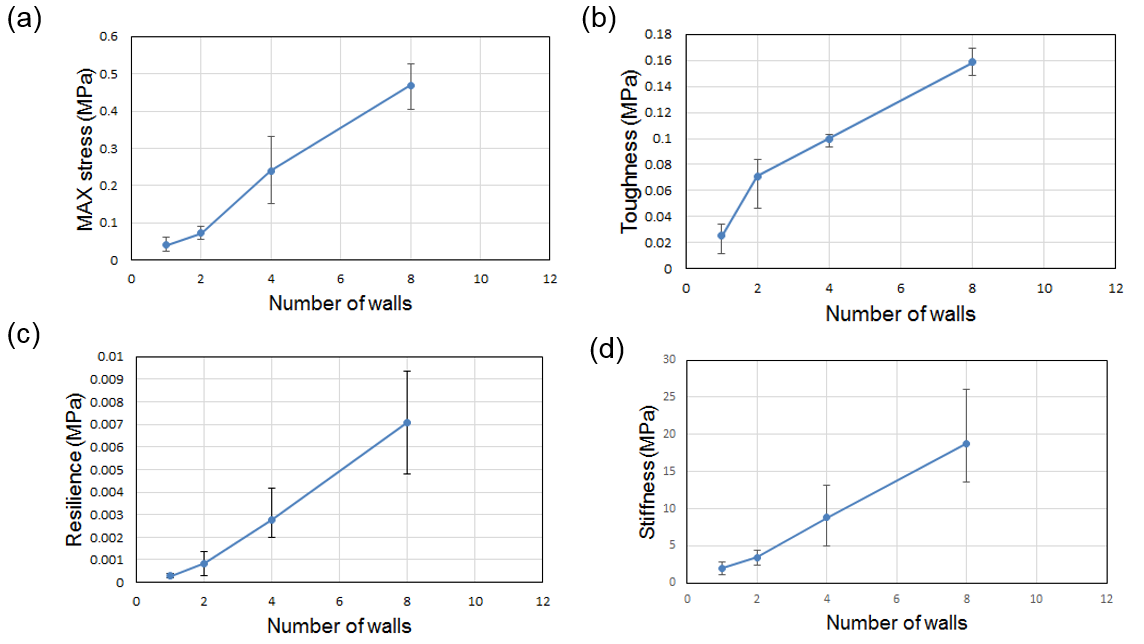

Figure 7.12 Effect of wall thickness on the **(a)** maximum force, **(b)** toughness, **(c)** resilience and **(d)** stiffness in the Y direction.

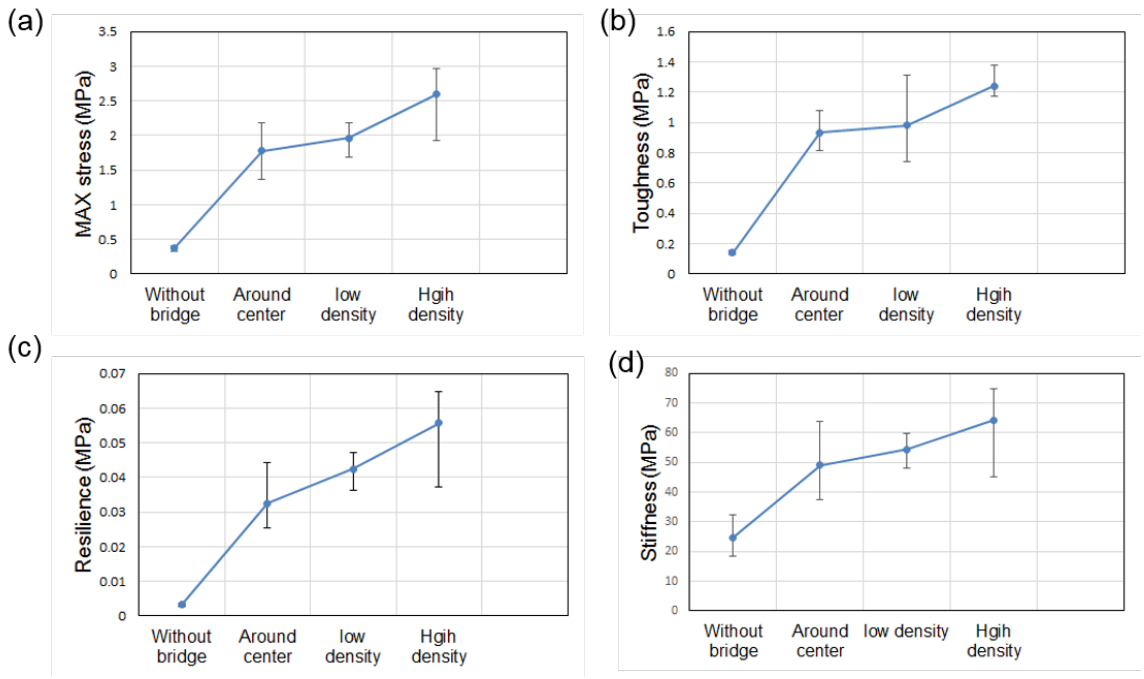

Figure 7.13 Effect of bridges on the **(a)** maximum force, **(b)** toughness, **(c)** resilience and **(d)** stiffness in the Y direction.

7.3 Radar chart method

By utilizing radar charts, multiple properties of a system can be shown on a single radar chart. The concern with radar charts, however, is that the order of the properties is subjective. Here, we applied the maximal area permutation[316] method to determine the sequence of properties on the radar charts. To explain this further, let's consider five systems (shown with different colors in **Figure 7.15**) that are compared across five different properties (P1-P5 in **Figure 7.15**). First, the property values are normalized by the maximum value of each property category[316]:

$$p_{ij} = \bar{P}_{ij} / \max \bar{P}_i \tag{7.1}$$

where the *j* subscript shows different properties and *i* different systems. Hence, each property axis ranges from 0 to 1. All possible combinations that the properties

can be sorted are shown in **Figure 7.16.** Total number of all possible permutations is given by[316]:

$$\mathcal{N} = \frac{(N-1)!}{2} \tag{7.2}$$

For each of these permutations, each system is plotted as an area on the radar chart. The total area is obtained by the summation of the areas of all five systems. Area of each system is given by[316]:

$$A_j = \frac{1}{2}\left(\begin{vmatrix} x_1 & x_2 \\ y_1 & y_2 \end{vmatrix} + \begin{vmatrix} x_2 & x_3 \\ y_2 & y_3 \end{vmatrix} + \cdots + \begin{vmatrix} x_N & x_1 \\ y_N & y_1 \end{vmatrix}\right)_j \tag{7.3}$$

And total area is found by summation over the areas:

$$\tilde{A} = max \sum_{j=1}^{n} A_j \tag{7.4}$$

In this case of maximal area, the properties that have values close to each other are sorted next to each other, and often correlated with specific functionalities of the system. Here, the radar chart method is applied to the 3D printed scaffolds.

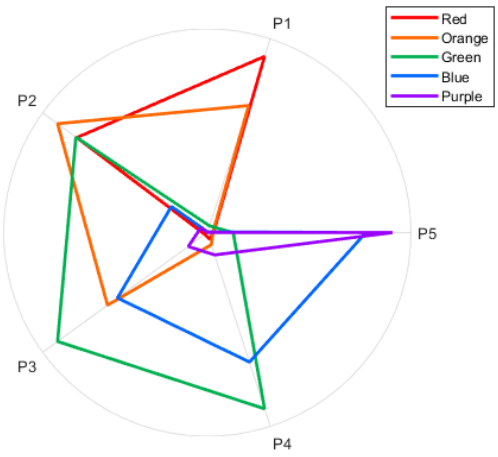

Figure 7.14 Radar chart for five systems compared based on five properties.

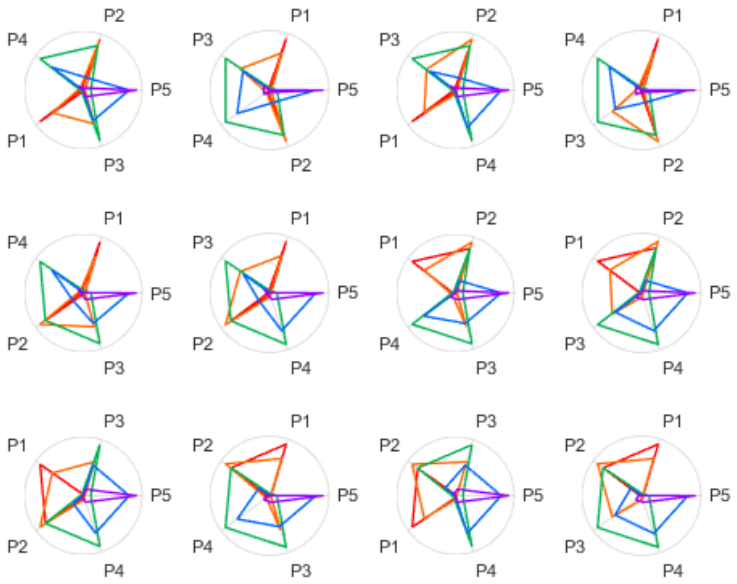

Figure 7.15 All possible permutations for five different properties. Different colors are showing different systems.

7.4 Comparison of scaffolds based on multiple properties with radar charts

Rather than comparing the different properties of scaffolds in multiple charts, radar charts can be utilized to combine all of those plots together. As an example, all four plots of **Figure 7.4** can be displayed on the radar charts in **Figure 7.16c**.

Now, by looking at the radar charts of **Figure 7.16**, the performance of the scaffolds with different numbers of domains bases on five different properties can be compared. As can be seen from **Figure 7.16c**, an increased number of domains did not affect strain to failure that much and the stiffness has increased slightly, but strength, toughness, and resilience have increased substantially. Also, the inner polygon (one domain) has the lowest performance and the outer polygon (thirty-six domains) has the highest. In the X direction, the four-domain polygon is the

inner one (weakest performance), while the thirty-six domain is still the best (see **Figure 7.16a**). The reason for this increase in performance with increasing domains is that buckling after yielding occurs periodically, rather than abrupt dropping as each domain collapses (see **Figure 7.17**). The behavior of scaffolds with different number of domains in Y direction is following almost the same pattern seen in Z direction.

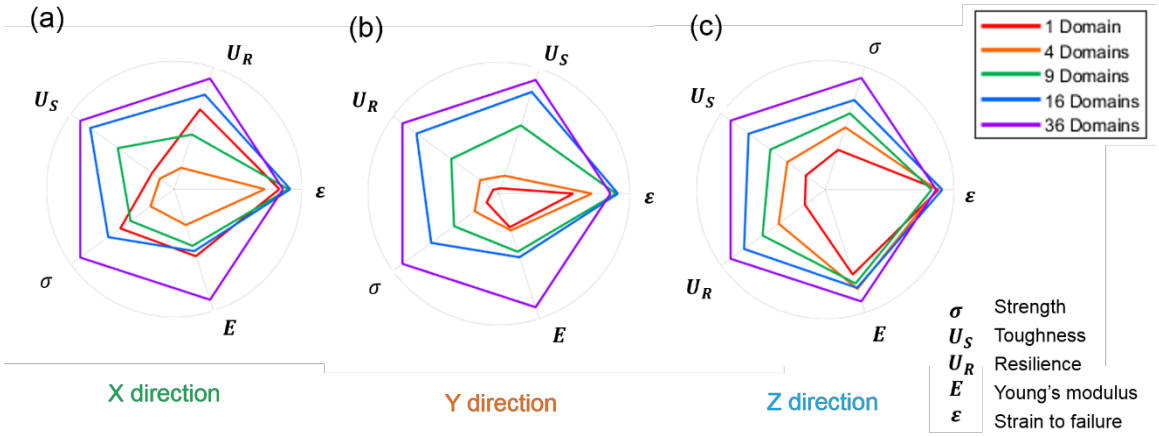

Figure 7.16 Radar chart for scaffolds with different number of domains in the **(a)** X, **(b)** Y and **(c)** Z directions. All properties on axes are normalized with maximum value in that property category and are from zero to one.

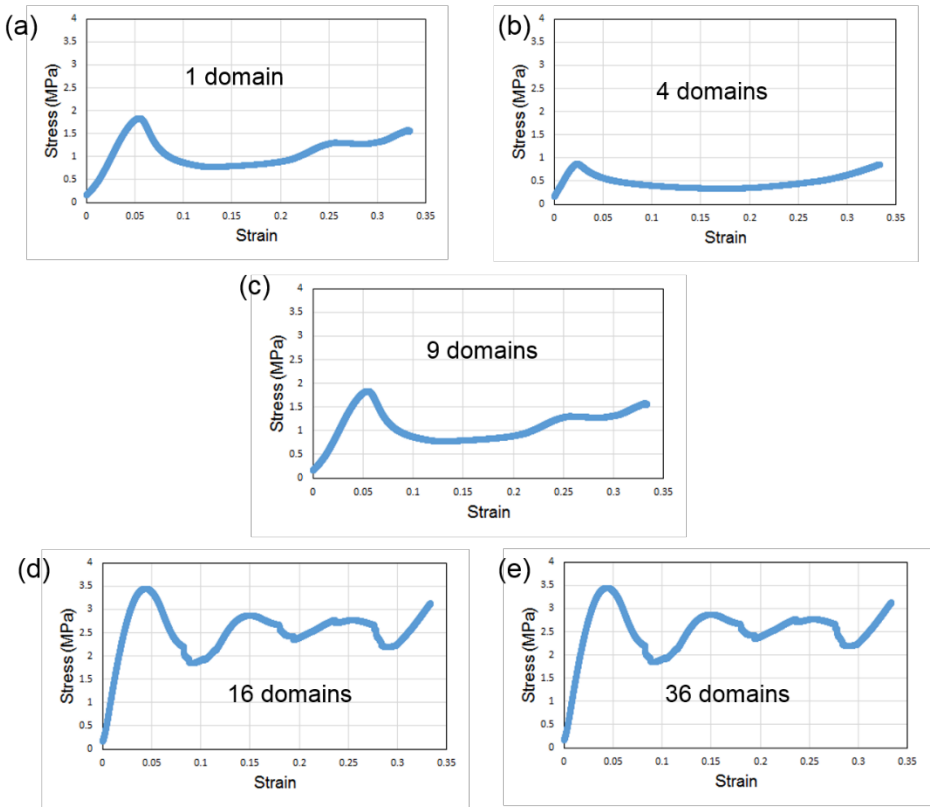

Figure 7.17 Post yielding behavior for scaffolds with **(a)** one domain, **(b)** four domains, **(c)** nine domains, **(d)** sixteen domains and **(e)** thirty six domains in X direction.

For different walls with different thicknesses, one and two walls have higher strength, resilience, and toughness in the Z and X directions (see **Figure 7.18b&c**). In contrast, in the Y direction the eight wall scaffold is outperforming all other scaffolds (see **Figure 7.18b**). For the bridge design, in the Z direction the highest density of bridges perform the best while the scaffold without bridges performs the worst. Interestingly, in the X direction, the bridges “around the center” exhibit the highest performance, while the scaffold without bridges again exhibits the weakest performance (see **Figure 7.19**).

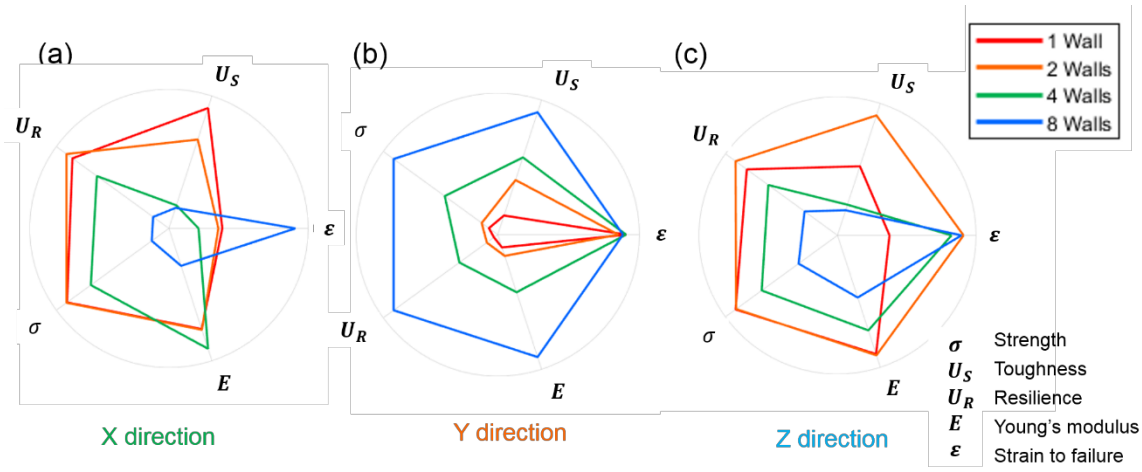

Figure 7.18 Radar chart for scaffolds with different wall thickness in X, Y and Z directions.

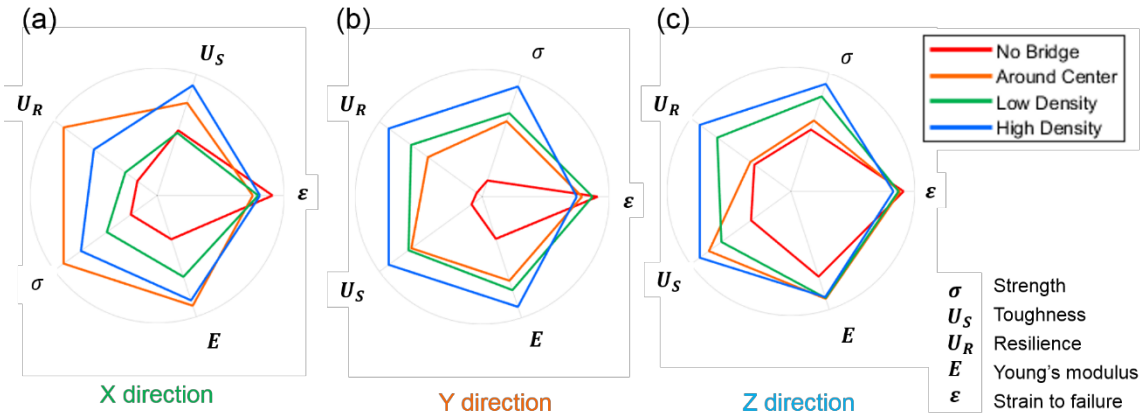

Figure 7.19 Radar chart for scaffolds with different density of bridges in X, Y and Z directions.

One advantage of radar charts is that multiple properties can be analyzed simultaneously. Next, we compare the behavior of all systems in three different directions. In **Figure 7.20** all three different designs, i.e. different numbers of domains, different wall thicknesses and different bridge densities, are compared together in the Z direction. Adding bridges or increasing the number of domains enhances most mechanical properties, while the effect of increasing the number of domains is more dominant. Comparing the increased number of domains versus

increased wall thickness shows that increased thickness of the walls resulted in better strength, resilience, and stiffness at the cost of increased pore size (see **Figure 7.20**). Both designs resulted in nearly the same toughness.

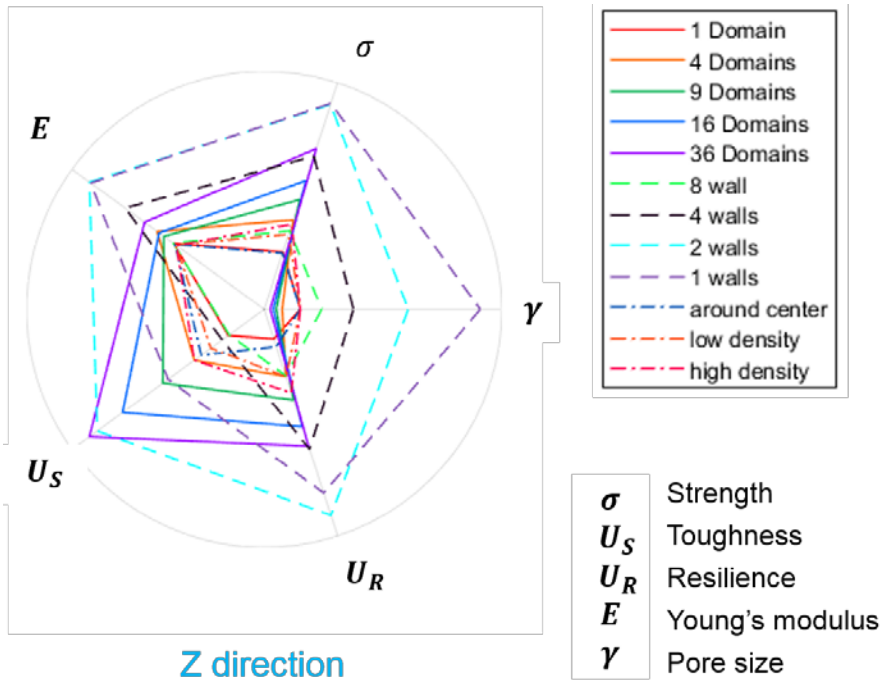

Figure 7.20 Comparison of all designs with radar chart based on strength, toughness, resilience, Young's modulus and pore distribution in the solidification direction.

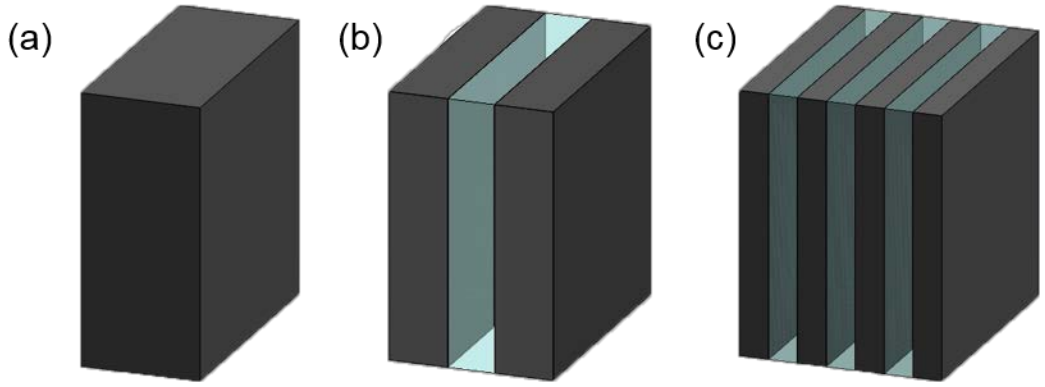

Figure 7.21 Outer walls are removed to show increasing pore size will turn porous scaffolds to more solid ones. Scaffolds with **(a)** one wall, **(b)** two walls, and **(c)** four walls. Light green regions are showing the pores.

An interesting observation in **Figure 7.20** is the order of properties, where strength (σ) and stiffness (E) are next to each other which shows their correlation; stiff materials are usually strong too. Also, pore size is placed between strength and resilience. In fact by increasing pore size, scaffolds are getting closer to solid materials rather than porous ones (see **Figure 7.21**). This leads to increased strength and stiffness of materials as solid materials are stronger and stiffer than porous materials. Scaffolds with increased thickness of the walls are stronger and stiffer than scaffolds with increased number of domains but they almost have same toughness (see **Figure 7.20**). Adding porosity sometimes increases the toughness of materials, even in different modes of failure. As an example, in tension, pores causes crack deflection and resist failure or in compression, increased porosity causes a gradual decrease in maximum load after yielding rather than an abrupt drop as seen in one-domain scaffold (see **Figure 7.22**). Also, from **Figure 7.20**, the relevant effect of each design can be compared visually. The effect of the bridges is small compared to the increased number of domains and increased wall thickness.

In the X direction, a similar trend to solidification direction is observed with the exception that the effect of the wall thickness is more dominant than the increased number of domains**.** In the X direction the bridge design and increased number of domains contribute to enhancement of mechanical properties almost with the same degree (see **Figure 7.23**). Increased thickness of the walls increases the mechanical properties significantly as seen in **Figure 7.23,** where

the effect of wall thickness is more dominant than the increased number of domains. Again, for scaffold with thirty six domain, it has noticeable toughness compared to other properties due to homogenous distribution of the pores.

In contrast, in the Y direction, design with increased thickness of the walls had lowest performance while increased number of domains outperformed the others and bridge design had performance between those (see **Figure 7.24)**.

Finally, the strength, stiffness and toughness of all designs in three orthogonal directions are compared in **Figure 7.25**. In all three directions, the strength and stiffness are placed next to each other showing how stiffness is correlated with strength. Also, seen form **Figure 7.25** that scaffolds with different wall thickness are outperforming the others Z & X direction while they have very weak performance in Y direction. Scaffolds with different number of domains have high performance in the Y direction while in the X direction they have weaker performance compared to the wall thickness design. Bridge design has behavior similar to increased number of the domains design while increased number of domains design is performing better. From **Figure 7.25** can be seen that

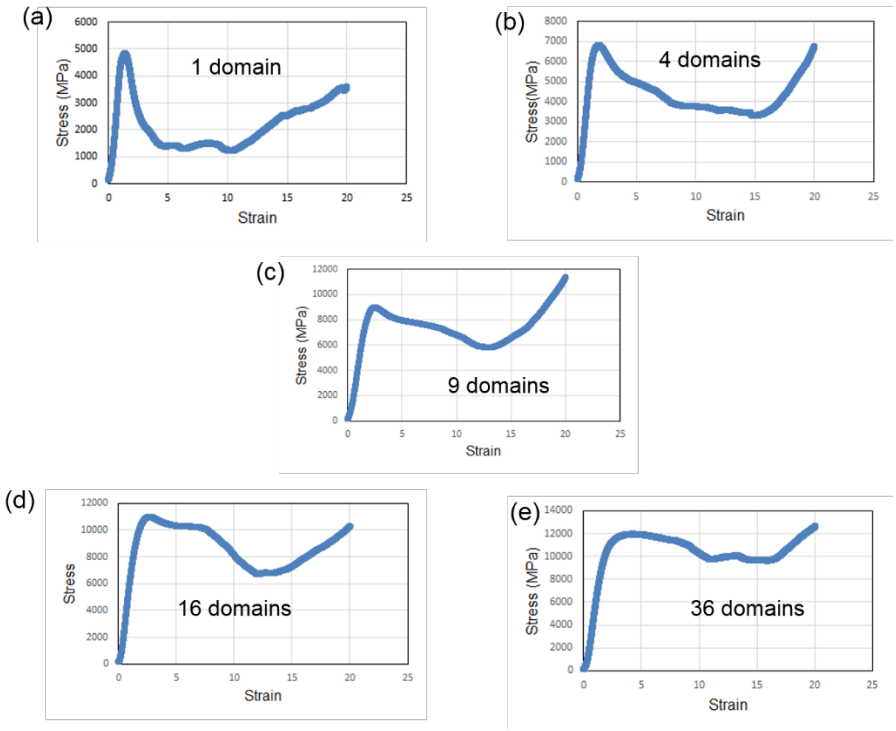

Figure 7.22 Failure behavior of scaffolds with **(a)** one, **(b)** four, **(c)** nine, **(d)** sixteen and **(e)** thirty six domains in the Z direction.

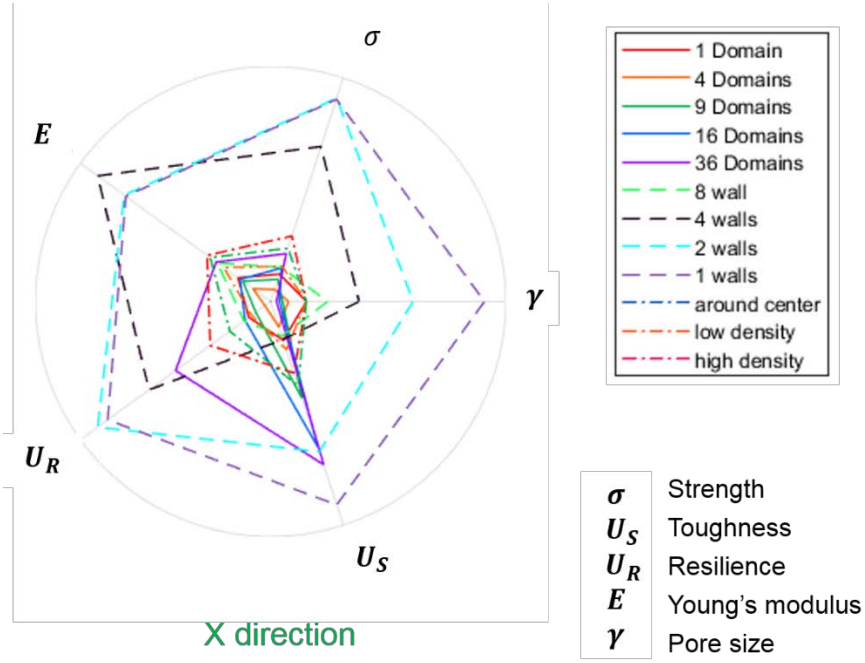

Figure 7.23 Comparison of all designs with radar chart based on strength, toughness, resilience, Young's modulus and pore distribution in the X direction.

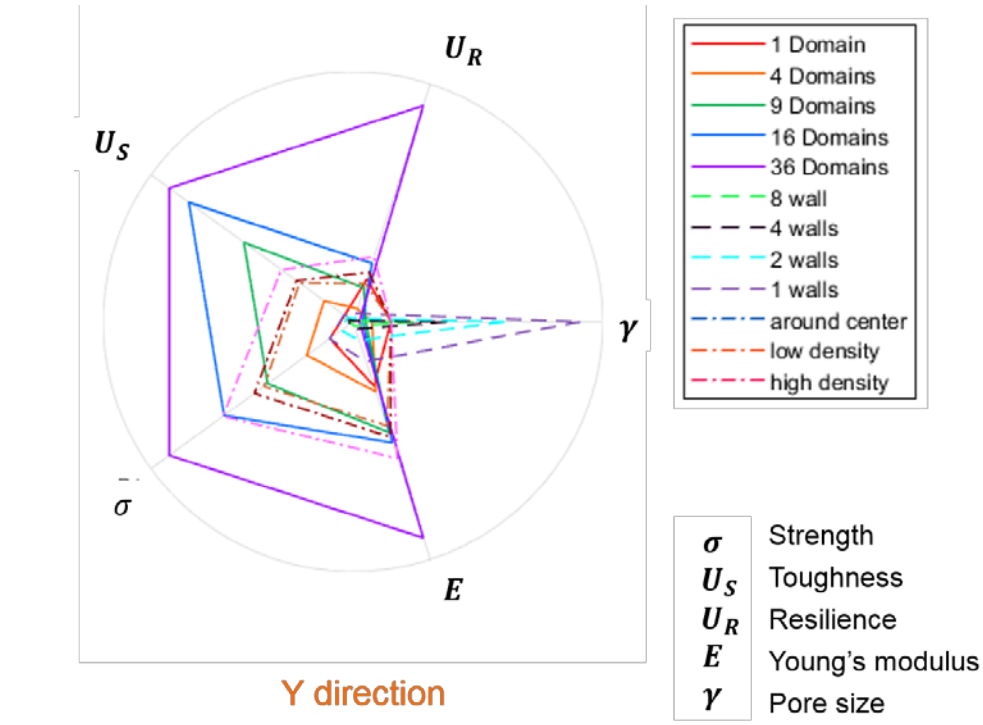

Figure 7.24 Comparison of all designs with radar chart based on strength, toughness, resilience, Young's modulus and pore distribution in the Y direction.

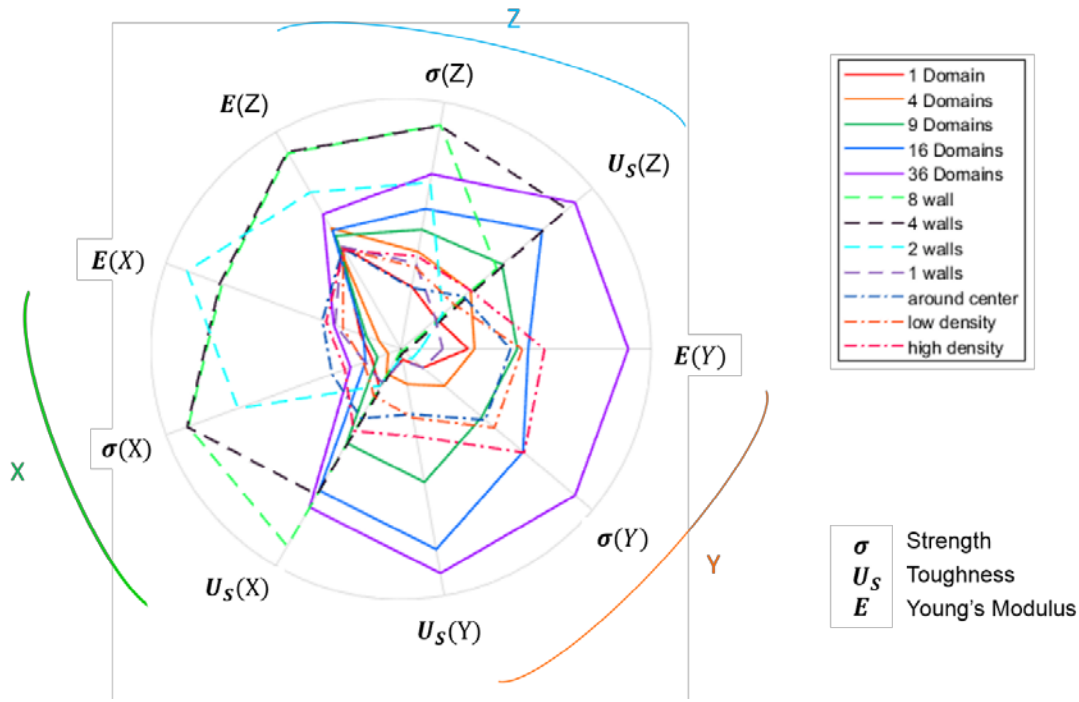

Figure 7.25 Comparison of strength (σ), toughness and stiffness for different domains, different wall thickness and bridge designs in three orthogonal directions.

7.8 Concluding remarks

Investigating the compression strength of 3D-printed materials in orthogonal directions showed that they behave differently in different directions. Scaffolds with four and nine domains, performed better in the Z direction, while in the X direction, scaffolds with one domain performed best. In bridge design, “around the center” outperformed the others in the X direction, while scaffolds with a higher density of mineral bridges performed better in the other directions. This shows the importance of considering properties of materials in multiple directions or even in different modes of loading to reveal multi-functionality and also determine mechanisms that contribute to performance enhancement. For this purpose, the permutated radar chart method was applied to the 3D printed scaffolds, and shows different advantages. First, multiple properties with various systems can be compared on a single chart, rather than using several 2D graphs, which avoids cluttering. Also, the order of properties on a radar chart can reveal relationships between different properties that in some cases reveal functionality of the systems. This is something that cannot be easily observed from common 2D plots. Also, permutated radar charts can be used to compare different materials/systems based on mechanical properties or functions. This can also be extended to combinations of them.

REFERENCES

1. Licavoli JJ, Gao MC, Sears JS, Jablonski PD, Hawk JA. Microstructure and Mechanical Behavior of High-Entropy Alloys. *J Mater Eng Perform*. 2015;24(10):3685-3698. doi:10.1007/s11665-015-1679-7
2. Holcomb GR, Tylczak J, Carney C. Oxidation of CoCrFeMnNi High Entropy Alloys. *Jom*. 2015;67(10):2326-2339. doi:10.1007/s11837-015-1517-2
3. J. D. C. *Bones: Structure and Mechanics*. Princeton: Princeton University Press; 2002.
4. Gibson LJ. Cellular solids. *Mrs Bull*. 2003;28(04):270-274.
5. Fukasawa T, Deng ZY, Ando M, Ohji T, Goto Y. Pore structure of porous ceramics synthesized from water-based slurry by freeze-dry process. *J Mater Sci*. 2001;36(10):2523-2527. doi:10.1023/A:1017946518955
6. Gaudillere C, Garcia-Fayos J, Balaguer M, Serra JM. Enhanced Oxygen Separation through Robust Freeze-Cast Bilayered Dual-Phase Membranes. *ChemSusChem*. 2014;7(9):2554-2561. doi:10.1002/cssc.201402324
7. Lichtner AZ, Jauffrès D, Roussel D, Charlot F, Martin CL, Bordia RK. Dispersion , connectivity and tortuosity of hierarchical porosity composite SOFC cathodes prepared by freeze-casting. *J Eur Ceram Soc*. 2015;35(2):585-595. doi:10.1016/j.jeurceramsoc.2014.09.030
8. Behr S, Behr S, Amin R, Chiang Y, Tomsia AP. Highly-Structured , Additive-Free Lithium-Ion Cathodes by Freeze-Casting Technology. 2015;(August).
9. Shapiro J. Freezing-out, a safe technique for concentration of dilute solutions. *Science (80-)*. 1961;133(3470).
10. Tang XC, Pikal MJ. Design of Freeze-Drying Processes for Pharmaceuticals : Practical Advice. 2004;21(2).
11. Frohberg P, Nguyen TNP, Ulrich J. New aspects in the formulation of drugs based on three case studies. *Molecules*. 2016;21(5). doi:10.3390/molecules21050577
12. Kumar RS, McDowell DL. Generalized continuum modeling of 2-D periodic cellular solids. *Int J Solids Struct*. 2004;41(26):7399-7422. doi:10.1016/j.ijsolstr.2004.06.038
13. Gu S, Lu TJ, Evans AG. On the design of two-dimensional cellular metals for combined heat dissipation and structural load capacity. *Int J Heat Mass Transf*. 2001;44(11):2163-2175. doi:10.1016/S0017-9310(00)00234-9
14. Wang A-J, McDowell DL. In-Plane Stiffness and Yield Strength of Periodic Metal Honeycombs. *J Eng Mater Technol*. 2004;126(2):137. doi:10.1115/1.1646165
15. Taylor CM, Smith CW, Miller W, Evans KE. The effects of hierarchy on the in-plane elastic properties of honeycombs. *Int J Solids Struct*. 2011;48(9):1330-1339. doi:10.1016/j.ijsolstr.2011.01.017
16. Ajdari A, Jahromi BH, Papadopoulos J, Nayeb-Hashemi H, Vaziri A. Hierarchical honeycombs with tailorable properties. *Int J Solids Struct*. 2012;49(11-12):1413-1419. doi:10.1016/j.ijsolstr.2012.02.029
17. Chen Q, Pugno N, Zhao K, Li Z. Mechanical properties of a hollow-cylindrical-joint honeycomb. *Compos Struct*. 2014;109(1):68-74. doi:10.1016/j.compstruct.2013.10.025
18. Naleway SE, Porter MM, McKittrick J, Meyers MA. Structural Design Elements in Biological Materials: Application to Bioinspiration. *Adv Mater*. 2015;27(37):5455-5476. doi:10.1002/adma.201502403
19. Herzog A, Klingner R, Vogt U, Graule T. Wood-Derived Porous SiC Ceramics by Sol

Infiltration and Carbothermal Reduction. *J Am Ceram Soc*. 2004;87(5):784-793. doi:10.1111/j.1551-2916.2004.00784.x

20. Sieber H, Hoffmann C, Kaindl a., Greil P. Biomorphic cellular ceramics. *Adv Eng Mater*. 2000;2(3):105-109. doi:10.1002/(SICI)1527-2648(200003)2:3<105::AID-ADEM105>3.3.CO;2-G

21. Cao J, Rambo CR, Sieber H. Preparation of Porous Al 2 O 3 -Ceramics by Biotemplating of Wood. *J Porous Mater*. 2004;11(3):163-172. doi:10.1023/B:JOPO.0000038012.58705.c9

22. Sepulveda P, Binner JG. Processing of cellular ceramics by foaming and in situ polymerisation of organic monomers. *J Eur Ceram Soc*. 1999;19(12):2059-2066. doi:10.1016/S0955-2219(99)00024-2

23. Pokhrel A, Seo DN, Lee ST, Kim IJ. Processing of porous ceramics by direct foaming: A review. *J Korean Ceram Soc*. 2013;50(2):93-102. doi:10.4191/kcers.2013.50.2.093

24. Colombo P, Hellmann JR. Ceramic foams from preceramic polymers. *Mater Res Innov*. 2002;6(5-6):260-272.

25. Lam CXF, Mo XM, Teoh SH, Hutmacher DW. Scaffold development using 3D printing with a starch-based polymer. *Mater Sci Eng C*. 2002;20(1-2):49-56. doi:10.1016/S0928-4931(02)00012-7

26. Bose S, Vahabzadeh S, Bandyopadhyay A. Bone tissue engineering using 3D printing. *Mater Today*. 2013;16(12):496-504. doi:10.1016/j.mattod.2013.11.017

27. Sajadi SM, Owuor PS, Schara S, et al. Multiscale Geometric Design Principles Applied to 3D Printed Schwarzites. *Adv Mater*. 2018;30(1):1-8. doi:10.1002/adma.201704820

28. Hench LL, West JK. The sol-gel process. *Chem Rev*. 1990;90(1):33-72. doi:10.1021/cr00099a003

29. Budd K, Key SK, Payne DA. Sol-gel processing of {PbTiO} 3, {PbZrO} 3, {PZT} and {PLZT} thin films. *{BR} {CERAM} {PROC} {Br} {Ceram} {Proc}*. 1985;(January 1985):107.

30. Saboori A, Rabiee M, Moztarzadeh F, Sheikhi M, Tahriri M, Karimi M. Synthesis , characterization and in vitro bioactivity of sol-gel-derived SiO 2 – CaO – P 2 O 5 – MgO bioglass. *Mater Sci Eng C*. 2009;29(1):335-340. doi:10.1016/j.msec.2008.07.004

31. Doshi J, Reneker DH. Electrospinning Process and Applications of Electrospun Fibers. *Ind Appl Soc Annu Meet 1993, Conf Rec 1993 IEEE*. 1993;3:1698-1703. doi:10.1109/IAS.1993.299067

32. Deville S. Freeze-casting of porous ceramics: A review of current achievements and issues. *Adv Eng Mater*. 2008;10(3):155-169. doi:10.1002/adem.200700270

33. Reed JS. *Principles of Ceramics Processing*. 2nd ed. Wiley; 1995.

34. Mutsuddy BC, Ford RG. *Ceramic Injection Molding*. 1st ed. Springer Science & Business Media; 1994.

35. Atre S V, Weaver TJ, German RM. Injection molding of metals and ceramics. 1998;(724). doi:10.4271/982417

36. Mangels JA. Low-pressure injection molding. *Am Ceram Soc Bull*. 1994;73(5).

37. Fanelli AJ, Silvers RD, Frei WS, Burlew J V., Marsh GB. New aqueous injection molding process for ceramic powders. *ournal Am Ceram Soc*. 1989;72(10).

38. Janney MA, Omatete OO, Walls CA, Nunn SD, Ogle RJ, Westmoreland G. Development of Low-Toxicity Gelcasting Systems. *J Am Ceram Soc*. 2005;81(3):581-591. doi:10.1111/j.1151-2916.1998.tb02377.x

39. Omatete OO, Strehlow RA, Walls CA. Drying of gelcast ceramics. *Oak Ridge Natl Lab*. 1991.

40. Chen Y, Xie Z, Yang J, Huang Y. Alumina casting based on gelation of gelatine. *J Eur Ceram Soc*. 1999;19(2):271-275. doi:10.1016/S0955-2219(98)00201-5

41. Schilling CH, Bellman RA, Smith RM, Goel H, Giesche H. Plasticizing Aqueous Suspensions of Concentrated Alumina with Maltodextrin Sugar. *J Am Ceram Soc*. 2004;82(1):57-66. doi:10.1111/j.1151-2916.1999.tb01723.x

42. Russell-Floyd RS, Harris B, Cooke RG, et al. Application of Sol-Gel Processing Techniques for the Manufacture of Fiber-Reinforced Ceramics. *J Am Ceram Soc*. 1993;76(10):2635-2643.

43. Sofie SW, Dogan F. Freeze casting of aqueous alumina slurries with glycerol.pdf. 2001;64(188747):1459-1464.

44. Deville S. Freeze-casting of porous biomaterials: Structure, properties and opportunities. *Materials (Basel)*. 2010;3(3):1913-1927. doi:10.3390/ma3031913

45. Shaga A, Shen P, Guo RF, Jiang QC. Effects of oxide addition on the microstructure and mechanical properties of lamellar SiC scaffolds and Al-Si-Mg/SiC composites prepared by freeze casting and pressureless infiltration. *Ceram Int*. 2016;42(8):9653-9659. doi:10.1016/j.ceramint.2016.03.052

46. Wang Y, Shen P, Guo RF, Hu ZJ, Jiang QC. Developing high toughness and strength Al/TiC composites using ice-templating and pressure infiltration. *Ceram Int*. 2017;43(4):3831-3838. doi:10.1016/j.ceramint.2016.12.038

47. Colard CAL, Cave RA, Grossiord N, Covington JA, Bon SAF. Conducting nanocomposite polymer foams from Ice-crystal-templated assembly of mixtures of colloids. *Adv Mater*. 2009;21(28):2894-2898. doi:10.1002/adma.200803007

48. Madihally S V., Matthew HWT. Porous chitosan scaffolds for tissue engineering. *Biomaterials*. 1999;20(12):1133-1142. doi:10.1016/S0142-9612(99)00011-3

49. Schoof H, Bruns L, Fischer A, Heschel I, Rau G. Dendritic ice morphology in unidirectionally solidified collagen suspensions. *J Cryst Growth*. 2000;209(1):122-129. doi:10.1016/S0022-0248(99)00519-9

50. Yook SW, Kim HE, Koh YH. Fabrication of porous titanium scaffolds with high compressive strength using camphene-based freeze casting. *Mater Lett*. 2009;63(17):1502-1504. doi:10.1016/j.matlet.2009.03.056

51. Chino Y, Dunand DC. Directionally freeze-cast titanium foam with aligned, elongated pores. *Acta Mater*. 2008;56(1):105-113. doi:10.1016/j.actamat.2007.09.002

52. Park H, Choi M, Choe H, Dunand DC. Microstructure and compressive behavior of ice-templated copper foams with directional, lamellar pores. *Mater Sci Eng A*. 2017;679(October 2016):435-445. doi:10.1016/j.msea.2016.10.057

53. Fukasawa T, Ando M, Ohji T, Kanzaki S. Synthesis of Porous Ceramics with Complex Pore Structure by Freeze-Dry Processing. *J Am Ceram Soc*. 2001;84(1):230-232.

54. Mazur P. Cryobiology: the freezing of biological systems. *Science (80-)*. 1970;168(3934).

55. MASHL SJ, FLORES RA, TRIVEDI R. Dynamics of Solidification in 2% Corn Starch-Water Mixtures: Effect of Variations in Freezing Rate on Product Homogeneity. *J Food Sci*. 1996;61(4).

56. Nguyen PTN, Ulrich J. Fast Dispersible Cocoa Tablets: A Case Study of Freeze-Casting Applied to Foods. *Chem Eng Technol*. 2014;37(8):1376-1382. doi:10.1002/ceat.201400032

57. Choi H, Park H, Um JH, Yoon WS, Choe H. Processing and characterization of titanium dioxide grown on titanium foam for potential use as Li-ion electrode. *Appl Surf Sci*. 2017;411:363-367. doi:10.1016/j.apsusc.2017.03.122

58. Zuo P, Zhang W, Hua J, et al. A Novel One-dimensional Reduced Graphene Oxide/Sulfur Nanoscroll Material and its Application in Lithium Sulfur Batteries. *Electrochim Acta*. 2016;222:1861-1869. doi:10.1016/j.electacta.2016.11.179

59. Gay G, Azouni MA. Forced migration of nonsoluble and soluble metallic pollutants ahead of a Liquid - Solid Interface during Unidirectional Freezing of Dilute Clayey Suspensions. 2002:0-5.

60. Northcott KA, Snape I, Scales PJ, Stevens GW. Contaminated water treatment in cold regions : an example of coagulation and dewatering modelling in Antarctica. 2005;41:61-72. doi:10.1016/j.coldregions.2004.10.003

61. Xing Z, Zhou W, Du F, et al. Facile Synthesis of Hierarchical Porous TiO 2 Ceramics with Enhanced Photocatalytic Performance for Micropolluted Pesticide Degradation. 2014. doi:10.1021/am5034236

62. Xing Z, Li J, Wang Q, et al. A floating porous crystalline TiO2ceramic with enhanced photocatalytic performance for wastewater decontamination. *Eur J Inorg Chem*. 2013;(13):2411-2417. doi:10.1002/ejic.201201494

63. Chen C, Zhang Y, Zeng J, et al. Aligned macroporous TiO2/chitosan/reduced graphene oxide (rGO) composites for photocatalytic applications. *Appl Surf Sci*. 2017;424:170-176. doi:10.1016/j.apsusc.2017.02.137

64. Barrow M, Eltmimi A, Ahmed A, Myers P, Zhang H. Frozen polymerization for aligned porous structures with enhanced mechanical stability, conductivity, and as stationary phase for HPLC. *J Mater Chem*. 2012;22(23):11615. doi:10.1039/c2jm31425h

65. Kuang J, Dai Z, Liu L, Yang Z, Jin M, Zhang Z. Synergistic effects from graphene and carbon nanotubes endow ordered hierarchical structure foams with a combination of compressibility, super-elasticity and stability and potential application as pressure sensors. *Nanoscale*. 2015;7(20):9252-9260. doi:10.1039/C5NR00841G

66. Li Y, Zhao M, Chen J, et al. Flexible chitosan/carbon nanotubes aerogel, a robust matrix for in-situ growth and non-enzymatic biosensing applications. *Sensors Actuators, B Chem*. 2016;232:750-757. doi:10.1016/j.snb.2016.04.023

67. Kuang J, Liu L, Gao Y, et al. A hierarchically structured graphene foam and its potential as a large-scale strain-gauge sensor. *Nanoscale*. 2013;5(24):12171. doi:10.1039/c3nr03379a

68. Nguyen TNP, Ulrich J. Requirements for Designing a Freeze Casting Process for Drugs ??? Rheological Properties of Suspensions. *Chem Eng Technol*. 2016;39(7):1231-1236. doi:10.1002/ceat.201600036

69. Ulrich J. An Alternative Technology to Form Tablets. 2010;(5):757-761. doi:10.1002/ceat.200900576

70. Gannon P, Sofie S, Deibert M, Smith R, Gorokhovsky V. Thin film YSZ coatings on functionally graded freeze cast NiO/YSZ SOFC anode supports. *J Appl Electrochem*. 2009;39(4):497-502. doi:10.1007/s10800-008-9682-4

71. J. M. Smith, H. C. Van Ness MM, Abbott. *Introduction to Chemical Engineering Thermodynamics*. 6th ed. McGraw-Hill; 2001.

72. J. N. Reddy. *An Introduction to Continnum Mechanics*. 2nd ed. Cambridge university press; 2013.

73. Currie IG. Fundamental Mechanics of Fluids. *Mech Eng*. 2003;1:xiv, 525 p. doi:10.1017/CBO9781107415324.004

74. Niksiar P, Ashrafizadeh A, Shams M, Madani AH. Implementation of a GPU-based CFD code. *Proc - 2014 Int Conf Comput Sci Comput Intell CSCI 2014*. 2014;1(1):84-89. doi:10.1109/CSCI.2014.21

75. Reynolds WC, Perkins HC. *Engineering Thermodynamics*. 2nd ed. McGraw-Hill; 1977.

76. Sonntag RE, Van Wylen GJ. Introduction to Thermodynamics : classical and statistical. 1991.

77. Deville S, Saiz E, Nalla R k., Tomsia AP. Freezing as a Path to Build Complex Composites. *Science (80-)*. 2006;311(5760):515-518. doi:10.1126/science.1120937

78. Oxley HR, Corkhill PH, Fitton JH, Tighe BJ. Macroporous hydrogels for biomedical applications: methodology and morphology. *Biomaterials*. 1993;14(14):1064-1072. doi:10.1016/0142-9612(93)90207-I

79. Francis NL, Hunger PM, Donius AE, Wegst UGK, Wheatley MA. Strategies for neurotrophin-3 and chondroitinase ABC release from freeze-cast chitosan–alginate nerve-guidance scaffolds. *J Tissue Eng Regen Med*. 2017;11(1):285-294. doi:10.1002/term.1912

80. Wegst UGK, Schecter M, Donius AE, Hunger PM. Biomaterials by freeze casting. *Philos Trans R Soc A Math Phys Eng Sci*. 2010;368(1917):2099-2121. doi:10.1098/rsta.2010.0014

81. Flauder S, Sajzew R, Müller FA. Mechanical properties of porous β-tricalcium phosphate composites prepared by ice-templating and poly(σ-caprolactone) impregnation. *ACS Appl Mater Interfaces*. 2015;7(1):845-851. doi:10.1021/am507333q

82. Fu Q, Rahaman MN, Bal BS, Brown RF. Preparation and in vitro evaluation of bioactive glass (13-93) scaffolds with oriented microstructures for repair and regeneration of load-bearing bones. *J Biomed Mater Res - Part A*. 2010;93(4):1380-1390. doi:10.1002/jbm.a.32637

83. Plunk AA, Dunand DC. Iron foams created by directional freeze casting of iron oxide, reduction and sintering. *Mater Lett*. 2017;191:112-115. doi:10.1016/j.matlet.2016.12.104

84. Jenei P, Choi H, Tóth A, Choe H, Gubicza J. Mechanical behavior and microstructure of compressed Ti foams synthesized via freeze casting. *J Mech Behav Biomed Mater*. 2016;63:407-416. doi:10.1016/j.jmbbm.2016.07.012

85. Huang Y, Onyeri S, Siewe M, Moshfeghian A, Madihally S V. In vitro characterization of chitosan-gelatin scaffolds for tissue engineering. *Biomaterials*. 2005;26(36):7616-7627. doi:10.1016/j.biomaterials.2005.05.036

86. Zhang N, Qiu H, Si Y, Wang W, Gao J. Fabrication of highly porous biodegradable monoliths strengthened by graphene oxide and their adsorption of metal ions. *Carbon N Y*. 2011;49(3):827-837. doi:10.1016/j.carbon.2010.10.024

87. Guo R fen, Shen P, Sun C, Wang Y, Shaga A, Jiang Q chuan. Processing and mechanical properties of lamellar-structured Al-7Si-5Cu/TiC composites. *Mater Des*. 2016;106:446-453. doi:10.1016/j.matdes.2016.06.008

88. Koh YH, Sun JJ, Kim HE. Freeze casting of porous Ni-YSZ cermets. *Mater Lett*. 2007;61(6):1283-1287. doi:10.1016/j.matlet.2006.07.009

89. Fassler A, Majidi C. 3D structures of liquid-phase GaIn alloy embedded in PDMS with freeze casting. *Lab Chip*. 2013;13(22):4442. doi:10.1039/c3lc50833a

90. Sengupta S, Patra A, Akhtar M, Das K, Majumder SB, Das S. 3D microporous Sn-Sb-Ni alloy impregnated Ni foam as high-performance negative electrode for lithium-ion batteries. *J Alloys Compd*. 2017;705:290-300. doi:10.1016/j.jallcom.2017.02.125

91. Deville S. Ice-templating, freeze casting: Beyond materials processing. *J Mater Res*. 2013;28(17):2202-2219. doi:10.1557/jmr.2013.105

92. Bronstein VL, Itkin YA, Ishkov GS. Rejection and capture of cells by ice crystals on freezing aqueous solutions. *J Cryst Growth*. 1981;52(PART 1):345-349. doi:10.1016/0022-0248(81)90216-5

93. Shao Y, El-Kady MF, Lin CW, et al. 3D Freeze-Casting of Cellular Graphene Films for Ultrahigh-Power-Density Supercapacitors. *Adv Mater*. 2016:6719-6726. doi:10.1002/adma.201506157

94. Ghadkolai MA, Creager S, Nanda J, Bordia RK. Freeze Tape Cast Thick Mo Doped Li $_4$ Ti $_5$ O $_{12}$ Electrodes for Lithium-Ion Batteries. *J Electrochem Soc*. 2017;164(12):A2603-A2610. doi:10.1149/2.1311712jes

95. Porter MM, McKittrick J, Meyers MA. Biomimetic materials by freeze casting. *Jom*. 2013;65(6):720-727. doi:10.1007/s11837-013-0606-3

96. Araki K, Halloran JW. Porous ceramic bodies with interconnected pore channels by a novel freeze casting technique. *J Am Ceram Soc*. 2005;88(5):1108-1114. doi:10.1111/j.1551-2916.2005.00176.x

97. Durán P, Lachén J, Plou J, Sepúlveda R, Herguido J, Peña JA. Behaviour of freeze-casting iron oxide for purifying hydrogen streams by steam-iron process. *Int J Hydrogen Energy*. 2016;41(43):19518-19524. doi:10.1016/j.ijhydene.2016.06.062

98. Hong C, Du J, Liang J, Zhang X, Han J. Functionally graded porous ceramics with dense surface layer produced by freeze-casting. *Ceram Int*. 2011;37(8):3717-3722. doi:10.1016/j.ceramint.2011.04.119

99. Araki K, Halloran JW. New Freeze-Casting Technique for Ceramics with Sublimable Vehicles. *J Am Ceram Soc*. 2005;87(10):1859-1863. doi:10.1111/j.1151-2916.2004.tb06331.x

100. Araki K, Halloran JW. Room-Temperature Freeze Casting for Ceramics with Nonaqueous Sublimable Vehicles in the Naphthalene – Camphor Eutectic System. 2014;2019(10706):2014-2019.

101. Chen R, Wang C, Huang Y, Lin W. Ceramics with special porous structures fabricated by freeze-Gelcasting : Using tert-Butyl Alcohol as a Template. *J Am Ceram Soc*. 2007;3484(22864):3478-3484. doi:10.1111/j.1551-2916.2007.01957.x

102. Li WL, Lu K, Walz JY. Freeze casting of porous materials: review of critical factors in microstructure evolution. *Int Mater Rev*. 2012;57(1):37-60. doi:10.1179/1743280411Y.0000000011

103. Sobolev SL. Rapid colloidal solidifications under local nonequilibrium diffusion conditions. *Phys Lett Sect A Gen At Solid State Phys*. 2012;376(47-48):3563-3566. doi:10.1016/j.physleta.2012.10.031

104. Bareggi A, Maire E, Lasalle A, Deville S. Dynamics of the freezing front during the solidification of a colloidal alumina aqueous suspension: In situ x-ray radiography, tomography, and modeling. *J Am Ceram Soc*. 2011;94(10):3570-3578. doi:10.1111/j.1551-2916.2011.04572.x

105. Rempel AW, Worster MG. Interaction between a particle and an advancing solidification front. *J Cryst Growth*. 1999;205(3):427-440. doi:10.1016/S0022-0248(99)00290-0

106. Zhang H, Cooper AI. Aligned porous structures by directional freezing. *Adv Mater*. 2007;19(11):1529-1533. doi:10.1002/adma.200700154

107. Zhang H, Hussain I, Brust M, Butler MF, Rannard SP, Cooper AI. Aligned two- and three-dimensional structures by directional freezing of polymers and nanoparticles. *Nat Mater*. 2005;4(October):787-793. doi:10.1038/nmat1487

108. Delattre B, Bai H, Ritchie RO, De Coninck J, Tomsia AP. Unidirectional freezing of ceramic suspensions: In situ x-ray investigation of the effects of additives. *ACS Appl Mater*

Interfaces. 2014;6(1):159-166. doi:10.1021/am403793x

109. Muldrew K, Novak K, Yang H, Zernicke R, Schachar NS, McGann LE. Cryobiology of articular cartilage: ice morphology and recovery of chondrocytes. *Cryobiology*. 2000;40(2):102-109. doi:10.1006/cryo.2000.2236

110. Mutou Y, Watanabe K, Ishizaki T, Mizoguchi M. Microscopic Observation of Ice Lensing and Frost Heaves in Glass Beads. *Proc 7th Int Conf Permafr*. 1998.

111. Peppin SSL, Elliott J a. W, Worster MG. Solidification of colloidal suspensions. *J Fluid Mech*. 2006;554(1):147. doi:10.1017/S0022112006009268

112. W. K, Fisher DJ. *Fundamentals of Solidification*. Trans Tech Publications; 1986.

113. Huppert HE. The fluid mechanics of solidification. *J Fluid Mech*. 1990;212:209. doi:10.1017/S0022112090001938

114. Wettlaufer JS, Worster MG. Premelting Dynamics. *Annu Rev Fluid Mech*. 2006;38(1):427-452. doi:10.1146/annurev.fluid.37.061903.175758

115. You J, Wang L, Wang Z, et al. Interfacial undercooling in solidification of colloidal suspensions: analyses with quantitative measurements. *Sci Rep*. 2016;6(June):28434. doi:10.1038/srep28434

116. You J, Wang L, Wang Z, et al. In situ observation the interface undercooling of freezing colloidal suspensions with differential visualization method In situ observation the interface undercooling of freezing colloidal suspensions with differential visualization method. 2015;084901. doi:10.1063/1.4928108

117. Delattre B, Bai H, Ritchie RO, Coninck J De, Tomsia AP. Unidirectional Freezing of Ceramic Suspensions : In Situ X - ray Investigation of the E ff ects of Additives. 2013.

118. Peppin SSL, Worster MG, Wettlaufer JS. Morphological instability in freezing colloidal suspensions. *Proc R Soc A Math Phys Eng Sci*. 2006;463(2079):723-733. doi:10.1098/rspa.2006.1790

119. Wang L, You J, Wang Z, Wang J, Lin X. Interface instability modes in freezing colloidal suspensions: revealed from onset of planar instability. *Sci Rep*. 2016;6(November 2015):23358. doi:10.1038/srep23358

120. Peppin SSL, Wettlaufer JS, Worster MG. Experimental verification of morphological instability in freezing aqueous colloidal suspensions. *Phys Rev Lett*. 2008;100(23):1-4. doi:10.1103/PhysRevLett.100.238301

121. Deville S, Maire E, Bernard-Granger G, et al. Metastable and unstable cellular solidification of colloidal suspensions. *Nat Mater*. 2009;8(12):966-972. doi:10.1038/nmat2571

122. Mullins WW, Sekerka RF. Stability of a planar interface during solidification of a dilute binary alloy. *J Appl Phys*. 1964;35(2):444-451. doi:10.1063/1.1713333

123. Israelachvili JN. *Intermolecular and Surface Forces*. third. Academic press; 2015.

124. Wettlaufer J, Worster M, Wilen L, Dash J. A Theory of Premelting Dynamics for all Power Law Forces. *Phys Rev Lett*. 1996;76(19):3602-3605. doi:10.1103/PhysRevLett.76.3602

125. Rempel AW, Wettlaufer JS, Worster MG. Premelting dynamics in a continuum model of frost heave. *J Fluid Mech*. 2004;498:227-244. doi:10.1017/S0022112003006761

126. Gilpin RR. A model of the “liquid-like” layer between ice and a substrate with applications to wire regelation and particle migration. *J Colloid Interface Sci*. 1979;68(2):235-251. doi:10.1016/0021-9797(79)90277-7

127. Vignes M, Dijkema KM. A model for the freezing of water in a dispersed medium. *J Colloid Interface Sci*. 1974;49(2):165-172. doi:10.1016/0021-9797(74)90348-8

128. Kuroda T, Lacmann R. Growth kinetics of ice from the vapour phase and its growth forms. *J Cryst Growth*. 1982;56(1):189-205. doi:10.1016/0022-0248(82)90028-8

129. Sadtchenko V, Ewing GE, Sadtchenko V, Ewing GE. Interfacial melting of thin ice films : An infrared study Interfacial melting of thin ice films : An infrared study. 2002;4686. doi:10.1063/1.1449947

130. Jellinek HH. Liquid-like (transition) layer on ice. *J Colloid Interface Sci*. 1967;25(2):192-205. doi:10.1016/0021-9797(67)90022-7

131. Itagaki K. Some surface phenomena of ice. *J Colloid Interface Sci*. 1967;227(2):218-227. doi:10.1016/0021-9797(67)90024-0

132. Weyl W. Surface structure of water and some of its physical and chemical manifestations. *J Colloid Sci*. 1951;6(5):389-405. doi:10.1016/0095-8522(51)90011-6

133. Anderson DM. The interface between ice and silicate surfaces. *J Colloid Interface Sci*. 1967;25(2):174-191. doi:10.1016/0021-9797(67)90021-5

134. Taber S. Frost heaving. *J Geol*. 1929;37.

135. Taber S. The Mechanics of Frost heaving. *J Geol*. 1930;38.

136. Dash JG, Rempel AW, Wettlaufer JS. The physics of premelted ice and its geophysical consequences. *Rev Mod Phys*. 2006;78(3):695-741. doi:10.1103/RevModPhys.78.695

137. Dash JG, Fu H, Wettlaufer JS. The premelting of ice and its environmental consequences. *Reports Prog Phys*. 1995;58(1):115-167. doi:10.1088/0034-4885/58/1/003

138. Woodruff DP. *The Solid-Liquid Interface*. Cambridge University Press; 1973.

139. Wettlaufer JS, Worster MG. Dynamics of premelted films: Frost heave in a capillary. *Phys Rev E*. 1995;51(5).

140. Style RW, Peppin SSL, Cocks ACF, Wettlaufer JS. Ice-lens formation and geometrical supercooling in soils and other colloidal materials. *Phys Rev E - Stat Nonlinear, Soft Matter Phys*. 2011;84(4):1-12. doi:10.1103/PhysRevE.84.041402

141. Peppin S, Majumdar A, Style R, Sander G. Frost Heave in Colloidal Soils. *SIAM J Appl Math*. 2011;71(5):1717-1732. doi:10.1137/100788197

142. Peppin SSL, Style RW. The Physics of Frost Heave and Ice-Lens Growth. *Vadose Zo J*. 2013;12(1):0. doi:10.2136/vzj2012.0049

143. Style RW, Peppin SSL. The kinetics of ice-lens growth in porous media. *J Fluid Mech*. 2012;692:482-498. doi:10.1017/jfm.2011.545

144. Anderson AM, Worster MG. Periodic ice banding in freezing colloidal dispersions. *Langmuir*. 2012;28(48):16512-16523. doi:10.1021/la303458m

145. Jackson KA, Chalmers B. Freezing of liquids in porous media with special reference to frost heave in soils. *J Appl Phys*. 1958;29(8):1178-1181. doi:10.1063/1.1723397

146. Everett DH. The thermodynamics of frost damage to porous solids. *Trans Faraday Soc*. 1961;57:1541. doi:10.1039/tf9615701541

147. Jackson KA, Uhlmann DR, Chalmers B. Frost heave in soils. *J Appl Phys*. 1966;37(2):848-852. doi:10.1063/1.1708270

148. Liu Z, Muldrew K, Wan RG, Elliott J a W. Measurement of freezing point depression of water in glass capillaries and the associated ice front shape. *Phys Rev E Stat Nonlin Soft Matter Phys*. 2003;67(6 Pt 1):061602. doi:10.1103/PhysRevE.67.061602

149. Kuhn W, Peterli E, Majer H. Freezing point depression of gels produced by high polymer network. *J Polym Sci*. 1955;16(82):539-548. doi:10.1002/pol.1955.120168238

150. Rempel AW, Worster MG. Particle trapping at an advancing solidification front with interfacial-curvature effects. *J Cryst Growth*. 2001;223(3):420-432. doi:10.1016/S0022-0248(01)00595-4

151. Rahaman MN, Fu Q. Manipulation of porous bioceramic microstructures by freezing of suspensions containing binary mixtures of solvents. *J Am Ceram Soc*. 2008;91(12):4137-4140. doi:10.1111/j.1551-2916.2008.02795.x

152. Tang Y, Qiu S, Wu C, Miao Q, Zhao K. Freeze cast fabrication of porous ceramics using tert-butyl alcohol-water crystals as template. *J Eur Ceram Soc*. 2016;36(6):1513-1518. doi:10.1016/j.jeurceramsoc.2015.12.047

153. Liu X, Xue W, Shi C, Sun J. Fully interconnected porous Al2O3scaffolds prepared by a fast cooling freeze casting method. *Ceram Int*. 2015;41(9):11922-11926. doi:10.1016/j.ceramint.2015.05.160

154. Lasalle A, Guizard C, Leloup J, et al. Ice-templating of alumina suspensions: Effect of supercooling and crystal growth during the initial freezing regime. *J Am Ceram Soc*. 2012;95(2):799-804. doi:10.1111/j.1551-2916.2011.04993.x

155. Zhao K, Tang YF, Qin YS, Wei JQ. Porous hydroxyapatite ceramics by ice templating: Freezing characteristics and mechanical properties. *Ceram Int*. 2011;37(2):635-639. doi:10.1016/j.ceramint.2010.10.003

156. Pawelec KM, Husmann a, Best SM, Cameron RE. A design protocol for tailoring ice-templated scaffold structure. *J R Soc Interface*. 2014;11(92):20130958. doi:10.1098/rsif.2013.0958

157. Xia Z, Yu X, Jiang X, Brody HD, Rowe DW, Wei M. Fabrication and characterization of biomimetic collagen-apatite scaffolds with tunable structures for bone tissue engineering. *Acta Biomater*. 2013;9(7):7308-7319. doi:10.1016/j.actbio.2013.03.038

158. Heschel I, Schoof H. Control of Pore Structure and Size in Freeze-Dried Collagen Sponges. 2001;(8 mm):352-357.

159. Niksiar P, Frank MB, Naleway SE, Meyers MA, McKittrick J, Porter MM. External field assisted freeze casting. *Ceramics*. 2018.

160. Yan JY, Patey GN. Heterogeneous Ice Nucleation Induced by Electric Fields. *J Phys Chem Lett*. 2011;2(20):2555-2559. doi:10.1021/jz201113m

161. Moore EB, Molinero V. Structural transformation in supercooled water controls the crystallization rate of ice. *Nature*. 2011;479(7374):506-508. doi:10.1038/nature10586

162. Petrenko VF, Whitworth RW. *Physics of Ice*. OUP Oxford; 1999.

163. Acharya P V., Bahadur V. Fundamental interfacial mechanisms underlying electrofreezing. *Adv Colloid Interface Sci*. 2018;251:26-43. doi:10.1016/j.cis.2017.12.003

164. Svishchev IM, Kusalik PG. Electrofreezing of liquid water: A microscopic perspective. *J Am Chem Soc*. 1996;118(3):649-654. doi:10.1021/ja951624l

165. Yan JY, Patey GN. Molecular Dynamics Simulations of Ice Nucleation by Electric Fields. *J Phys Chem A*. 2012;116(26):7057-7064. doi:10.1021/jp3039187

166. Ehre D, Lavert E, Lahav M, Lubomirsky I. Water freezes differently on possitively and negatively charged surfaces of pyroelectric materials. *Science (80-)*. 2010;327(February):672-675.

167. Conrad H. Influence of an electric or magnetic field on the liquid–solid transformation in materials and on the microstructure of the solid. *Mater Sci Eng A*. 2000;287(2):205-212. doi:10.1016/S0921-5093(00)00777-2

168. Otero L, Rodríguez AC, Pérez-Mateos M, Sanz PD. Effects of Magnetic Fields on

Freezing: Application to Biological Products. *Compr Rev Food Sci Food Saf*. 2016;15(3):646-667. doi:10.1111/1541-4337.12202

169. Uhlmann DR, Chalmers B, Jackson KA. Interaction between particles and a solid-liquid interface. *J Appl Phys*. 1964;35(10):2986-2993. doi:10.1063/1.1713142

170. Chernov AA, Temkin D., Mel'Nikova A. Theory of the capture of solid inclusions during the growth of crystals from the melt. *Sov Phys Crystallogr*. 1976;21(4).

171. Worster MG, Wettlaufer JS. *The Fluid Mechanics of Premelted Liquid Films*. Cambridge University Press; 1999.

172. Bolling GF, Ciss?? J. A theory for the interaction of particles with a solidifying front. *J Cryst Growth*. 1971;10(1):56-66. doi:10.1016/0022-0248(71)90046-7

173. Gilpin RR. Theoretical studies of particle engulfment. *J Colloid Interface Sci*. 1980;74(1):44-63. doi:10.1016/0021-9797(80)90169-1

174. Chernov AA, Temkin D. Capture of inclusions in crystal growth. *crystall growth Mater*. 1976;2.

175. Dash JG. Thermomolecular pressure in surface melting: motivation for frost heave. *Science*. 1989;246(October):1591-1593. doi:10.1126/science.246.4937.1591

176. Rempel AW, Wettlaufer JS, Worster MG. Interfacial Premelting and the Thermomolecular Force: Thermodynamic Buoyancy. *Phys Rev Lett*. 2001;87(8):088501. doi:10.1103/PhysRevLett.87.088501

177. Legert L, Joannys JF. Liquid spreading. *Rep Prog Phys Rep Prog Phys*. 1992;55:431-431. doi:10.1088/0034-4885/55/4/001

178. De Gennes PG. Wetting: Statics and dynamics. *Rev Mod Phys*. 1985;57(3):827-863. doi:10.1103/RevModPhys.57.827

179. Derjaguin B V. On the repulsive forces between charged colloid particles and on the theory of slow coagulation and stability of lyophobe sols. *Trans Faraday Soc*. 1940;35:203-215.

180. B. V. D, Churaev N V. Definition of disjoining pressure and its importance in equilibrium and flow of thin-films. *Colloid J USSR*. 1976;38(3):402-410.

181. Derjaguin B V. Some results from 50 years' research on surface forces. *Surf Forces Surfactant Syst*. 1987:17-30.

182. Andelman D, Robbins MO, Mchale G, et al. Liquid spreading. *Reports Prog Phys*. 1992;55.

183. PARK MS, GOLOVIN AA, DAVIS SH. The encapsulation of particles and bubbles by an advancing solidification front. *J Fluid Mech*. 2006;560(August 2006):415. doi:10.1017/S0022112006000796

184. Ghosh D, Kang H, Banda M, Kamaha V. Influence of anisotropic grains (platelets) on the microstructure and uniaxial compressive response of ice-templated sintered alumina scaffolds. *Acta Mater*. 2017;125:1-14. doi:10.1016/j.actamat.2016.11.047

185. Waschkies T, Oberacker R, Hoffmann MJ. Investigation of structure formation during freeze-casting from very slow to very fast solidification velocities. *Acta Mater*. 2011;59(13):5135-5145. doi:10.1016/j.actamat.2011.04.046

186. Deville S, Saiz E, Tomsia AP. Ice-templated porous alumina structures. *Acta Mater*. 2007;55(6):1965-1974. doi:10.1016/j.actamat.2006.11.003

187. Scotti KL, Northard EE, Plunk A, Tappan BC, Dunand DC. Directional solidification of aqueous TiO2suspensions under reduced gravity. *Acta Mater*. 2017;124:608-619. doi:10.1016/j.actamat.2016.11.038

188. Miller SM, Xiao X, Faber KT. Freeze-cast alumina pore networks: Effects of freezing conditions and dispersion medium. *J Eur Ceram Soc*. 2015;35(13):3595-3605. doi:10.1016/j.jeurceramsoc.2015.05.012

189. Lichtner AZ, Jauffrès D, Martin CL, Bordia RK. Processing of hierarchical and anisotropic porosity LSM-YSZ composites. *J Am Ceram Soc*. 2013;96(9):2745-2753. doi:10.1111/jace.12478

190. Flauder S, Gbureck U, M??ller FA. Structure and mechanical properties of B-TCP scaffolds prepared by ice-templating with preset ice front velocities. *Acta Biomater*. 2014;10(12):5148-5155. doi:10.1016/j.actbio.2014.08.020

191. Munch E, Saiz E, Tomsia AP, Deville S. Architectural control of freeze-cast ceramics through additives and templating. *J Am Ceram Soc*. 2009;92(7):1534-1539. doi:10.1111/j.1551-2916.2009.03087.x

192. Waschkies T, Oberacker R, Hoffmann MJ. Control of lamellae spacing during freeze casting of ceramics using double-side cooling as a novel processing route. *J Am Ceram Soc*. 2009;92(SUPPL. 1):79-84. doi:10.1111/j.1551-2916.2008.02673.x

193. Brezny R, Green DJ. The effect of cell size on the mechanical behavior of cellular materials. *Acta Metall Mater*. 1990;38(12):2517-2526. doi:10.1016/0956-7151(90)90263-G

194. Ojuva A, Järveläinen M, Bauer M, et al. Mechanical performance and CO2 uptake of ion-exchanged zeolite A structured by freeze-casting. *J Eur Ceram Soc*. 2014;35(9):2607-2618. doi:10.1016/j.jeurceramsoc.2015.03.001

195. Ghosh D, Banda M, Kang H, Dhavale N. Platelets-induced stiffening and strengthening of ice-templated highly porous alumina scaffolds. *Scr Mater*. 2016;125:29-33. doi:10.1016/j.scriptamat.2016.07.030

196. Naglieri V, Bale HA, Gludovatz B, Tomsia AP, Ritchie RO. On the development of ice-templated silicon carbide scaffolds for nature-inspired structural materials. *Acta Mater*. 2013;61(18):6948-6957. doi:10.1016/j.actamat.2013.08.006

197. Huang TH, Huang TH, Lin YS, et al. Phase-Field Modeling of Microstructural Evolution by Freeze-Casting. *Adv Eng Mater*. 2017;1700343:1-13. doi:10.1002/adem.201700343

198. Bai H, Chen Y, Delattre B, Tomsia AP, Ritchie RO. Bioinspired large-scale aligned porous materials assembled with dual temperature gradients. *Sci Adv*. 2015;(December):1-9.

199. Macchetta A, Turner IG, Bowen CR. Fabrication of HA/TCP scaffolds with a graded and porous structure using a camphene-based freeze-casting method. *Acta Biomater*. 2009;5(4):1319-1327. doi:10.1016/j.actbio.2008.11.009

200. Koh YH, Lee EJ, Yoon BH, Song JH, Kim HE, Kim HW. Effect of polystyrene addition on freeze casting of ceramic/camphene slurry for ultra-high porosity ceramics with aligned pore channels. *J Am Ceram Soc*. 2006;89(12):3646-3653. doi:10.1111/j.1551-2916.2006.01311.x

201. Moon JW, Hwang HJ, Awano M, Maeda K. Preparation of NiO-YSZ tubular support with radially aligned pore channels. *Mater Lett*. 2003;57(8):1428-1434. doi:10.1016/S0167-577X(02)01002-9

202. Dong S, Zhu W, Gao X, et al. Preparation of tubular hierarchically porous silicate cement compacts via a tert-butyl alcohol (TBA)-based freeze casting method. *Chem Eng J*. 2016;295:530-541. doi:10.1016/j.cej.2016.03.023

203. Seuba J, Leloup J, Richaud S, Deville S, Guizard C, Stevenson AJ. Fabrication of ice-templated tubes by rotational freezing: Microstructure, strength, and permeability. *J Eur Ceram Soc*. 2017;37(6):2423-2429. doi:10.1016/j.jeurceramsoc.2017.01.014

204. Ouyang A, Gong Q, Liang J. Carbon nanotube-chitosan composite beads with radially aligned channels and nanotube-exposed walls for bilirubin adsorption. *Adv Eng Mater*.

2015;17(4):460-466. doi:10.1002/adem.201400250

205. Bai H, Wang D, Delattre B, et al. Biomimetic gradient scaffold from ice-templating for self-seeding of cells with capillary effect. *Acta Biomater*. 2015;20:113-119. doi:10.1016/j.actbio.2015.04.007

206. Yoon BH, Choi WY, Kim HE, Kim JH, Koh YH. Aligned porous alumina ceramics with high compressive strengths for bone tissue engineering. *Scr Mater*. 2008;58(7):537-540. doi:10.1016/j.scriptamat.2007.11.006

207. Tang Y, Zhao K, Hu L, Wu Z. Two-step freeze casting fabrication of hydroxyapatite porous scaffolds with bionic bone graded structure. *Ceram Int*. 2013;39(8):9703-9707. doi:10.1016/j.ceramint.2013.04.038

208. Macchetta A, Turner IG, Bowen CR. Fabrication of HA/TCP scaffolds with a graded and porous structure using a camphene-based freeze-casting method. *Acta Biomater*. 2009;5(4):1319-1327. doi:10.1016/j.actbio.2008.11.009

209. You J, Wang L, Wang Z, Li J, Wang J, Lin X. Interfacial undercooling in solidification of colloidal suspensions : analyses with quantitative measurements. *Nat Publ Gr*. 2016;(February):1-7. doi:10.1038/srep28434

210. Zuo KH, Zeng YP, Jiang D. Effect of polyvinyl alcohol additive on the pore structure and morphology of the freeze-cast hydroxyapatite ceramics. *Mater Sci Eng C*. 2010;30(2):283-287. doi:10.1016/j.msec.2009.11.003

211. Wu J, Luo B, Liu X, Zhang L. Control of the structure and mechanical property of porous WS2 scaffold during freeze casting. *J Porous Mater*. 2017;25(1):37-43. doi:10.1007/s10934-017-0418-x

212. Zuo KH, Zeng YP, Jiang D. Properties of microstructure-controllable porous yttria-stabilized ziroconia ceramics fabricated by freeze casting. *Int J Appl Ceram Technol*. 2008;5(2):198-203. doi:10.1111/j.1744-7402.2008.02190.x

213. Pot MW, Faraj KA, Adawy A, et al. Versatile wedge-based system for the construction of unidirectional collagen scaffolds by directional freezing: Practical and theoretical considerations. *ACS Appl Mater Interfaces*. 2015;7(16):8495-8505. doi:10.1021/acsami.5b00169

214. Qian L, Ahmed A, Foster A, Rannard SP, Cooper AI, Zhang H. Systematic tuning of pore morphologies and pore volumes in macroporous materials by freezing. *J Mater Chem*. 2009;19(29):5212. doi:10.1039/b903461g

215. Peko C, Groth B, Nettleship I. The effect of polyvinyl alcohol on the microstructure and permeability of freeze-cast alumina. *J Am Ceram Soc*. 2010;93(1):115-120. doi:10.1111/j.1551-2916.2009.03398.x

216. Scotti KL, Dunand DC. Freeze Casting – A Review of Processing, Microstructure and Properties via the Open Data Repository, FreezeCasting.net.

217. Pekor C, Nettleship I. The effect of the molecular weight of polyethylene glycol on the microstructure of freeze-cast alumina. *Ceram Int*. 2014;40(7 PART A):9171-9177. doi:10.1016/j.ceramint.2014.01.134

218. Pekor CM, Kisa P, Nettleship I. Effect of Polyethylene Glycol on the Microstructure of Freeze-Cast Alumina.pdf. 2008;3190(24228). doi:10.1111/j.1551-2916.2008.02616.x

219. Porter MM, Imperio R, Wen M, Meyers MA, McKittrick J. Bioinspired scaffolds with varying pore architectures and mechanical properties. *Adv Funct Mater*. 2014;24(14):1978-1987. doi:10.1002/adfm.201302958

220. Naleway SE, Yu CF, Porter MM, et al. Bioinspired composites from freeze casting with clathrate hydrates. *Mater Des*. 2015;71:62-67. doi:10.1016/j.matdes.2015.01.010

221. Gonda T, Sei T. Formation mechanism of ice crystal habit and side branches of dendritic ice crystals growing from the vapor phase. *J Cryst Growth*. 1990;99:183-187. doi:10.1016/0022-0248(90)90509-J

222. Nguyen PTN, Ulrich J. Production of High-Tensile-Strength Paracetamol Tablets Using the Freeze-Casting Process. *Chem Eng Technol*. 2015;38(6):991-998. doi:10.1002/ceat.201400700

223. Fu Q, Rahaman MN, Dogan F, Bal BS. Freeze-cast hydroxyapatite scaffolds for bone tissue engineering applications. *Biomed Mater*. 2008;3(2). doi:10.1088/1748-6041/3/2/025005

224. Fu Q, Rahaman MN, Dogan F, Bal BS. Freeze casting of porous hydroxyapatite scaffolds. I. Processing and general microstructure. *J Biomed Mater Res - Part B Appl Biomater*. 2008;86(1):125-135. doi:10.1002/jbm.b.30997

225. Deville S, Maire E, Lasalle A, et al. Influence of particle size on ice nucleation and growth during the ice-templating process. *J Am Ceram Soc*. 2010;93(9):2507-2510. doi:10.1111/j.1551-2916.2010.03840.x

226. Lipp G, K??rber C. On the engulfment of spherical particles by a moving ice-liquid interface. *J Cryst Growth*. 1993;130(3-4):475-489. doi:10.1016/0022-0248(93)90536-6

227. KAO JCT, GOLOVIN AA. Particle capture in binary solidification. *J Fluid Mech*. 2009;625(September 2008):299. doi:10.1017/S0022112008005570

228. Tiller W., Jackson K., Rutter J., Chalmers B. The redistribution of solute atoms during the solidification of metals. *Acta Metall*. 1953;1(4):428-437. doi:10.1016/0001-6160(53)90126-6

229. Cisse J, Bolling GF. A study of the trapping and rejection of insoluble particles during the freezing of water. *J Cryst Growth*. 1971;10(1):67-76. doi:10.1016/0022-0248(71)90047-9

230. Sekhar JA, Trivedi R. Solidification microstructure evolution in the presence of inert particles. *Mater Sci Eng A*. 1991;147(1):9-21. doi:10.1016/0921-5093(91)90800-3

231. Hadji L. Morphological instability induced by the interaction of a particle with a solid-liquid interface. *Eur Phys J B*. 2004;37(1):85-89. doi:10.1140/epjb/e2004-00032-2

232. K??rber C, Rau G, Cosman MD, Cravalho EG. Interaction of particles and a moving ice-liquid interface. *J Cryst Growth*. 1985;72(3):649-662. doi:10.1016/0022-0248(85)90217-9

233. Deville S, Saiz E, Tomsia AP. Freeze casting of hydroxyapatite scaffolds for bone tissue engineering. *Biomaterials*. 2006;27(32):5480-5489. doi:10.1016/j.biomaterials.2006.06.028

234. Nagashima K. Nonequilibrium effect of anisotropic interface kinetics on the directional growth of ice crystals. *J Cryst Growth*. 1997;171(3-4):577-585. doi:10.1016/S0022-0248(96)00664-1

235. Young GW, Davis SH, Brattkus K. Anisotropic interface kinetics and tilted cells in unidirectional solidification. *J Cryst Growth*. 1987;83(4):560-571. doi:10.1016/0022-0248(87)90251-X

236. Qian L, Zhang H. Controlled freezing and freeze drying: A versatile route for porous and micro-/nano-structured materials. *J Chem Technol Biotechnol*. 2011;86(2):172-184. doi:10.1002/jctb.2495

237. Wang Z, Wang J, Yang G. Fourier synthesis predicting onset of the initial instability during directional solidification. *Appl Phys Lett*. 2009;94(6):16-19. doi:10.1063/1.3081634

238. Wang L, You J, Wang Z, Wang J, Lin X. Interface instability modes in freezing colloidal suspensions: revealed from onset of planar instability. *Sci Rep*. 2016;6(November 2015):23358. doi:10.1038/srep23358

239. Kurz W, Fisher DJ. *Fundamentals of Solidification*. Trans Tech Publications LTD; 1986.

240. Hunt JD, Lu SZ. Numerical modelling of cellular and dendritic array growth: spacing and structure predictions. *Mater Sci Eng A*. 1993;173(1-2):79-83. doi:10.1016/0921-5093(93)90191-G

241. Klotz M, Amirouche I, Guizard C, Viazzi C, Deville S. Ice templating-an alternative technology to produce micromonoliths. *Adv Eng Mater*. 2012;14(12):1123-1127. doi:10.1002/adem.201100347

242. Chen PY, Lin AYM, Lin YS, et al. Structure and mechanical properties of selected biological materials. *J Mech Behav Biomed Mater*. 2008;1(3):208-226. doi:10.1016/j.jmbbm.2008.02.003

243. Seuba J, Deville S, Guizard C, Stevenson AJ. The effect of wall thickness distribution on mechanical reliability and strength in unidirectional porous ceramics. *Sci Technol Adv Mater*. 2016;17(1):128-135. doi:10.1080/14686996.2016.1140309

244. Porter MM, Niksiar P, Mckittrick J. Microstructural Control of Colloidal-Based Ceramics by Directional Solidification Under Weak Magnetic Fields. *J Am Ceram Soc*. 2016;1926(37101). doi:10.1111/jace.14183

245. Stefan J. Über einige probleme der theorie der wärmeleitung. *Sitzungber, Wien, Akad Mat Natur*. 1889.

246. Stolze C, Janoschka T, Schubert US, M??ller FA, Flauder S. Directional Solidification with Constant Ice Front Velocity in the Ice-Templating Process. *Adv Eng Mater*. 2016;18(1):111-120. doi:10.1002/adem.201500235

247. Hafezi M, Nezafati N, Nadernezhad A, Yasaei M, Zamanian A, Mobini S. Effect of sintering temperature and cooling rate on the morphology, mechanical behavior and apatite-forming ability of a novel nanostructured magnesium calcium silicate scaffold prepared by a freeze casting method. *J Mater Sci*. 2014;49(3):1297-1305. doi:10.1007/s10853-013-7813-8

248. Fukasawa T, Deng Z, Ando M, Ohji T, Kanzaki S. Synthesis of Porous Silicon Nitride with Unidirectionally Aligned. *J Am Ceram Soc*. 2002;85(9):2151-2155. doi:10.1111/j.1151-2916.2002.tb00426.x

249. Porter MM, Yeh M, Strawson J, et al. Magnetic freeze casting inspired by nature. *Mater Sci Eng A*. 2012;556:741-750. doi:10.1016/j.msea.2012.07.058

250. Trivedi R, Kurz W. Solidification microstructures: A conceptual approach. *Acta Metall Mater*. 1994;42(1):15-23. doi:10.1016/0956-7151(94)90044-2

251. Bouville F, Portuguez E, Chang Y, et al. Templated Grain Growth in Macroporous Materials. *J Am Ceram Soc*. 2014;1742:1736-1742. doi:10.1111/jace.12976

252. Bai H, Walsh F, Gludovatz B, et al. Bioinspired Hydroxyapatite/Poly(methyl methacrylate) Composite with a Nacre-Mimetic Architecture by a Bidirectional Freezing Method. *Adv Mater*. 2016;28(1):50-56. doi:10.1002/adma.201504313

253. Bouville F, Maire E, Meille S, Van de Moortèle B, Stevenson AJ, Deville S. Strong, tough and stiff bioinspired ceramics from brittle constituents. *Nat Mater*. 2014;13(5):508-514. doi:10.1038/nmat3915

254. Porter MM, Meraz L, Calderon A, et al. Torsional properties of helix-reinforced composites fabricated by magnetic freeze casting. *Compos Struct*. 2015;119:174-184. doi:10.1016/j.compstruct.2014.08.033

255. Frank MB, Naleway SE, Haroush T, et al. Stiff , porous scaffolds from magnetized alumina particles aligned by magnetic freeze casting. *Mater Sci Eng C*. 2017;77:484-492. doi:10.1016/j.msec.2017.03.246

256. Frank MB, Hei Siu S, Karandikar K, et al. Synergistic structures from magnetic freeze casting with surface magnetized alumina particles and platelets. *J Mech Behav Biomed Mater*. 2017;76(May):153-163. doi:10.1016/j.jmbbm.2017.06.002

257. Martin JJ, Fiore BE, Erb RM. Designing bioinspired composite reinforcement architectures via 3D magnetic printing. *Nat Commun*. 2015;6:8641. doi:10.1038/ncomms9641

258. Kokkinis D, Schaffner M, Studart AR. Multimaterial magnetically assisted 3D printing of composite materials. *Nat Commun*. 2015;6:8643. doi:10.1038/ncomms9643

259. Cao Z, Sassa K, Asai S. The orientation mechanism of (Ca,Sr)Bi4Ti4O15 ceramics prepared by slip casting in high magnetic field and subsequent sintering. *J Eur Ceram Soc*. 2007;27(7):2591-2596. doi:10.1016/j.jeurceramsoc.2006.10.014

260. Akiyama J, Hashimoto M, Takadama H, et al. Formation of c-axis aligned polycrystal hydroxyapatite using a high magnetic field with mechanical sample rotation. *Nippon Kinzoku Gakkaishi/Journal Japan Inst Met*. 2006;70(5):412-414. doi:10.2320/jinstmet.70.412

261. Suzuki TS, Uchikoshi T, Sakka Y. Control of texture in alumina by colloidal processing in a strong magnetic field. *Sci Technol Adv Mater*. 2006;7(4):356-364. doi:10.1016/j.stam.2006.01.014

262. Sakka Y, Suzuki TS, Uchikoshi T. Fabrication and some properties of textured alumina-related compounds by colloidal processing in high-magnetic field and sintering. *J Eur Ceram Soc*. 2008;28(5):935-942. doi:10.1016/j.jeurceramsoc.2007.09.039

263. Griffiths DJ. Introduction To Electrodynamics. 1999.

264. M. M. Porter. Bioinspired Design : Magnetic Freeze Casting. *PhD Diss Univ Calif , SAN DIEGO*. 2014.

265. Sommerfeld A. *Electrodynamics: Lectures on Theoretical Physics*. Academic Press.; 2013.

266. Ebner AD, Ritter JA, Ploehn HJ. Feasibility and limitations of nanolevel high gradient magnetic separation. *Sep Purif Technol*. 1997;11(3):199-210. doi:10.1016/S1383-5866(97)00021-X

267. Erb RM, Martin JJ, Soheilian R, Pan C, Barber JR. Actuating Soft Matter with Magnetic Torque. *Adv Funct Mater*. 2016;26(22):3859-3880. doi:10.1002/adfm.201504699

268. Liu T, Wang Q, Gao A, Zhang C, Wang C, He J. Fabrication of functionally graded materials by a semi-solid forming process under magnetic field gradients. 2007;57:992-995. doi:10.1016/j.scriptamat.2007.08.011

269. Wang Q, Liu T, Gao A, Zhang C, Wang C, He J. A novel method for in situ formation of bulk layered composites with compositional gradients by magnetic field gradient. 2007;56:1087-1090. doi:10.1016/j.scriptamat.2007.02.026

270. Climent E, Maxey MR, Karniadakis GE. Dynamics of Self-Assembled Chaining in Magnetorheological Fluids. *Langmuir*. 2004;20(2):507-513. doi:10.1021/la035540z

271. Promislow JHE, Gast AP, Fermigier M. Aggregation kinetics of paramagnetic colloidal particles. *J Chem Phys*. 1995;102(13):5492-5498. doi:10.1063/1.469278

272. Fermigier M, P. Gast A. Structure evolution in a paramagnetic latex suspension. *J Magn Magn Mater*. 1993;122(1-3):46-50. doi:10.1016/0304-8853(93)91036-7

273. Erb RM, Libanori R, Routhfuchs N, Studart AR. Composites reinforced in three dimensions by using low magnetic fields. *Science (80-)*. 2012;335.

274. Furlani EP, Sahoo Y, Ng KC, Wortman JC, Monk TE. A model for predicting magnetic particle capture in a microfluidic bioseparator. *Biomed Microdevices*. 2007;9(4):451-463.

doi:10.1007/s10544-007-9050-x

275. Erb RM, Segmehl J, Charilaou M, Löffler JF, Studart AR. Non-linear alignment dynamics in suspensions of platelets under rotating magnetic fields. *Soft Matter*. 2012;8(29):7604-7609. doi:10.1039/c2sm25650a

276. Peng X, Min Y, Ma T, Yan M. Two-dimensional Monte Carlo simulations of a suspension comprised of magnetic and nonmagnetic particles in gradient magnetic fields. *J Magn Magn Mater*. 2009;321(19):3250-3255. doi:10.1016/j.jmmm.2009.05.072

277. Peng X, Min Y, Ma T, Luo W, Yan M. Two-dimensional Monte Carlo simulations of structures of a suspension comprised of magnetic and nonmagnetic particles in uniform magnetic fields. *J Magn Magn Mater*. 2009;321(9):1221-1226. doi:10.1016/j.jmmm.2008.11.011

278. Suh YK, Kang S. Motion of paramagnetic particles in a viscous fluid under a uniform magnetic field: Benchmark solutions. *J Eng Math*. 2011;69(1):25-58. doi:10.1007/s10665-010-9364-1

279. Cotten GB, Eldredge HB. Nanolevel magnetic separation model considering flow limitations. *Sep Sci Technol*. 2002;37(16):3755-3779. doi:10.1081/SS-120014830

280. Liu B, Zhu Y. Computer simulation of structures and distributions of particles in MAGIC fluid. *2009 IEEE Int Conf Mechatronics Autom ICMA 2009*. 2009;302:5094-5098. doi:10.1109/ICMA.2009.5246147

281. Ilg P, Coquelle E, Hess S. Structure and rheology of ferrofluids: Simulation results and kinetic models. *J Phys Condens Matter*. 2006;18(38). doi:10.1088/0953-8984/18/38/S15

282. Trohidou KN, Blackman JA. Aggregation and segregation in a mixture of magnetic and nonmagnetic particles. 1995;51(17).

283. Wang H, Chen QW, Sun LX, et al. Magnetic-field-induced formation of one-dimensional magnetite nanochains. *Langmuir*. 2009;25(12):7135-7139. doi:10.1021/la900234n

284. Satoh A, Chantrell R, Coverdale G. Brownian Dynamics Simulations of Ferromagnetic Colloidal Dispersions in a Simple Shear Flow. *J Colloid Interface Sci*. 1999;209(1):44-59. doi:10.1006/jcis.1998.5826

285. Related G. Cluster structures and cluster-cluster aggregations in a two-dimensional ferromagnetic colloidal system. *J Phys A Math Gen Relat content*. 2000.

286. Weis JJ, Levesque D. Chain formation in low density dipolar hard spheres: A Monte Carlo study. *Phys Rev Lett*. 1993;71(17):2729-2732. doi:10.1103/PhysRevLett.71.2729

287. Jeyadevan B, Nakatani I. Characterization of field-induced needle-like structures in ionic and water-based magnetic fluids. *J Magn Magn Mater*. 1999;201(1-3):62-65. doi:10.1016/S0304-8853(99)00013-X

288. Hayes CF. Observation of association in a ferromagnetic colloid. *J Colloid Interface Sci*. 1975;52(2):239-243. doi:10.1016/0021-9797(75)90194-0

289. Ido Y, Inagaki T, Yamaguchi T. Numerical simulation of microstructure formation of suspended particles in magnetorheological fluids. *J Phys Condens Matter*. 2010;22(32). doi:10.1088/0953-8984/22/32/324103

290. Peng X, Yan M, Shi W. A new approach for the preparation of functionally graded materials via slip casting in a gradient magnetic field. *Scr Mater*. 2007;56(10):907-909. doi:10.1016/j.scriptamat.2006.12.020

291. Cutillas S, Bossis G, Cebers A. Flow-induced transition from cylindrical to layered patterns in magnetorheological suspensions. *Phys Rev E - Stat Physics, Plasmas, Fluids, Relat Interdiscip Top*. 1998;57(1):804-811. doi:10.1103/PhysRevE.57.804

292. Piao M, Lane AM, Johnson DT. Rheological and magnetic properties of a metal particle dispersion exposed to magnetic fields. *J Magn Magn Mater*. 2003;267(3):366-372. doi:10.1016/S0304-8853(03)00405-0

293. Aoshima M, Satoh A. Two-dimensional Monte Carlo simulations of a colloidal dispersion composed of polydisperse ferromagnetic particles in an applied magnetic field. *J Colloid Interface Sci*. 2005;288(2):475-488. doi:10.1016/j.jcis.2005.02.093

294. Satoh A. Three-dimensional Monte Carlo simulations of internal aggregate structures in a colloidal dispersion composed of rod-like particles with magnetic moment normal to the particle axis. *J Colloid Interface Sci*. 2008;318(1):68-81. doi:10.1016/j.jcis.2007.09.098

295. Chin CJ, Lu SC, Yiacoumi S, Tsouris C. Fractal dimension of particle aggregates in magnetic fields. *Sep Sci Technol*. 2004;39(12):2839-2862. doi:10.1081/SS-200028768

296. Aoshima M, Satoh A. Two-dimensional Monte Carlo simulations of a colloidal dispersion composed of rod-like ferromagnetic particles in the absence of an applied magnetic field. *J Colloid Interface Sci*. 2006;293(1):77-87. doi:10.1016/j.jcis.2005.06.035

297. Aoshima M, Satoh A. Two-dimensional Monte Carlo simulations of a polydisperse colloidal dispersion composed of ferromagnetic particles for the case of no external magnetic field. *J Colloid Interface Sci*. 2004;280(1):83-90. doi:10.1016/j.jcis.2004.07.025

298. Ebner AD, Ritter JA, Ploehn HJ, Kochen RL, Navratil JD. NEW MAGNETIC FIELD-ENHANCED PROCESS FOR THE TREATMENT OF AQUEOUS WASTES NEW MAGNETIC FIELD-ENHANCED PROCESS FOR THE TREATMENT OF AQUEOUS WASTES. *Sep Sci Technol*. 1999;34(7):1277-1300. doi:10.1080/01496399908951093

299. Ebner AD, Ritter JA, Ploehn HJ. Magnetic hetero-flocculation of paramagnetic colloidal particles. *J Colloid Interface Sci*. 2000;225(1):39-46. doi:10.1006/jcis.2000.6739

300. Liang Y, Hilal N, Langston P, Starov V. Interaction forces between colloidal particles in liquid: Theory and experiment. *Adv Colloid Interface Sci*. 2007;134-135:151-166. doi:10.1016/j.cis.2007.04.003

301. Ebner AD, Ploehn HJ, Ritter JA. Magnetic field orientation and spatial effects on the retention of paramagnetic nanoparticles with magnetite. *Sep Sci Technol*. 2002;37(16):3727-3753. doi:10.1081/SS-120014823

302. Ebner AD, Ritter JA. Retention of paramagnetic particles by magnetite particle clusters with multifunctional character. *Sep Sci Technol*. 2004;39(12):2785-2808. doi:10.1081/SS-200028807

303. Niksiar P, Frank M, McKittrick J, Porter M. Microstructural evolution of paramagnetic materials by Magnetic Freeze Casting. *J Mater Res Technol Submitt*. 2018.

304. Niksiar P, Frank M, McKittrick J, Porter M. Structural Evolution of Paramagnetic Materials by Magnetic Freeze Casting. *J Mater Res Technol*. 2018.

305. Lide DR. Magnetic susceptibility of the elements and inorganic compounds. *Handb Chem Phys*. 2005:130-135.

306. Fatemi-Ardekani A. Identification and Quantification of Calcium in vivo using Susceptibility Weighted Imaging (SWI). *McMaster Univ*. 2010.

307. Frank MB, Hei Siu S, Karandikar K, et al. Synergistic structures from magnetic freeze casting with surface magnetized alumina particles and platelets. *J Mech Behav Biomed Mater*. 2017;(March):1-11. doi:10.1016/j.jmbbm.2017.06.002

308. Wegst UGK, Bai H, Saiz E, Tomsia AP, Ritchie RO. Bioinspired structural materials. *Nat Mater*. 2014;14(1):23-36. doi:10.1038/nmat4089

309. Aizenberg J, Fratzl P. New materials through bioinspiration and nanoscience. *Adv Funct Mater*. 2013;23(36):4398-4399. doi:10.1002/adfm.201302690

310. Seitz H, Rieder W, Irsen S, Leukers B, Tille C. Three-dimensional printing of porous ceramic scaffolds for bone tissue engineering. *J Biomed Mater Res - Part B Appl Biomater*. 2005;74(2):782-788. doi:10.1002/jbm.b.30291

311. Timoshenko SP, Gere JM. *Theory of Elastic Buckling*. SEcond edi. Dover publications, INC.; 1989.

312. Côté F, Deshpande VS, Fleck NA, Evans AG. The out-of-plane compressive behavior of metallic honeycombs. *Mater Sci Eng A*. 2004;380(1):272-280. doi:10.1016/j.msea.2004.03.051

313. Bushnell D. Plastic Buckling of Various Shells. *J Press Vessel Technol Trans ASME*. 1982;104(2):51-72. doi:10.1115/1.3264190

314. Russell BP, Deshpande VS, Wadley HNG. QUASISTATIC DEFORMATION AND FAILURE MODES OF. *Mech Mater Struct*. 2008;3(September).

315. Hutchinson JW. On the postbuckling behavior of imperfection-sensitive structures in the plastic range. *J Appl Mech*. 1972;39(1):155-162. doi:10.1115/1.3422605

316. Porter MM, Niksiar P. Multidimensional mechanics: Performance mapping of natural biological systems using permutated radar charts. *PLoS One*. 2018;13(9):1-18. doi:10.1371/journal.pone.0204309